POLITECNICO DI MILANO

School of Industrial and Information Engineering

Automation and Control Engineering

STEERING WHEEL FOR DRIVING SIMULATOR, STATE OF ART AND MECHANICAL DESIGN

Master's Thesis

Felippe Francesconi 953567

Supervised by: Hermes Giberti

Academic Years 2021/2022

Abstract

This thesis aims at describing the state of the art of force-feedback steering wheel systems. Context, meaning, different macroscopic categories and the relative descriptions are explained in an introduction chapter

The mathematical model of the steering torque felt by the driver due to the mechanical interaction is elaborated in the following chapter. Then a wide exhibition and a detailed description of commercial and literal solutions are carried out, so that a benchmark can be identified.

Finally, after having sized the actuator to reach better performances than the benchmark product a mechanical design is proposed with more alternatives. Driving tests simulating extreme driving conditions are reported to provide the necessary information (e.g forces and torques) for the mechanical design.

The main goal of this thesis is to be propaedeutic for the complete realization of a functional and improved force-feedback steering wheel.

Table of Contents

Nomenclature

F_S = axial load

α = angle around shaft axis

$p(\alpha)$ = contact pressure

p_{MAX} = contact pressure maximum magnitude

p_F = equivalent constant contact pressure

L = adapter length

r = contact radius

T_t = transmissible torque

$F_{friction}$ = friction force

$\tau_{friction}$ = friction shear stress

$T_{x_{max}}$ = maximum steering torque

T_{peak} = peak torque

$T_x, T_y, T_z = Resulting\ torque\ along\ x, y, z\ axis$

$F_x, F_y, F_z = Resulting\ forces\ along\ x, y, z\ axis$

$F_{x_r}, F_{y_r}, F_{z_r} = Forces\ along\ x, y, z\ axis\ applied\ with\ the\ right\ hand$

$F_{x_l}, F_{y_l}, F_{z_l} = Forces\ along\ x, y, z\ axis\ applied\ with\ the\ right\ hand$

$F_{z_{r\_max}}$ = Maximum value of force along z applied with right hand

$F_{z_{l\_max}}$ = Maximum value of force along z applied with left hand

$F_{x_{max}}$ = Maximum value of force along x

$F_{y_{max}}$ = Maximum value of force along y

$F_{z_{max}}$ = Maximum value of force along z

$d_{wheel} = handwheel\ diamenter$

$\sigma_c = circuferential\ stress$

σ_r = radial stress

$\sigma_{c_{max}}$ = maximum circuferential stress

$\sigma_{r_{max}}$ = maximum radial stress

A, B = generic constants

r = generic redius

α = angle around shaft axis

$p(\alpha)$ = contact pressure

p_{MAX} = contact pressure maximum magnitude

r_{hub_i} = internal hub radius

r_{hub_e} = external hub radius

r_{shaft} = shaft radius

d = contact diameter = shaft diameter = internal hub diameter

F_{radial} = radial load

$F_{radial,max}$ = maximum radial load

τ_{radial} = maximum shear stress value due to F_{radial}

σ_{F_x} = axial stress value due to F_x

σ_{T_z} = axial stress value due to T_z

τ_{T_x} = maximum shear stress value due to T_x

T_s = torque due to Fs

$\sigma_{T_{s\_Nom}}$ = nominal axial stress value due to T_s

$\sigma_{T_{s\_Max}}$ = maximum axial stress value due to T_s

T_k = tightening torque for overcoming the friction of nut/screw head and the underneath surface

T_{ga} = effective tightening torque

F_s = axial load

μ = friction coefficient

$D=$ screw major diameter

$d_2=$ screw average diameter

$\varphi=$ helix angle

$\rho'=$ friction angle

Introduction

A virtual driving simulator is a device that allows users to feel a life-like experience of driving an actual vehicle within virtual reality. It is effectively used for studying the interaction of a driver and vehicle and for developing new vehicle systems, human factor study, and vehicle safety research by enabling the reproduction of the actual driving environments in a safe and tightly controlled environment. Mostly vehicle simulators consist of a sum of a software plus physical mockups as the examples steering wheel, gearshift and pedals. The simulator works as a form of a virtuous circle for testing, where the real parts feed on the software and vice versa: since the software is based on the model of the car, it can translate road results directly to the suspension and steering of the physical components, which promptly loop around and dictate force feedback in the simulator through actuators in the steering wheel.

Driver input for vehicle control in driving simulators may include visual cues, steering "feel", and sounds. Visual cues include objects in the environment, road signs, the vehicle speedometer, rearview mirrors etc. Rockwell [48] estimates that drivers receive over 90% of information input via vision. Steering "feel" includes the forces generated by power steering and vibrations from different road surfaces. Gordon [49] found that after vision, steering "feel" was rated the next highest source of input for drivers. Sounds relevant to vehicle control may include tire screeching and the sirens of emergency vehicles. [50]

Controlling a virtual vehicle is a sensory-motor activity with a specific rendering methodology that depends on the hardware technology and the software in use. To replicate the steering dynamic effects on a driving simulation, it is necessary to accomplish the steering wheel of the driving simulator hardware with an actuator (the obtained overall system is the haptic interface) and establish a model of the steering dynamics, including all known physical parameters (provided for each car).

Structure of the thesis

In this section is described how the contents of the present work are divided in each chapter:

1 Sim- Racing Steering Wheel State of the Art: The sim-racing steering wheel concept is defined, followed by brief history of its development along the years. Also studies and solutions found in literature are introduced in this capture

2 Market Analysis: In this chapter force-feedback steering wheel solutions on the market is analyzed, throughout several products of different marks, to identify inner components (motor, mechanical transmission, sensors, power supply etc.), architecture typologies, structural characteristics, and professional context.

3 Benchmark and Cataloguing: After the market analysis, all products are ordinated and clustered in categories, highlighting the pros and cons. When catalogue is done, we are able to identify the best solution, that is a benchmark.

4 Steering System Model: A mathematical model relating steering torque and vehicle dynamics is described. Then some practical tests are introduced, providing some real steering torque values.

5 Steering Wheel Development: Steering wheel project and mechanical design development. Motor selection, adapter design, carter design, etc.

6 Conclusion, Recommendation and Future Work: In this final chapter the conclusion are illustrated leading to recommendation for future work that could be carry out.

1 Sim- Racing Steering Wheel State of the Art

A racing wheel is a control technique used in racing video games, racing simulators, and driving simulators. In contrast to digital control, such as a keyboard, an analog wheel and pedal combination like this one allows the user to precisely change the steering angle and pedal control needed to effectively drive a simulated automobile. The relatively wide range of motion also enables the user to apply controls more precisely. They are often bundled with a paddle styled as a steering wheel, a set of pedals for gas, brakes, and occasionally clutch actuation and numerous shifting controls. Racing wheels have been developed for use with arcade games, game consoles, personal computers, and for professional driving simulators for race drivers.

When referring to sim racing, force feedback is a feature within certain wheels that try to simulate the feel of a real car by making the wheel react with resistance (steering torque).

Racing wheels started as simple plastic wheels hooked up to a rotary potentiometer, which was sprung by springs or bungees. These spring-based wheels had a reactive torque that increased proportionally only to the steering angle, without regard for the simulated vehicle dynamics.

Eventually, manufacturers began to use electric motors in the controllers, in place of springs, in order to achieve a level of force feedback (sometimes abbreviated FFB), first seen in Microsoft's Sidewinder wheel. At first, this technology simply provided the centering force and other artificial effects such as shaking the wheel in a crash or other vibrations. However, as driving simulations have evolved, their physics engines have become more accurate, allowing also for linking the force feedback close to the simulated vehicle dynamics of the in-game physics. This allows the user to truly feel what forces go through the steering rack, instead of just artificial effects, and genuinely enhances the realism of the game. A fundamental factor for an adequate subjective steering feel and perception of drivability from a force feedback wheel is the transfer function from steering torque to the steering angle. [1]-[2]-[3]

In literature, two representative prototypes were found and are reported below:

1° Model

In uncoupled steering systems such as drive by wire, it is necessary for the driver to feel a simulated reaction torque related to tire/road interactions. To investigate this haptic necessity was constructed a simple stationary force feedback steering wheel.

In this model, the exterior of the steering system is composed of the wheels, the shaft and a DC motor (Figure 21). The steering wheel is connected to a 1/2" drive shaft which rotates in two

roller bearing assemblies at both ends. The shaft is press-fit into the bearings and is secured further by shaft collars which completely limit thrust movement. The shaft is then connected to a DC motor by a belt and pulley system. For the motor, motor controller, optical encoder and encoder circuitry, Phidgets parts are used due to their low cost and ease of connectivity. The motor was mounted in 1/2" Delrin brackets which each have two bolts for adjusting belt tension. All motor circuitry was mounted within the box for aesthetics. To power, the motor, a BK Precision AC/DC power supply was used and mounted atop the main box. This steering system is relatively portable at 25"x16"x17"(LxWxH) and can be affixed to any table. The system has a slight tilt (15 degrees) to mimic an actual steering column. [12]

Figure 1 Exterior Steering System
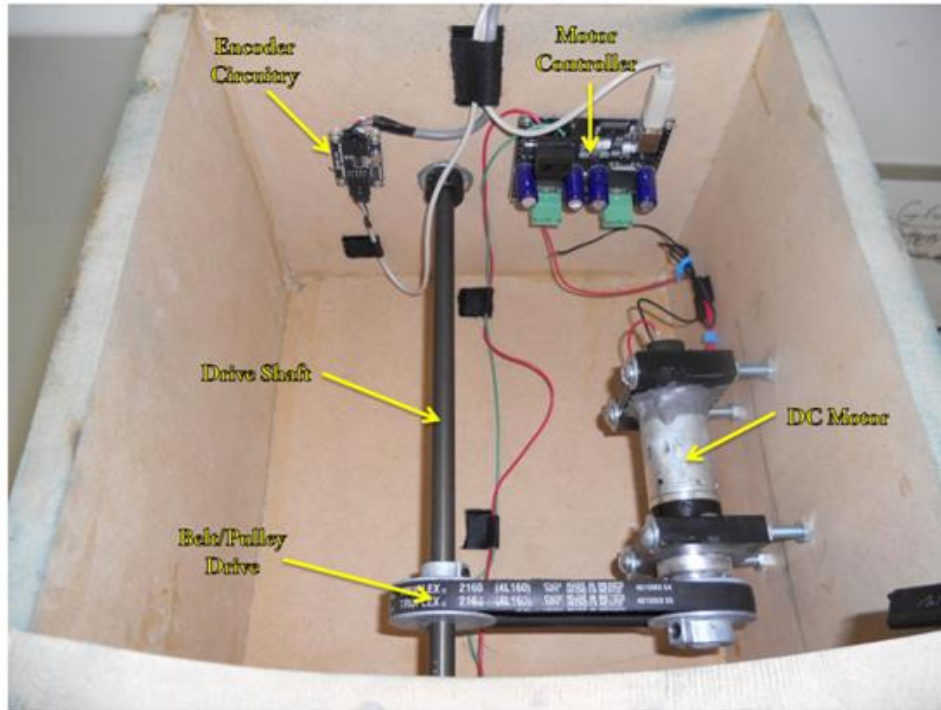
Figure 2 Interior Components

2° Model

This model is represented by interconnected chain-type matrices (Figure 22), which allows good modularity of the implementation, allowing changing or tuning a specific module without rewriting the equations for the entire steering system. A chain matrix representation of each module is motivated by the very fact that the overall transfer function is obtained by a simple ordered product of the connected set of transfer matrices.

Figure 3 Steering System

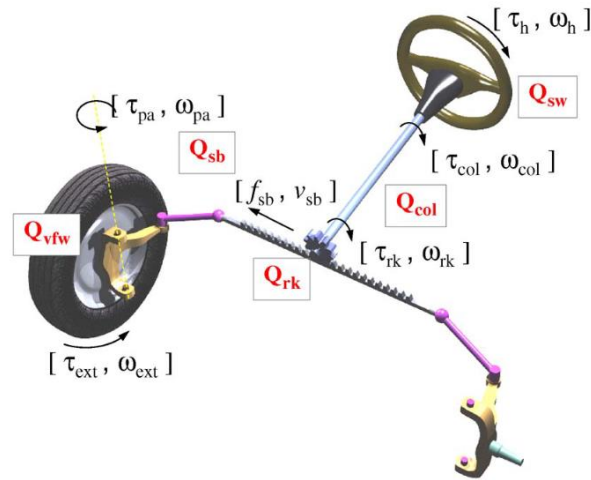The mechanical model of the steering system includes the dynamics induced by the following:

1) inertia and stiffness of the steering column.

2) pinion/rack link.

3) mass of the rack.

4) inertia and dynamic friction of the front wheels.

In this driving simulator, an actual car steering wheel and only a part of the steering column are installed. Using a DC actuator, the motorized steering wheel is linked with the dynamics of the steering system thanks to the simulated stiffness and damping of the steering column (figure 23). These elements will behave as a bilateral coupling in a force-reflecting system. To give the simulator steering wheel similar dynamics to any given actual vehicle steering wheel while altogether computing force feedback during virtual driving, the actuator's desired torque is computed.[13]
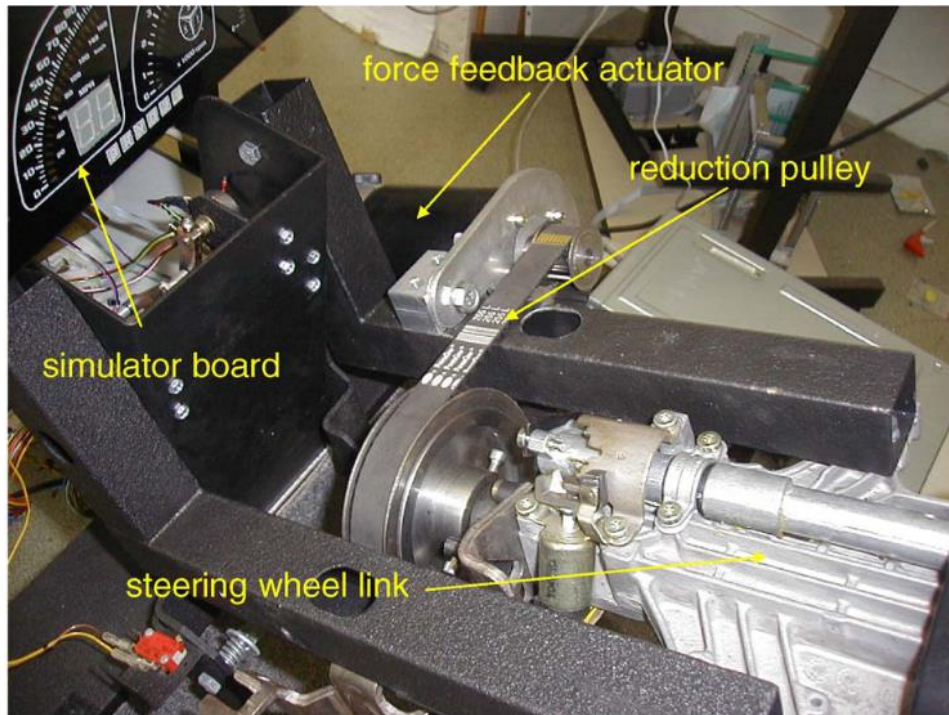
Figure 4 Steering System

Since in literature there is not enough information for developing an improved force-feedback steering wheel, in the next chapter a market analysis was carried out to fetch more information.

2 Market Analysis

In this chapter the force-feedback steering wheel solutions on the market is analyzed, throughout several products of different marks, to identify inner components (motor, mechanical transmission, sensors, power supply etc.), architecture typologies, structural characteristics, and professional context.

The main goal of this capture is to fetch enough information for a benchmark identification that is exposed on the next capture.

2.1 Thrustmaster T300 RS

2.1.1 Outside

Figure 5 Thrustmaster T300 RS Base

Base size: 180mm x 310mm x 234mm

2.1.2 Inside

Figure 6 Thrustmaster T300 RS Inside Components
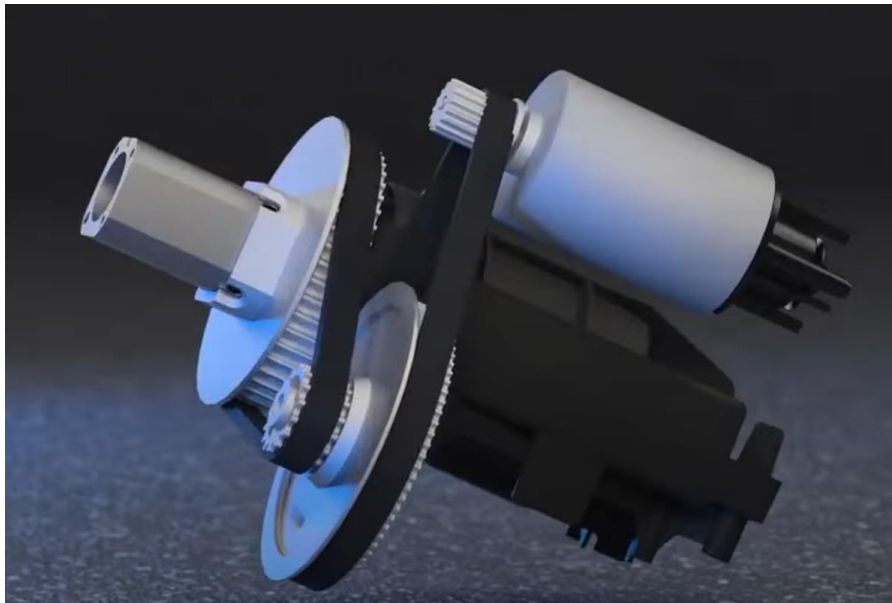
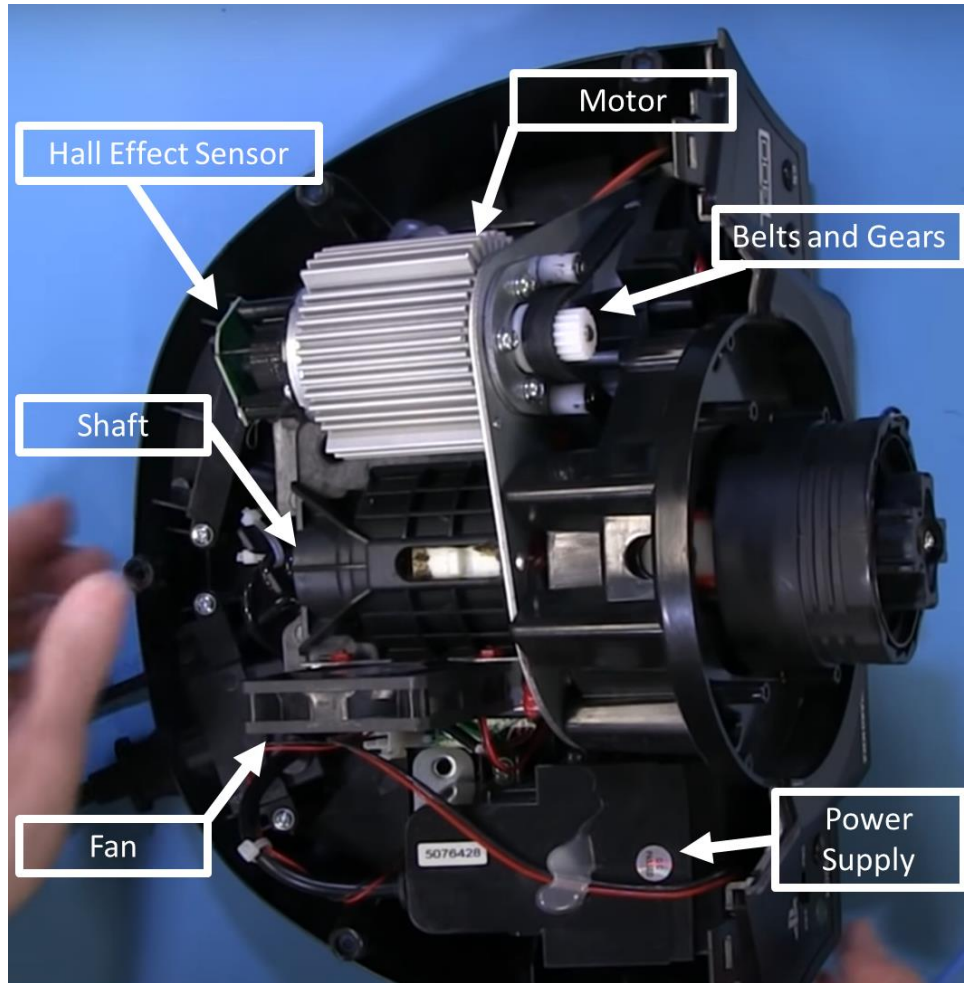## 2.1.3 Main Components

Figure 7 Inside view

2.1.4 Motor

To generate the Feedback Torque on the steering wheel, which makes it possible to simulate driving a real car, is provided by DC Brushless Motor labelled B4260M-S03 and manufactured by HengDrive. [14]-[15]
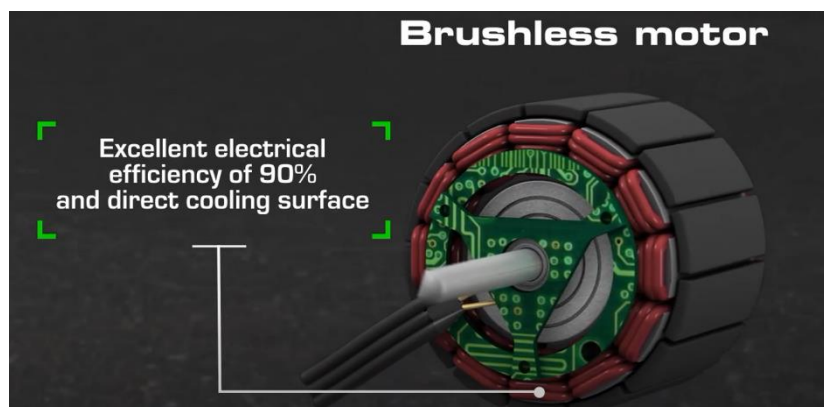
Motor Description and Technical information:

Figure 8 Thrustmaster T300 RS Motor

	KLS23-B4260M	Output Power: 10W~50W		Weight: 290g (Approx.)

Brushless DC Motor-Typical Application

Home Application: White Goods, Small Appliance, Fanner, Coffee Machine, Meat Grinder

Medical Apparatus: Medical Pump, Surgery Tools, Medical Stirrer, centrifugal Machine

Power Tools: Screwdriver, Drill, Air Compressor

Business Equipment: Printer, Copier, Projector, ATM, Vending Machine

Personal Care: Hair Dryer, Massager, Vibrator

Model	Voltage(V)		No Load		Rated Load			Starting	
	Operating Range	Rated	Speed (rpm)	Current (A)	Torque (mNm)	Speed (rpm)	Current (A)	Output P. (W)	Torque (mNm)	Current (A)
B4260M-S01	8-26	12	4590	0.28	45.00	3500	1.88	16.54	190.2	7.04
B4260M-S02	8-26	24	4260	0.26	95.06	3270	1.85	32.58	409.2	7.10
B4260M-S03	8-26	24	7960	0.30	68.00	5920	2.48	42.19	265.4	8.00

Figure 9 Thrustmaster T300 RS Brushless DC Motor Datasheet

Motor Dimensions:
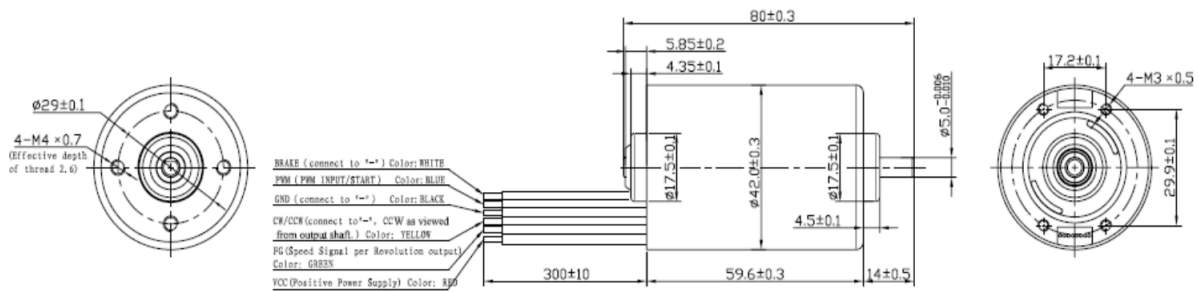
Figure 10 Thrustmaster T300 RS Motor Technical Drawing

Motor Curve [rotational speed-torque]:
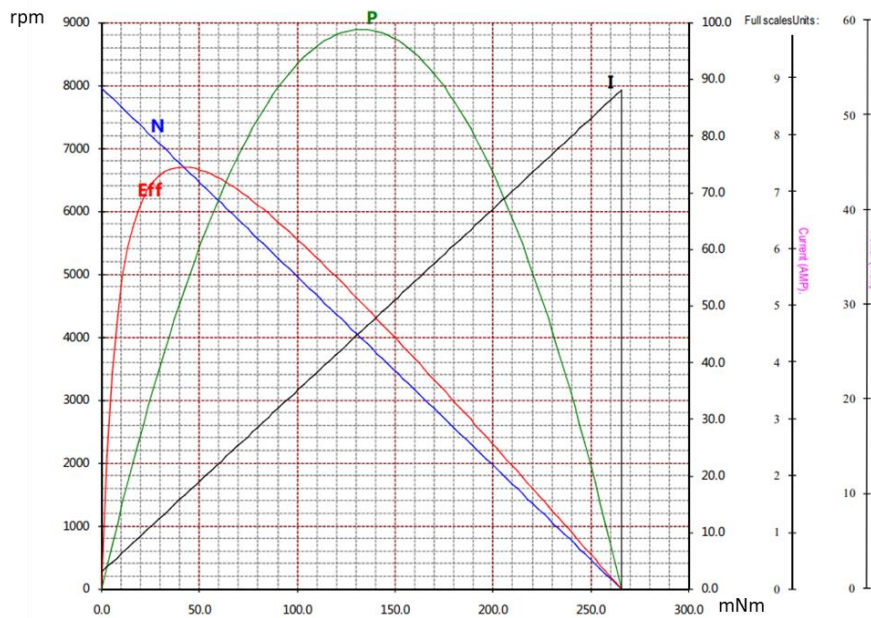
Figure 11 Thrustmaster T300 RS Motor Curve

18

2.1.5 Belts and Gears

In this project, Thrustmaster has chosen belts as a means to transmit power from the motor to the wheel. Two sets of gears and belts were used. The first set leads the power from the motor gear to gear 1.1 and the second set from gear 1.2 (gears 1.1 and 1.2 are two sides of the same gear) to the shaft gear.
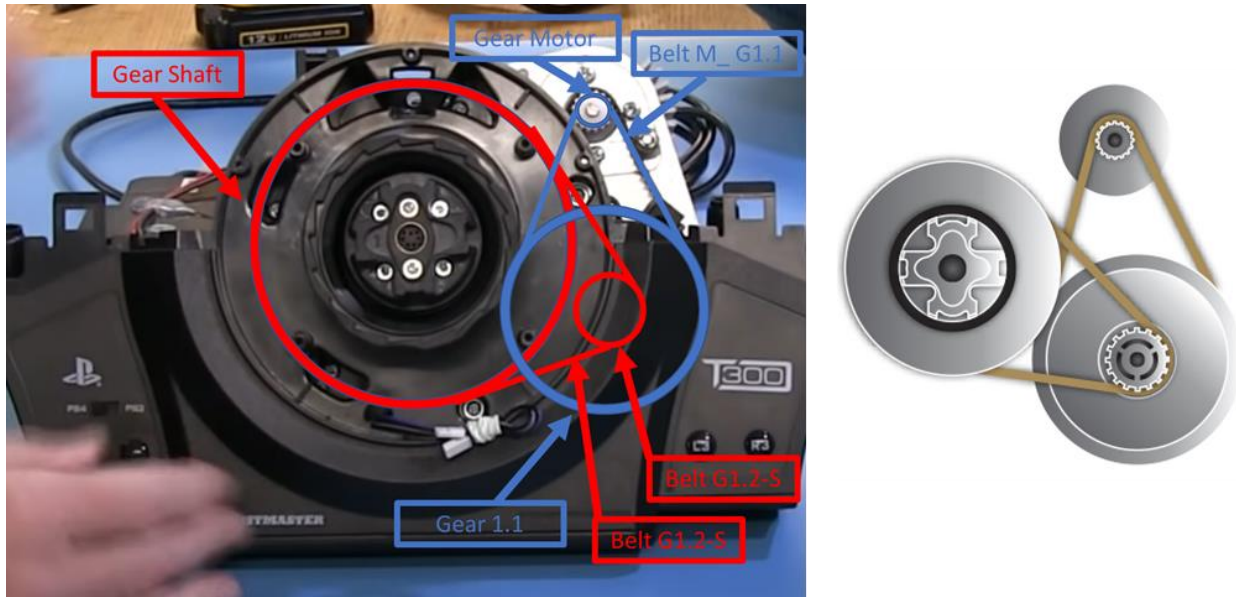
Figure 12 Thrustmaster T300 RS Belts and Gears

Gear Motor

The gear assem]bled to the motor shaft is a PowerGrip® GT3 324 3MGT 9 and has the following features [16]-[18]-[19]:

Pitch: 3mm   Pitch Length:324mm   N°teeth:108   Width:9mm

19
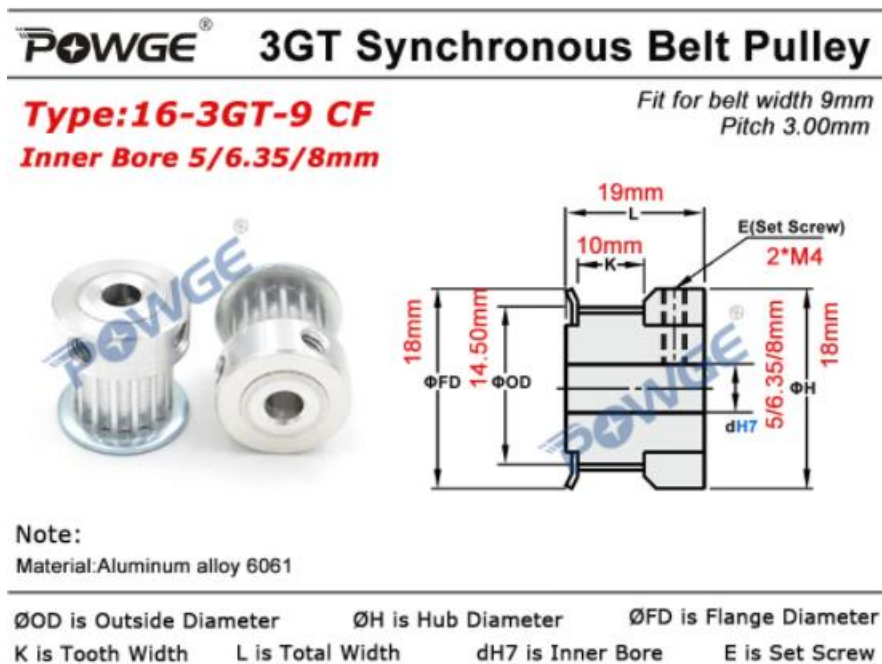
Figure 13 Motor Gear

Belt Gear 1.2 – Gear 2

The belt connecting Gear 1.2 and Gear 2 is a PowerGrip® GT3 325 5MGT 9

and has the following features [17]-[18]-[19]:

Passo: 5mm   Lunghezza passo:325mm   N°denti:108 Width:9mm

2.1.6 Hall Effect

The sensor chosen for measuring the wheel position was a Hall effect sensor, providing a resolution of 65.536 steps per revolution (16 bits).

The sensor is the small chip on the board, which is attached to the motor shaft. The sensor counts the rotation of the motor shaft that can be traduced in terms of wheel rotation through the gear ratios.
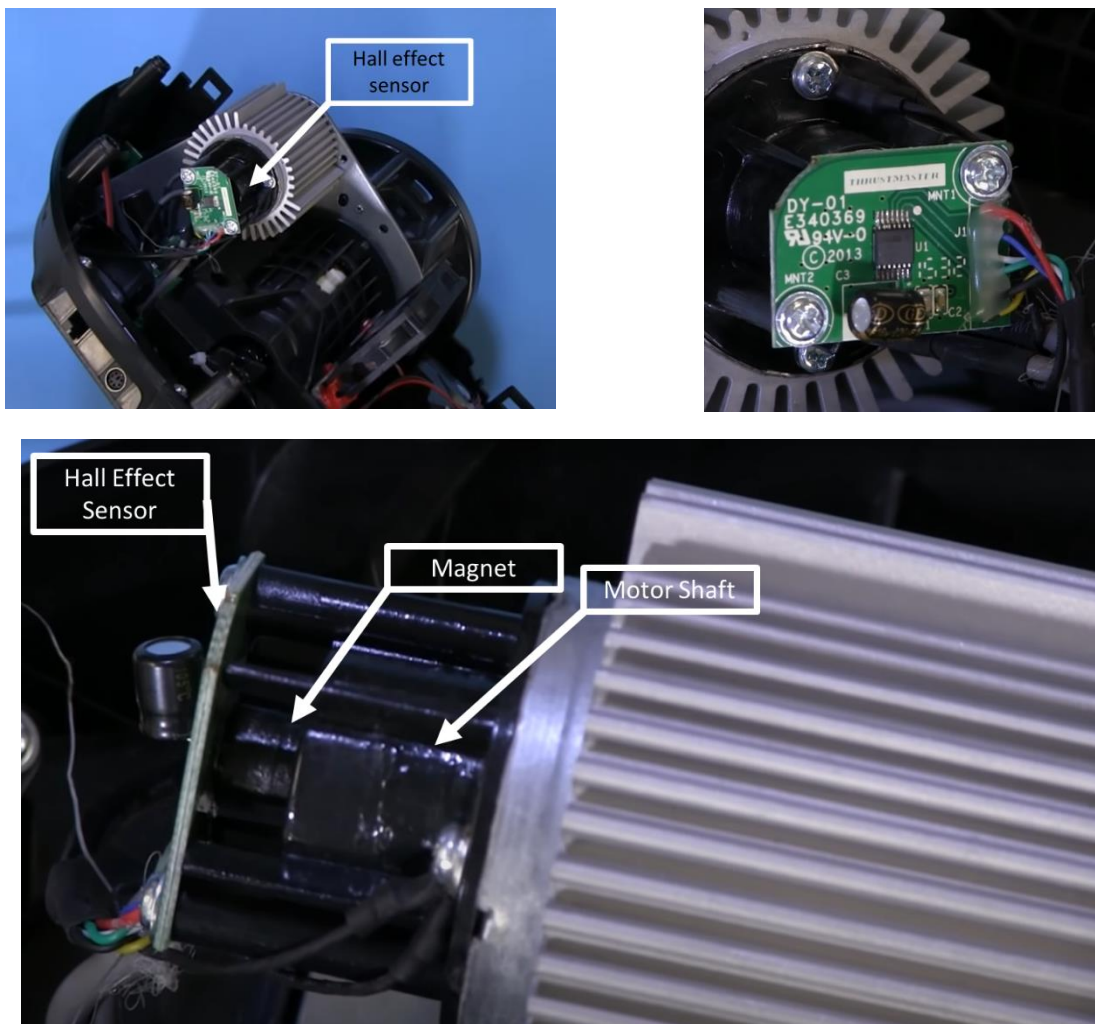
Figure 14 Hall Effect Sensor (Angular Position Sensor)

2.1.7 Power Supply

Input: 240 VAC 1A max   Output: 25 VDC 2A max

All the devices inside the steering wheel required a 24VDC in input. Then for power supplying such devices have applied the device shown below [21]-[22]:

Figure 15 Power Supply

2.1.8 Fan

T300's cooling system is composed of a passive part, represented by the heatsink coupled to the motor, and the active part which is a dc brushless Fan. Follows specification.[21]-[22]
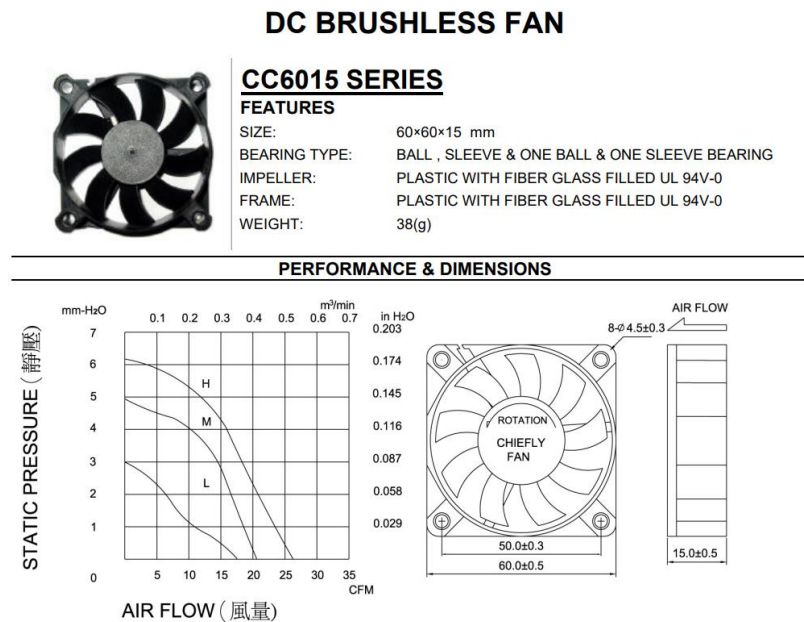
Figure 16 Fan Datasheet

2.2 Logitech G29

2.2.1 Outside

Figure 17 Logitech G29

On the outside, the Logitech G29 steering wheel can be disassembled into two main parts the wheel and the base.

Figure 18 Logitech G29 Base

Figure 19 Logitech G29 Hand Wheel

For the Thesis, we are focusing on the base.

Base size: 180mm x 260mm x 278mm

2.2.2 Inside

Figure 20 Logitech G29 Inside Components

Inside the G29 Wheel, there are several mechanical and electrical parts. Opening the G29 Wheelbase we find the motherboard. On it there is an entire circuitry meant to power supply the devices (**integrated power supply**), acquire data from the Hall Effect sensor, control motors to generate the Feedback Torque, besides the interfaces with the pc/console and other peripheral devices. [23]-[24]-[25]-[28]
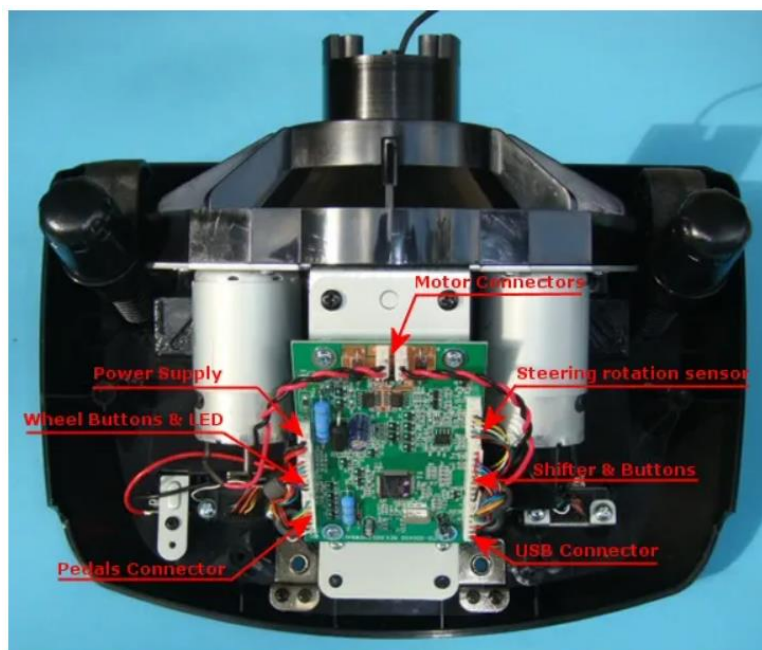
Figure 21 Inside View

2.2.3 Main Components
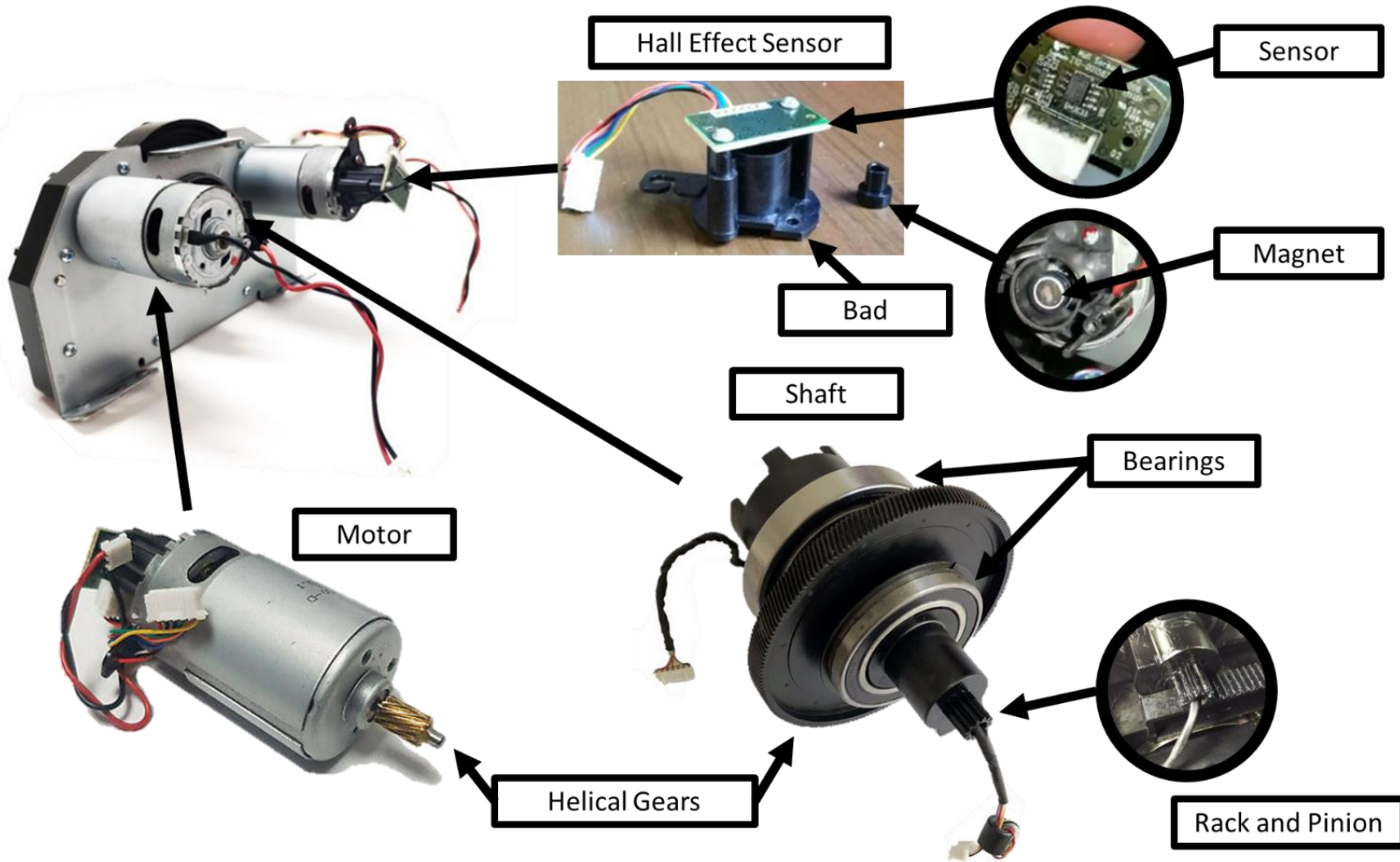
Figure 22 Logitech G29 Main Components

2.2.4 Motor Interface

The 2 mm thick metal plate is used as support for motors and shaft. The second shaft bearing is placed in the central hole.
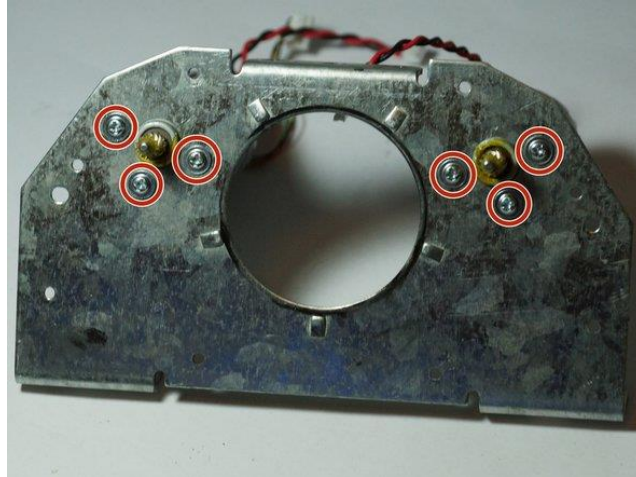
Figure 23 Logitech G29 Motor Interface

2.2.5 Motor

In G29 Steering Wheel, to ensure the correct Feedback Torque during the driving simulation Logitech has chosen a DC Brushed Motor labelled RS555SH-15260 from Leili. [26]-[27]

Motor Description and Technical information:

Model 型号		Voltage 电压		No Load 空载		At Maximum Efficiency 在最大效率时					Stall 堵转		
		Operating Range 工作范围	Nominal 额定	Speed 速度	Current 电流	Speed 速度	Current 电流	Torque 扭矩		Output 输出	Torque 扭矩		Current 电流
		V	V	r/min	A	r/min	A	mN.m	g.cm	W	mN.m	g.cm	A
RS-555SH	15260	12~28	24	1850	0.026	1560	0.15	14.70	150	2.4	84.529	862.54	0.72
RS-555SH	3256	12~28	12	5000	0.26	4309	0.15	1.12	207.7143	9.185	147.3	1503.061	7.00

Figure 24 Logitech G29 Motor Datasheet

Motor Dimensions:
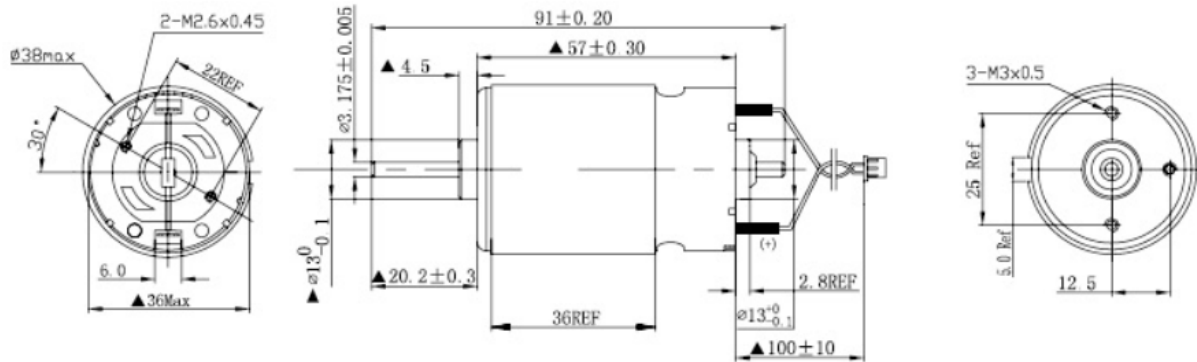
Figure 25 Logitech G29 Motor size

Motor Curve [rotational speed-torque]:
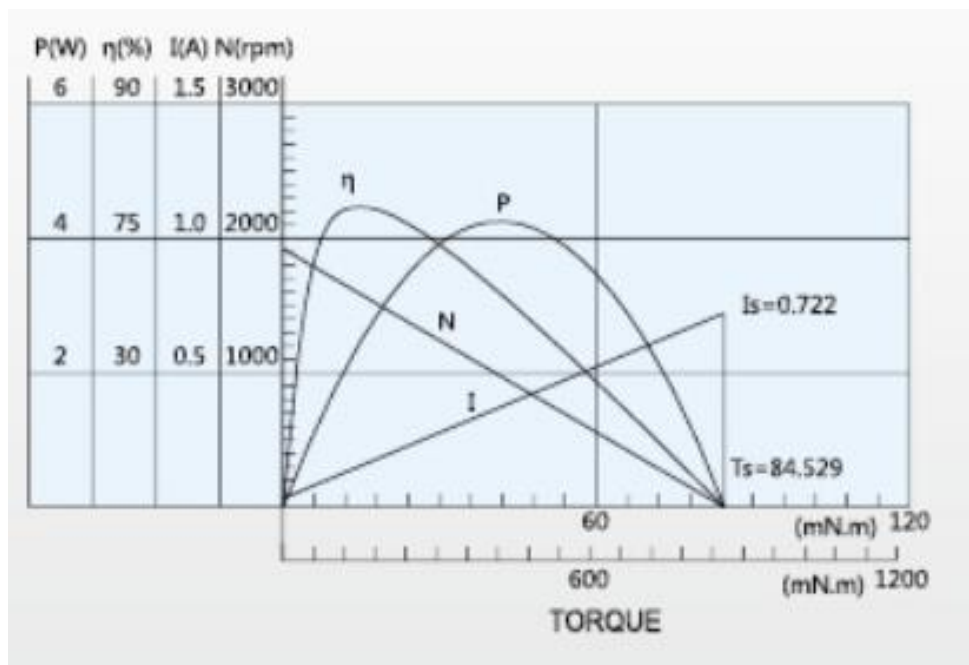
Figure 26 Logitech G29 Motor Curve

2.2.6 Shaft

The shaft connects the wheel to the gears which receive the torque from the motor.
The shaft is bounded by three points two bearings (minus 2 degrees of freedom for each bearing) and a rack-and-pinion at the end (minus 1 degree of freedom). The rack-and-pinion has the further objective to mechanically limit the rotation angle of the wheel. [28]-[29]
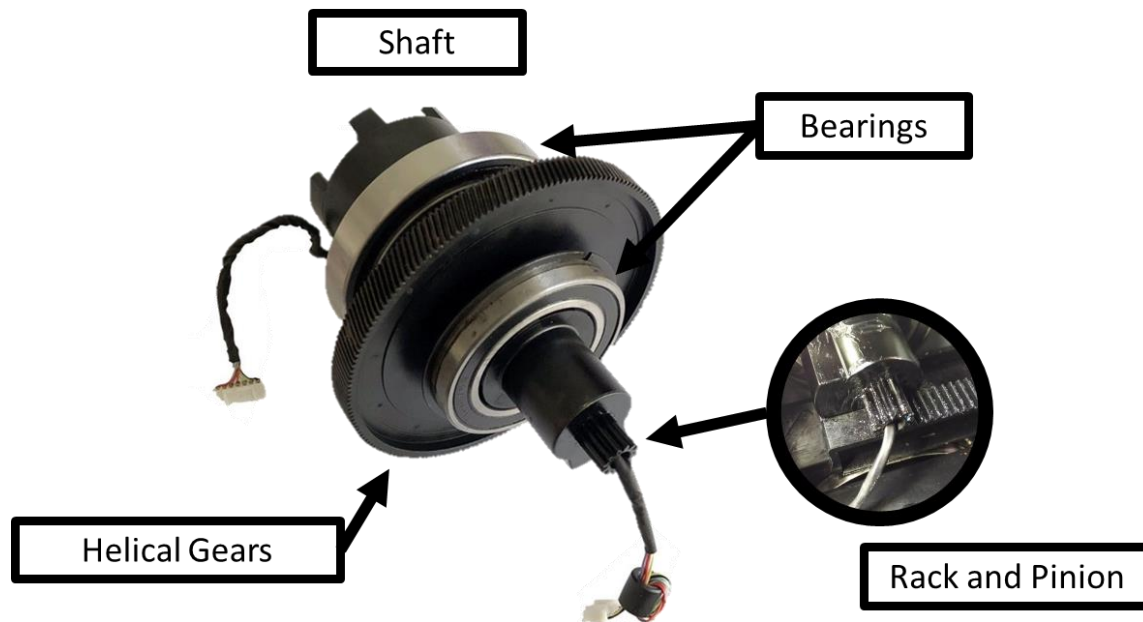
Figure 27 Logitech G29 Shaft Assembly

Under the rack, there is a flat spring meant to push the rack against the pion to avoid backlash between them. See the figure below.
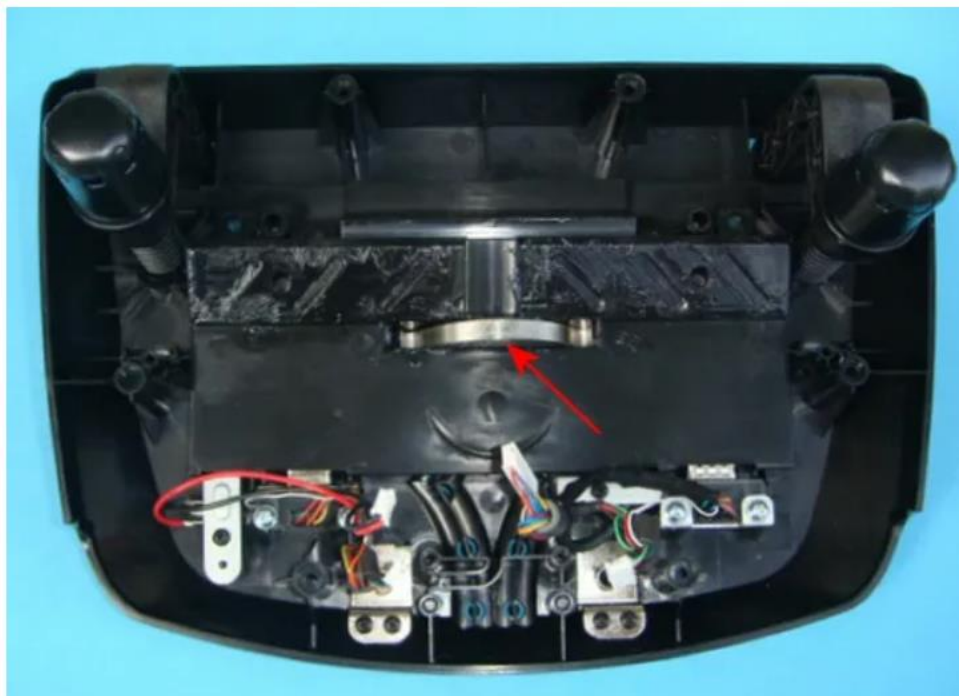
Figure 28 Logitech G29 Rack Spring

2.2.7 Plastic cover

On the Assembly plastic cover, there are two small grooves, where pre-loaded springs and spacers (white plastic part) are mounted and a bigger hole where the shaft bearing is placed. [27]-[28]
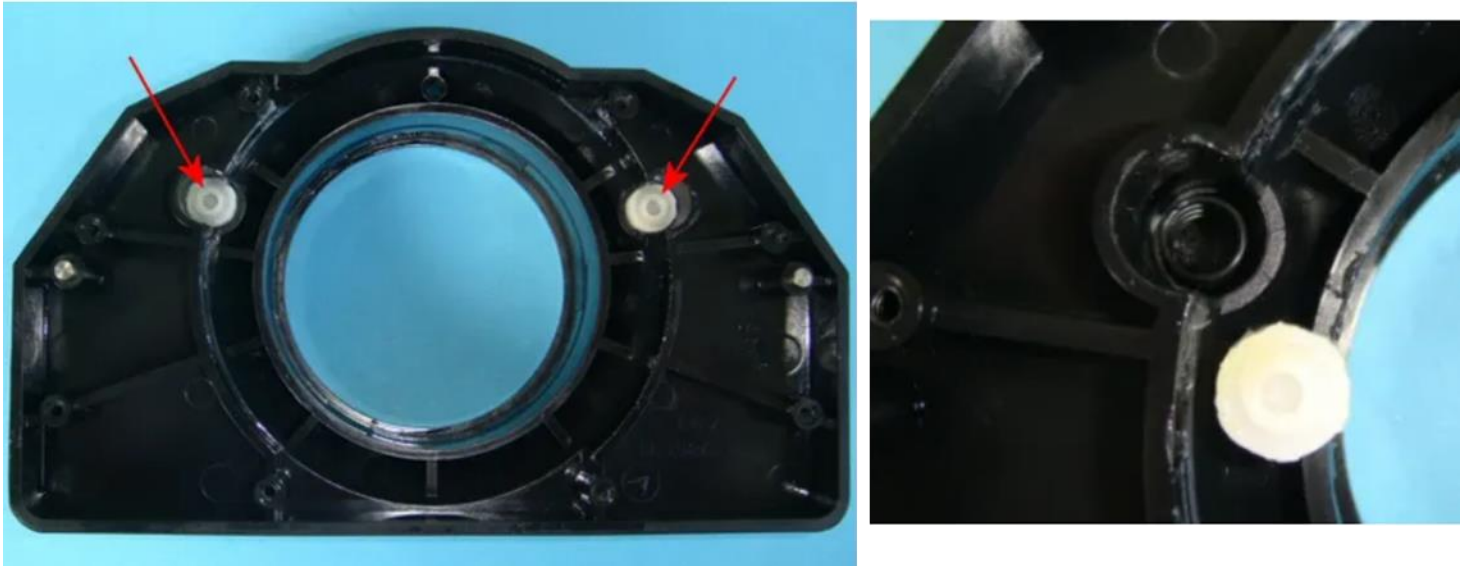
Figure 29 Logitech G29 Plastic Cover

The motors are assembled on one side of the metal plate while a black cover with springs and spacer mounted is assembled on the other side so that gears movements along the motor shaft are not allowed.

Figure 30 Logitech G29 Motor Assembly

28

Movements to be blocked:

Figure 31 Logitech G29 Movements Constraint

2.2.8 Gears

The set of helicoidal gears is composed of 2 small gears (7mm external diameter) assembled to
the motors shaft and a big gear (97mm external diameter) assembled to the shaft. [28]-[29]

Figure 32 Logitech G29 Motor Gears

2.2.9 Hall Effect Sensor

The sensor chosen for measuring the wheel position was a Hall effect sensor, providing a resolution of 256 steps per revolution (8 bits).

To physically create the sensor, we need the sensor itself, that is, the chip attached to the board, a "bad" for holding the board and ar link to couple the magnet to the motor shaft so that we can measure the shaft rotation. [27]-[28]
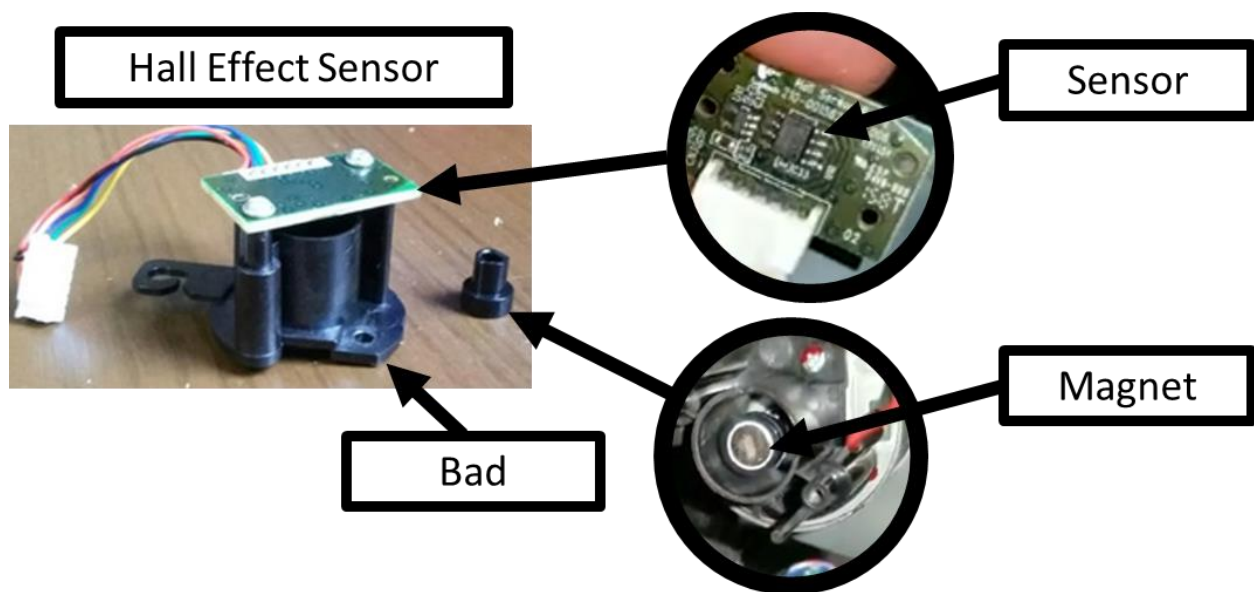
Figure 33 Logitech G29 Hall effect sensor Assembly

2.3 Fanatec Podium DD1/DD2

The Podium DD1 is the first plug-and-play **direct drive** wheelbase, featuring integrated electronics within the main housing.

Figure 34 Fanatec Podium DD1/DD2

2.3.1 Motor

Podium wheel bases use a tailor-made DC brushless outrunner motor engineered from the ground up specifically for sim racing. Instead of using a random industrial motor, the custom motors are tailored on purpose for the specific requirements of the sim racing. [30]-[31]-[32]
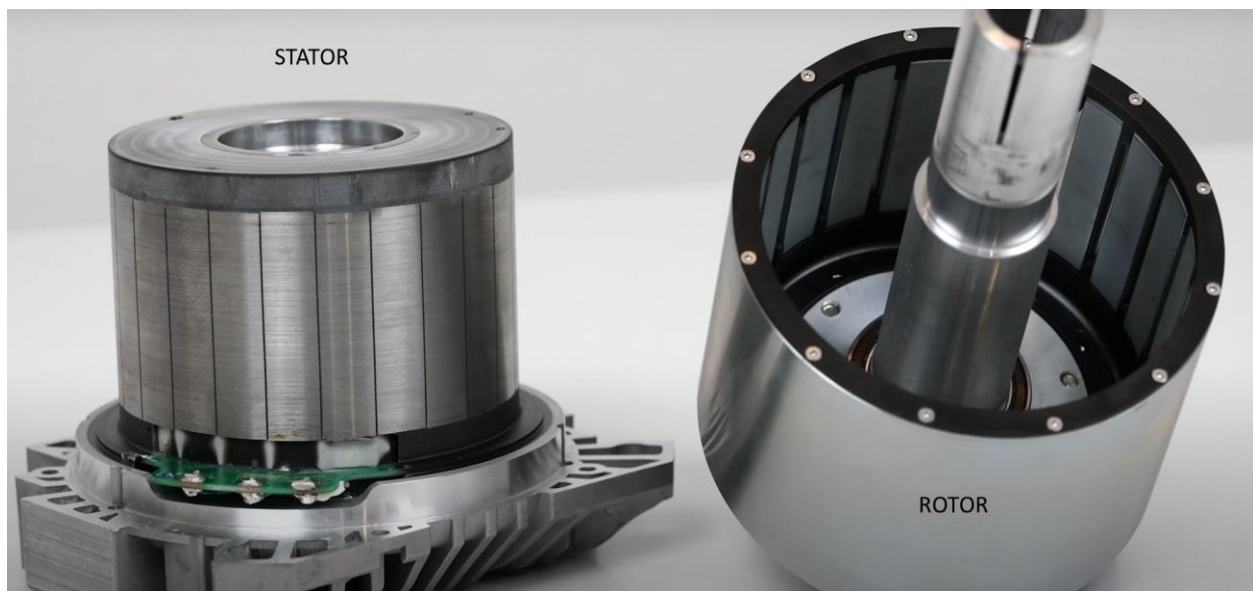
Figure 35 Fanatec Podium DD1/DD2 Motor

Podium DD1 and Podium DD2 are mechanically identical and differ only in power as the Podium DD1 is electronically limited.

Podium DD1's maximum holding torque value is 15Nm and Podium DD2's is 18 Nm.

Figure 36 Fanatec Podium DD1/DD2 Holding Torques

While Podium DD1's peak value of torque is 18 Nm and Podium DD2's is 24 Nm.

Figure 37 Fanatec Podium DD1/DD2 Peak Torques

2.3.2 Wireless Data transfer and Power Supply

The endless rotation of a direct drive motor led to the development of a wireless solution to transfer data and power to the wheel inputs and displays. This means no USB cables are flying around which can easily get damaged and make it difficult to let the wheel spin in a drift.
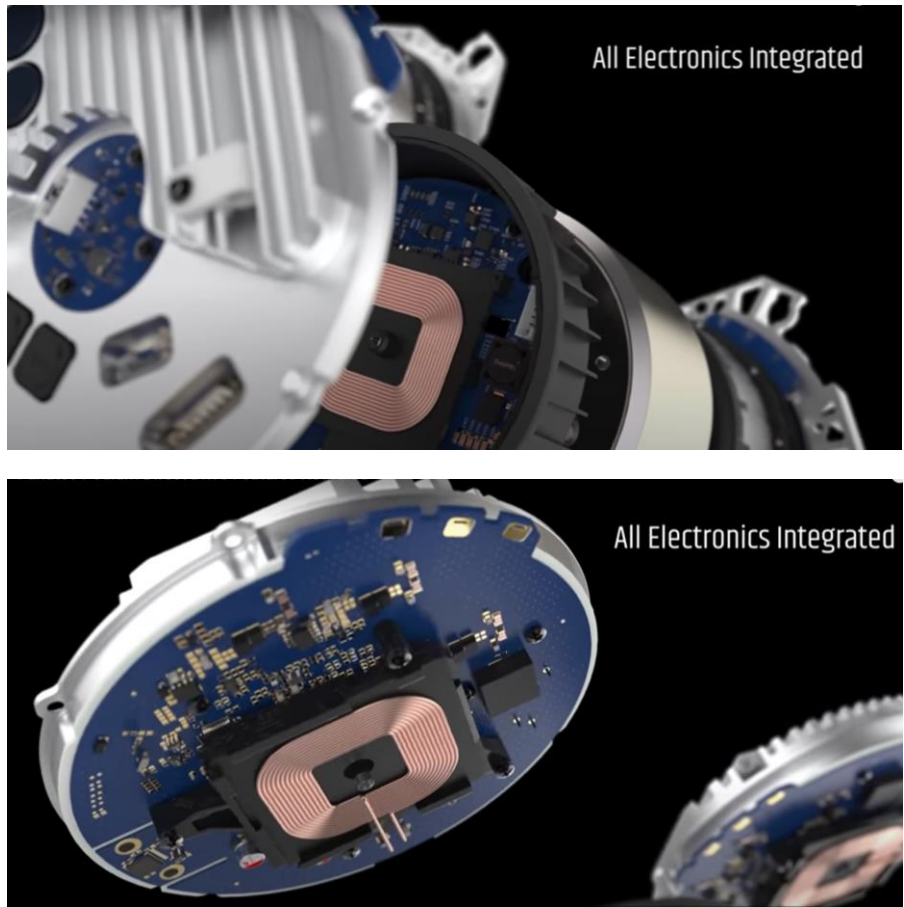
Figure 38 Fanatec Podium DD1/DD2 Data Transfer Links and Power Supply

2.3.3 Podium DD1/DD2 Teardown

Internally the wheelbase can be divided into 2 main assemblies and the cover
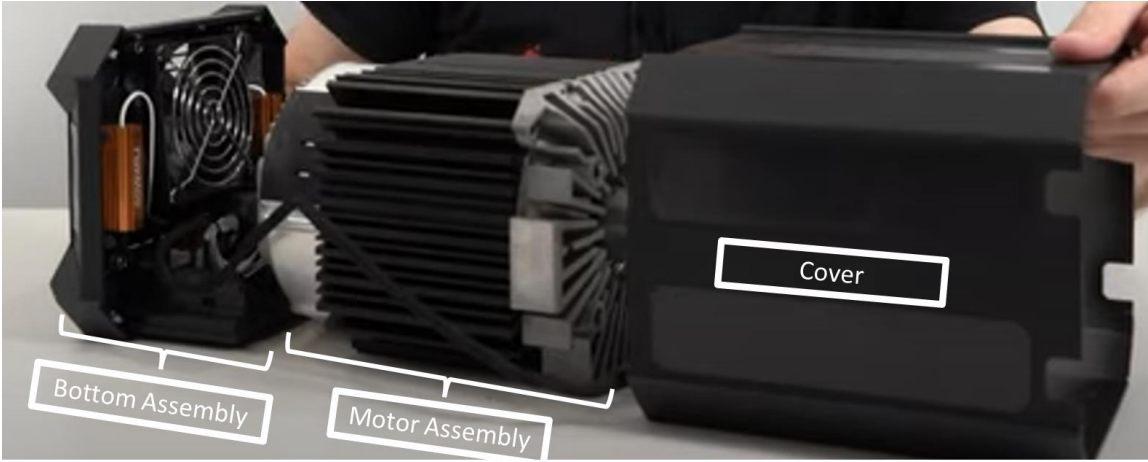
Figure 39 Fanatec Podium DD1/DD2 Teardown

2.3.4 Bottom Assembly

2.3.4.1 Cables

Undoing the screws on the back of the equipment we can see the power supply cable, some data cables connected to the motor and a data cable connected to the OLED visor on the front of the equipment.
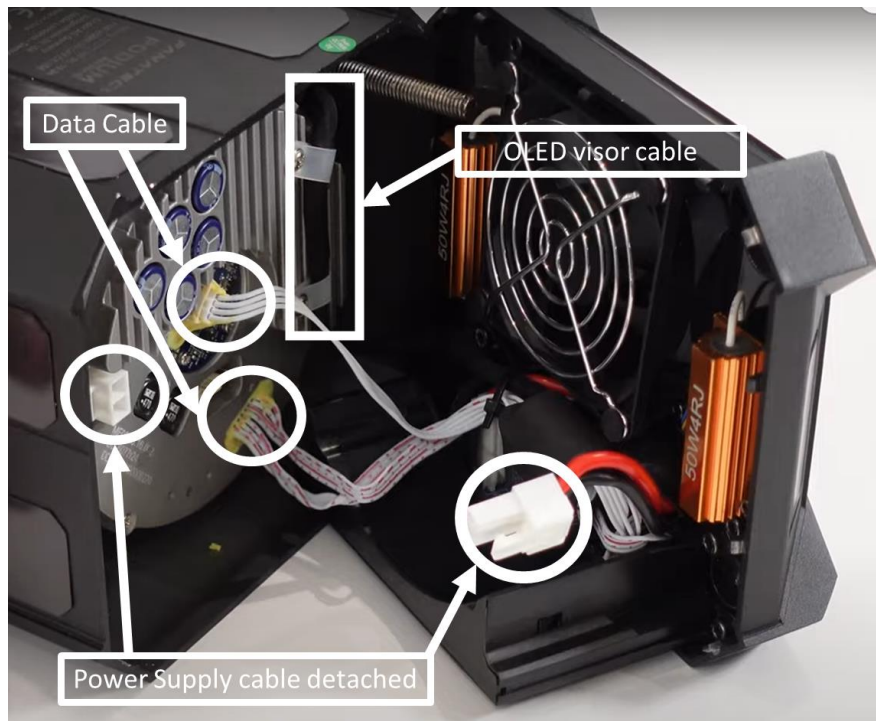
Figure 40 Fanatec Podium DD1/DD2 Cables

2.3.4.2 Components

Bottom part contains

- a PMW controlled Fan,
- two braking resistor which is meant to bleed off the voltage on the circuits created by the motor due to its inertia that makes it continues to rotate once the power supply has been switched off.
- PCB for controlling the Fan based on the measured temperature, and to contain the necessary circuit for the power supply and motor braking correct functioning

Figure 41 Electronic Components

The circuitry in PCB can be divided into two macro groups containing devices for realizing two different tasks, as shown in the figure below:
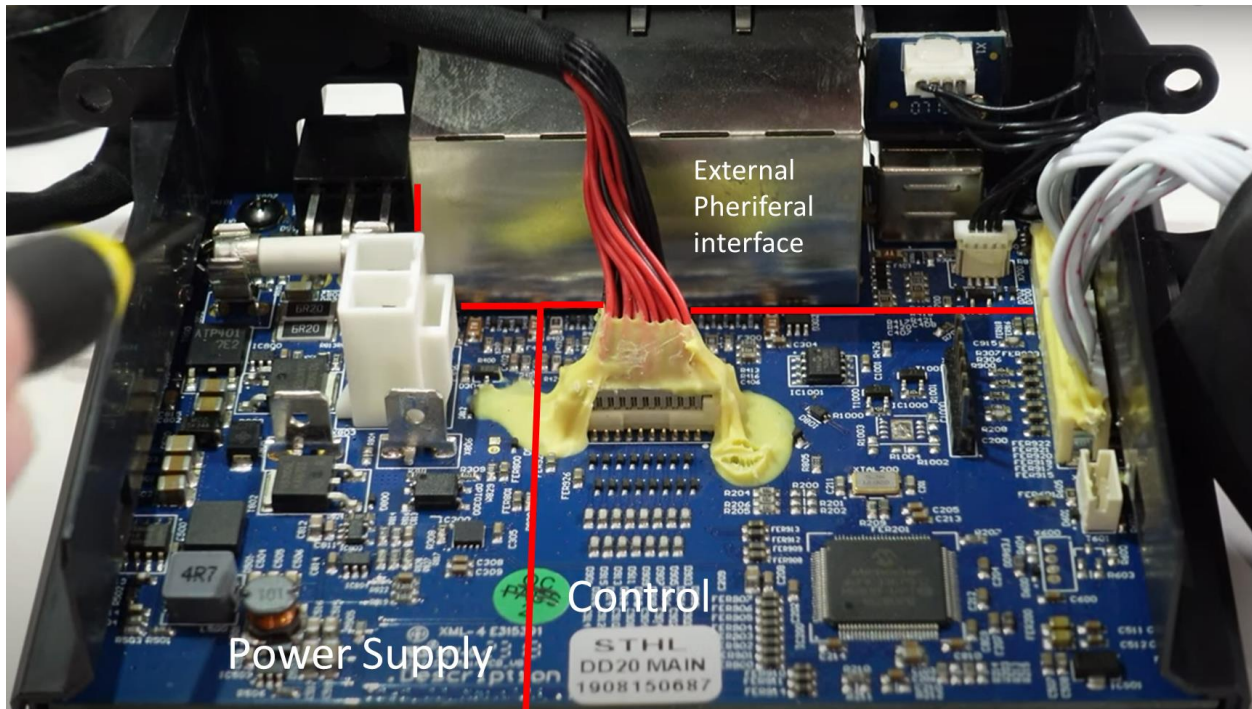
Figure 42 Fanatec Podium DD1/DD2 PCB

The microcontroller for controlling, through PWM signal, the motor and the fan is the chip called dsPIC33EP512MU810

2.3.5 Motor Assembly

2.3.5.1 Data Connection

Fanatec designed an optical transmitter/receiver for allowing communication through the several logic circuitries throughout the wheelbase, the transmitter is positioned on the bottom of the motor assembly, goes through a concentric path with the inductive coil and faces the receiver positioned concentrically in the opposite inductive coil (as in the picture shown in the next paragraph). [30]-[31]-[32]
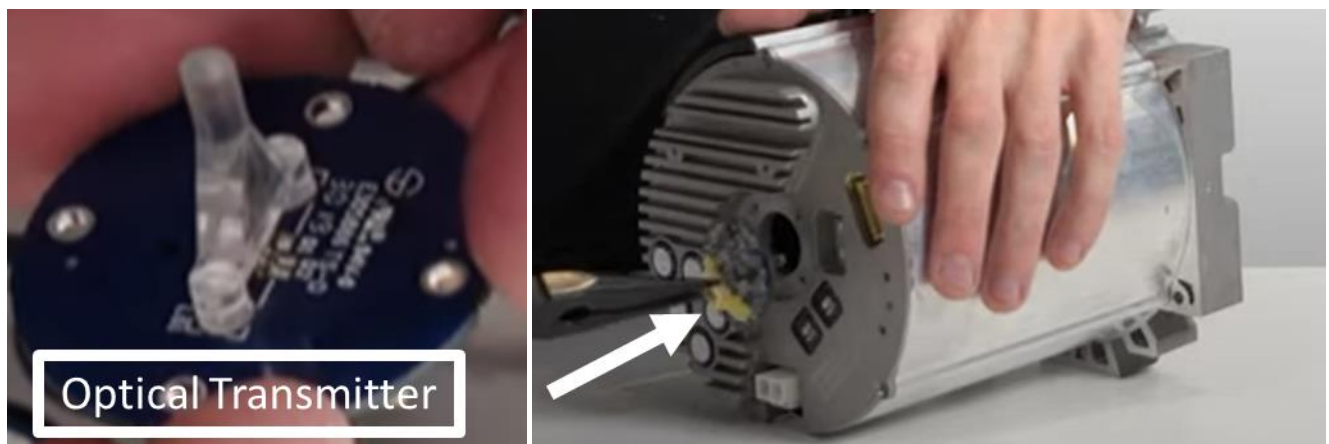
Figure 43 Fanatec Podium DD1/DD2 Optical Transmitter

2.3.5.2 Power Supply

The motor is power supplied through 2 coupled inductive coils. It allows the motor/ shaft to rotate without having any problem with the cable or any other mechanical component. [30]-[31]-[32]
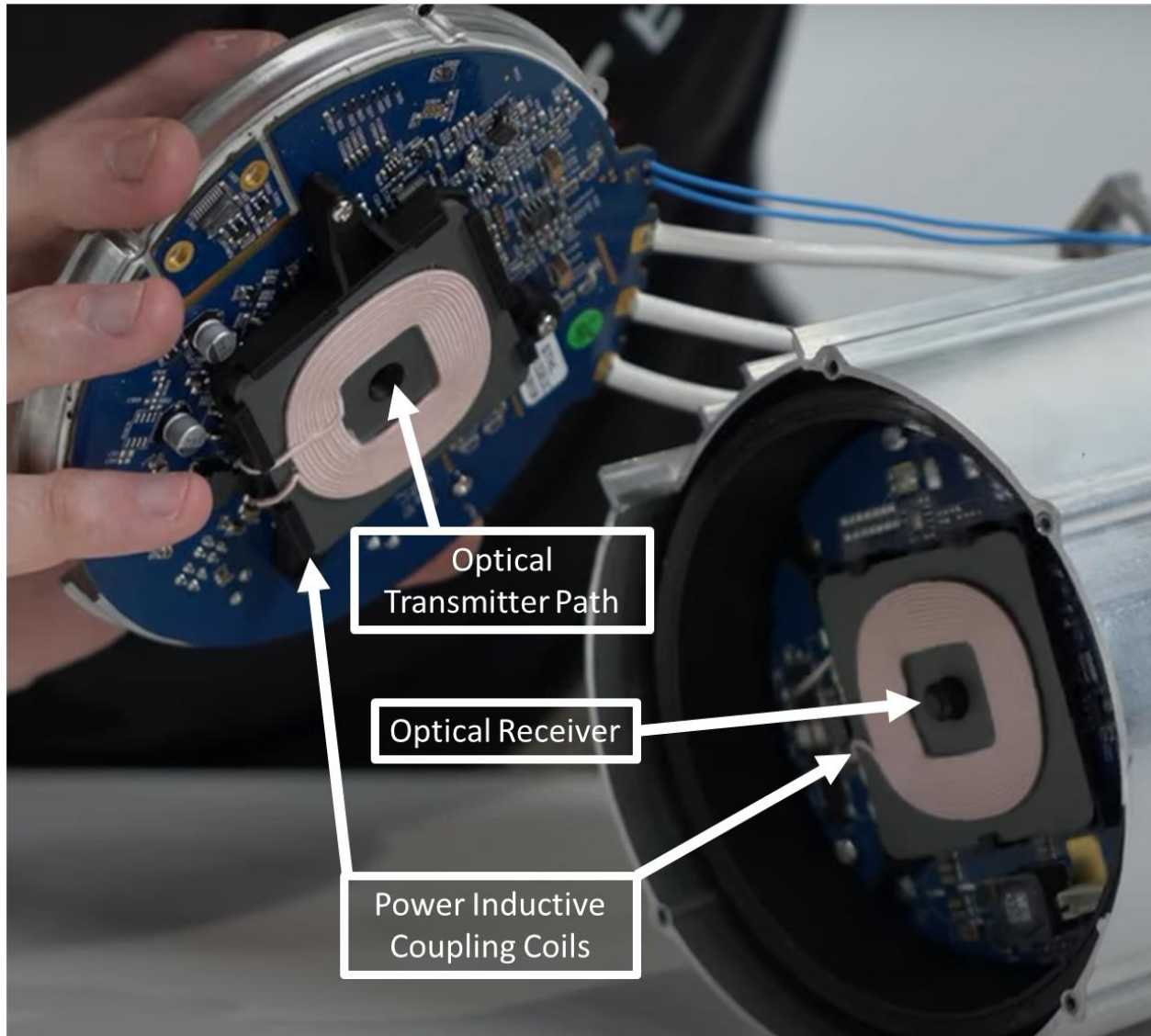
Figure 44 Fanatec Podium DD1/DD2 Power Supply

2.3.5.3 Hall Effect Sensor

Multi-position hall effect sensor by measuring the magnetic field of the magnetic strip can indicate the rotation angle of the shaft.

PCB containing the hall effect sensor chip faces the black plastic disk containing the magnetic field, making it possible for the sensor to measure the magnetic field. [30]-[31]-[32]
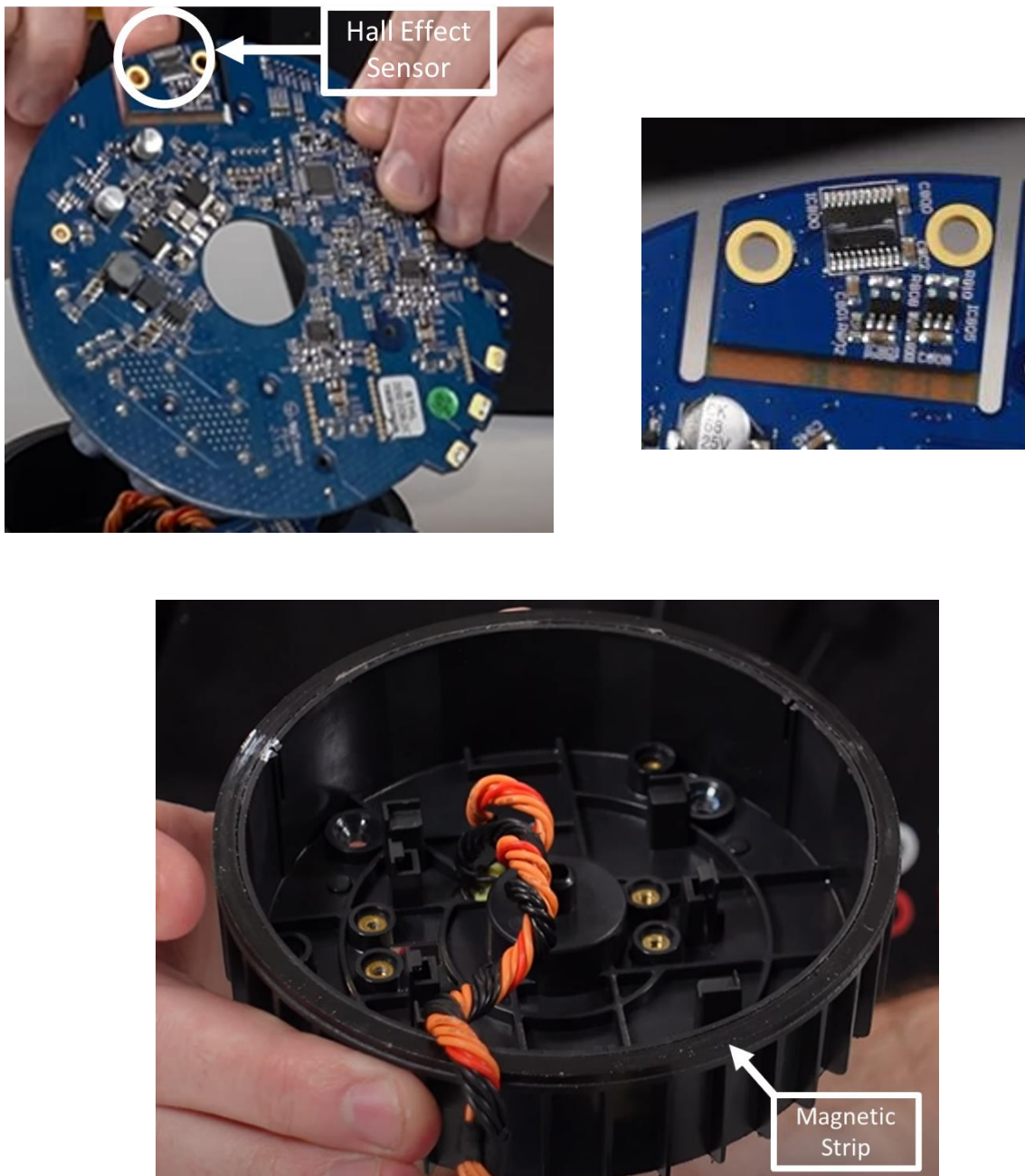
Figure 45 Fanatec Podium DD1/DD2 Hall effect Sensor Assembly

2.4 Simucube 2 PRO

Simucube 2 Pro is the world-class Direct Drive force feedback wheelbase.

The Simucube 2 Pro is built with an industrial motor with a robotics precision level, electronics and software are integrated to make room for a seamless monolithic design. Everything is optimized for performance at the highest level and with a latency of less than a millisecond.

Rigid mechanical coupling between wheel and base is the fundamental requirement for direct drive. Simucube 2 Pro was built to meet this requirement, even if it meant redesigning everything.

Simucube 2 Pro works with simulator games and rebuilds the authentic environment. Thanks to the Simucube's dedicated processor for motrol control and another one for interfacing with the PC simulator, the ultra-low latency is stable and consistent. With Simucube's award-winning feedback force processing, ultra-low latency mode and adjustable dynamic filters, Sim-Drive can achieve Realism.

Figure 46 Simucube 2 Pro

Base size: 130mm x 130mm x 270 mm

2.4.1 Simucube 2 Pro Teardown

Motor Control and Power Supply Cables
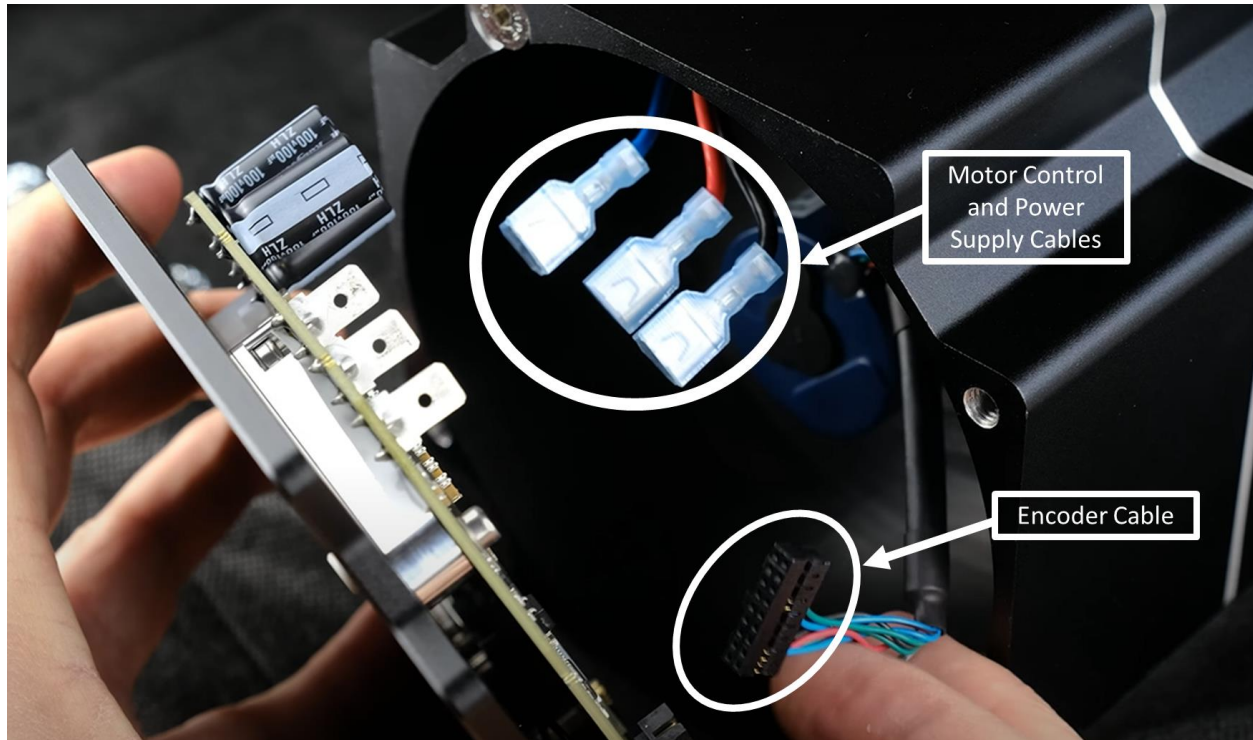
Encoder Cable

Figure 47 Simucube 2 Pro Cables

Starting from the back, once the cover is removed, we can identify four connectors, 3 for controlling and supplying the motor, the fourth connector for receiving data from the encoder.

Figure 48 Simucube 2 Pro Encoder

Simucube 2 Pro Direct Driver motor comes equipped with precision industrial robotics grade angle sensors with a resolution of 4.194.304 steps per revolution, namely, a Biss-C, a Chinese manufactured incremental encoder.

The quality of the angle sensor information has paramount importance when calculating natural physics effects and filters. Any imperfection of the sensor signal would feel like a distortion in reality. All Simucube 2's signal processing units are optimized to take full advantage of the unmatched sensor precision.

Moreover, the encoder is directly attached to the motor shaft and sends the signal to the board.
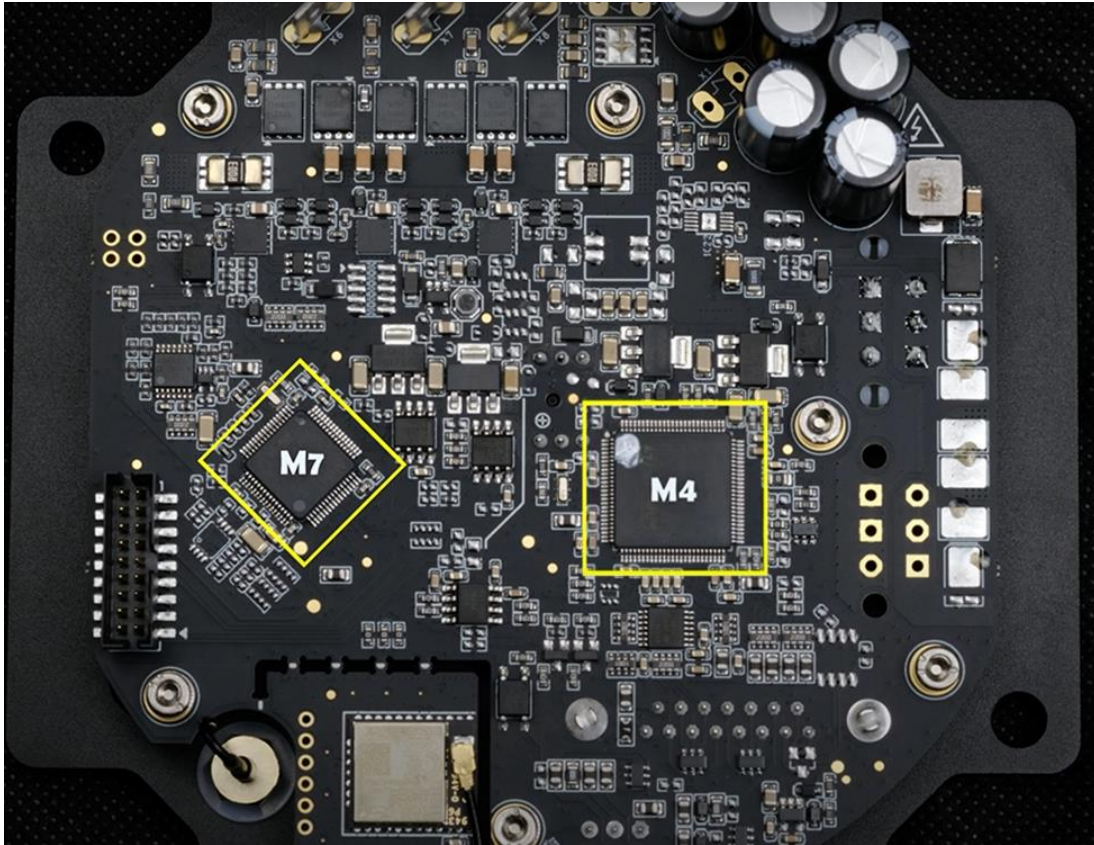
Figure 49 Simucube 2 Pro Processors

To unleash the full potential of the motor and to process signals at maximum precision, on the board are mounted two ARM dedicated processors. Simucube 2 has been given a dedicated 216 MHz real-time processor (ARM Cortex M7) in addition to a processor (ARM Cortex M4) 144 MHz dedicated to the PC-USB interface. Unique dual CPU architecture ensures zero impact on ultra-low latency performance even when all processing and simulator actions are running simultaneously. The new 216 MHz processor features superscalar ARM architecture, making it effectively four times faster than the 72 MHz processors of IONI drive in Simucube 1.
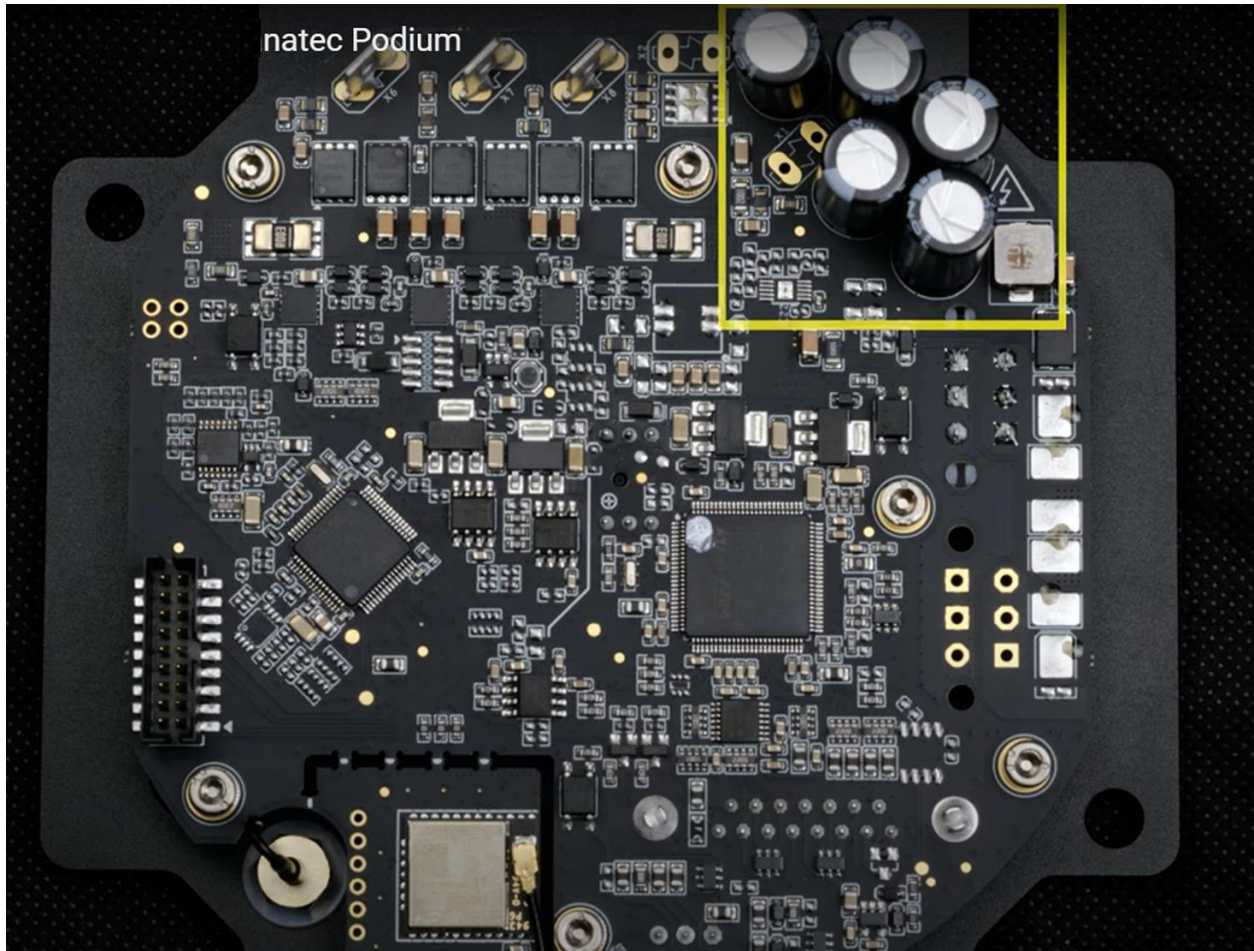
Figure 50 Simucube 2 Pro Capacitors for Power Supply Stabilization

On the upper right side of the board, there are 5 Japanese electrolytic capacitors of 100V and 100 µF for stabilizing the power supply.
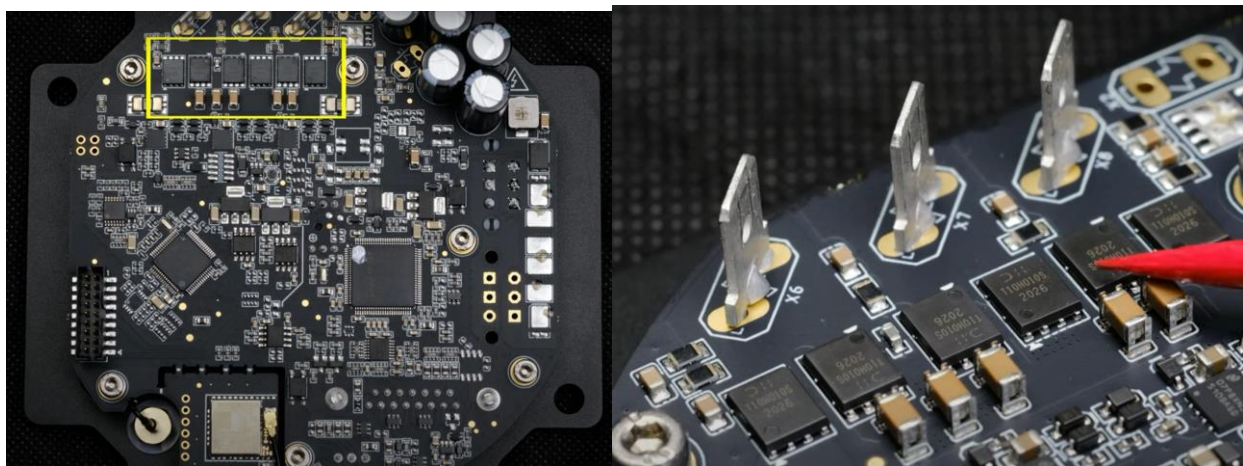
Figure 51 Simucube 2 Pro Mosfets for Motor Current Control

In the above picture is highlighted the group of Mosfets dedicated to controlling the current that supplies the motor. The Mosfets are oversized to ensure long durability.
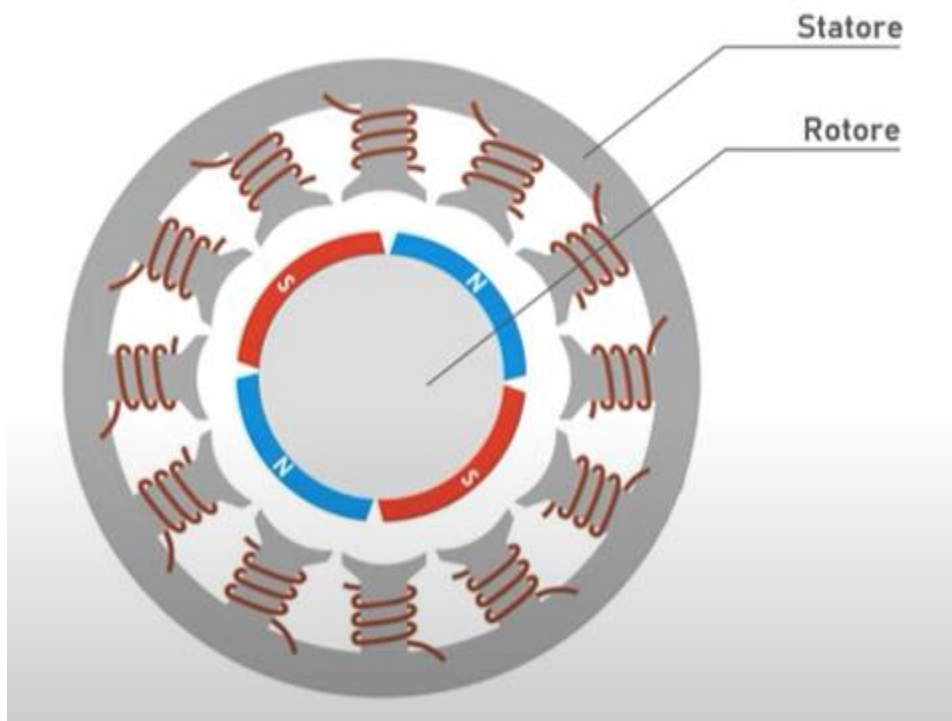
Figure 52 Inrunner DC Brushless Motor

Simucube developer team compared over 40 motors, hand-tested over ten of them, picked the best three motors, and finally customized them to suit flawlessly in direct drive racing simulation. SC2's latest generation inrunner brushless motor technology delivers unforeseen torque response rate and clarity. FEM optimized motor magnetic design yields practically zero torque ripple and magnetic cogging. Simucube 2 's are also individually tested and verified to exceed inhumanly tight tolerances in production. The motor can provide until 25Nm. [33]-[34]

2.5 Professional Context of Application

For a better understanding of the general context throughout the several possible applications, a survey was carried out with some company representatives of the sector.

DrivingItalia.NET, a leading portal in the simracing sector since 1999, after almost two years of development and testing at the Lanciano (CH) headquarters, in 2018 launched sim-racing services for professional driving simulation centres, open to all: Driving Simulation Center. The DSC package provides a wide range of services for a turnkey business, for the opening of a high-level virtual driving center!

DrivingItalia.NET uses two different simulators a Thurstmaster T-300 and a Thurstmaster T-500.

Arc- team Engineering, is an engineering group specialized in the design, assembling, and production of high-performance drive simulators. Besides the engineering, it was created a training simulation centre where many F1 pilots train. Arc-team for high-level simulators design uses Fanatec DD1 or Simucube 2.

Simulator Giantruck was founded in 2013 to build dynamic, professional, and low-cost driving systems. The brand quickly expands its designs and creates everything within the company. Progress within the company goes faster and faster and designs of new simulators come to life such as truck simulators, forklifts simulators, flight simulators, motorbike simulators (always dynamic and with movement). Simulator Giantruck uses mainly Fanatec DD2 and SimuCube 2.

3 Benchmark and Cataloguing

To catalogue the products in categories, indicating the pros and cons are useful for better understanding the different solutions realized until now. Moreover, identifying the best product (benchmark) lead us to elaborate correct specifications for kicking off the project of developing an improved force-feedback steering wheel.

3.1 Cataloguing

Force Feedback is mostly generated with three different mechanisms [4]:

3.1.1 Belt-Driven:

Most sim racing wheels on the market today are belt driven, and there is a good reason for this. Belt driven technology provides a much cheaper option when implementing force feedback through the wheel rim due to utilizing a small motor.

The price reduction in the small motor used to power belt-driven sim wheels allows these products to be targeted at gamers who are looking to buy their first wheel. And these types of products are often the first step into the world of sim racing for many.

Belt driven wheels work by utilizing a belt and pulley system and a small motor. The small motor generates the force feedback, which is then passed through the belt to the wheel rim. By utilizing a belt and pulley the effects that the small motor generates can be amplified to produce much more torque, and stronger force feedback. It isn't unusual for the belt to boost the motor's torque by up to 20 times.

The main downside to boosting the motor's actual force feedback by this much is that the force feedback becomes less accurate. A belt-driven wheelbase will almost always produce smoother force feedback than a gear drive wheelbase.

However, the downside is that the smoothness is a result of the belt absorbing some of the force feedback. The high-frequency force feedback is lost in this absorption, meaning you aren't getting the full force feedback intended.

Advantages:

- Utilizes a small motor, keeping the cost down.
- Smoother force feedback than gear driven wheels.

Disadvantages:

- The belt can sometimes absorb some of the force feedback, meaning, less feedback is sent through the wheel.
- Belts can wear or stretch over time, resulting in product failure.
- The small, low-cost motor can produce lacklustre force feedback.
- Less efficient due to belt friction and additional pulleys.

3.1.2 Gear-Driven:

Gear-driven wheels work in a very similar way to their belt-driven counterparts. The small motor is attached to a series of gears which translate and amplify the force feedback effect. This once again produces much more torque than the motor could on its own and in turn, stronger force feedback.

The main disadvantage of gear-driven wheels lay in the gears themselves. Geared systems can be inherently clunky due to the metal-on-metal contact of two spinning gears. Depending on the sim racing wheel you buy, you will occasionally feel the gears grinding and jumping through heavy force feedback.

Advantages:

- Utilizes a small motor, keeping the cost down.

Disadvantages:

- The small, low-cost, motor can produce lackluster force feedback.
- Gears often grind or jump, producing torque spikes.

3.1.3 Direct Drive:

Direct drive wheels connect the wheel rim directly to the motor shaft. The motor itself is much larger than those found in belts or gear-driven racing wheels. This has to be the case as there are no belt or gear systems to amplify the power which the motor outputs.

The size and power of these motors are what cause direct drive wheels to be able to create such high levels of torque. I mean, we've all probably seen top sim racing YouTubers battle 100% force feedback challenges with direct drive wheels. These alone show how powerful direct drive wheel motors can be.

As mentioned above, the large motor is connected directly to the wheel rim sending all of the force feedback directly into your hands. This not only gives a much superior level of torque and

strength to the wheel. It also means that none of the force feedback effects, which are generated, are lost in the gear/belt connections. [5]

Advantages:

- Much stronger force feedback.
- No loss of detail, meaning much better force feedback.
- No maintenance or belt wear to deal with.
- Transmits extremely high-frequency force feedback with no detail loss (better output resolution).

Disadvantages:

- Much more expensive due to the much larger motor and electronics for the high-performance controller.

In 2015, a preliminary comparison of gear-driven and direct drive wheels in the 0-30Hz frequency range, for a study on hard real-time multi-body simulation and high-fidelity steering wheel force feedback, concluded that direct-drive wheels are preferable.

3.2 Benchmark identification

Performance indicators of sim racing wheels include detail and fidelity of force feedback, smooth torque transmission, rotary encoder resolution, torque range, drivers and digital signal processing with control electronics, low inertia, damping, precise positioning and latency.

For the sake of simplicity, it will be analyzed only 3 features that are representative of some indicators:

Manufacturer	Product	Peak Torque	Resolution	Motor
THRUSTMASTER	T-300	3,9 Nm	65.536 steps	DC Brushless Motor B4260M-S03
LOGITECH	G29	2,1 Nm	256 steps	Standard DC Brushed Motor labeled RS555SH-15260
FANATEC	DD1	18 Nm	65.536 steps	Tailor-made Outrunner Servomotor
FANATEC	DD2	24 Nm	65.536 steps	Tailor-made Outrunner Servomotor
SIMUCUBE	Simucube 2 Pro	25 Nm	4.194.304 steps	Tailor-made Inrunner Servomotor

It's possible to notice, from the comparison table above, that the direct drive steering wheels have the best performances. Direct drive wheel tailor-made motors can provide a wider torque range as well as sophisticated electronics along with high-resolution position sensors to ensure a more precise positioning and accurate visual feedback.[35]-[36]

4 Steering System Model

In this chapter, the steering system used in this thesis is described. As mentioned before, steering system modelling is one of the most important issues in driving simulation. The high fidelity of steering system simulation is useful to achieve a high reality steering feel for the driver during driving simulation. The steering system modelled during this project consists of two main parts: steering geometry and steering wheel feedback torque. Steering geometry is created to transmit the steering wheel angle applied by the driver as an input to virtual wheels angles as output. Steering wheel feedback torque has the main purpose of transmitting the torque created in a tire (self-aligning torque, friction torque…) to the steering wheel. In other words, the steering system model receives the steering wheel position which is applied by the driver as input and provides the steering wheel feedback torque as output.

4.1 Steering System Overview

The steering system transfers the steering wheel angle to the wheels through a mechanical system composed of a series of rods and pivots linkages. In this case, when the driver turns the steering wheel, the steering wheel's rotation is transmitted through the steering column (steering shaft) to the pinion, the pinion and rack convert the rotation to the linear displacement. The linear movement is transferred to the steering arm through the tie roads and generates the steering angle in the wheels. It is important to notice that the steering wheel angle and wheel angle relates via a steering ratio coefficient. A rack and pinion steering system is commonly used in conventional cars. In this case, the power steering assistance system is used as well as the rack and pinion system. A power steering assist system helps drivers by applying an assistance force (or torque) on the rack (or on the steering column) according to the resistant torque measured by the torsion (angular displacement) measured on the torsion bar placed close to the pinion on the lower end of the steering column. The power steering assistance system can be hydraulic or electric having a motor/pump and a control unit so that the control unit calculates if steering assistance is required for the driver.

Two simplified and schematic draws of a rack and pinion steering system are shown below:
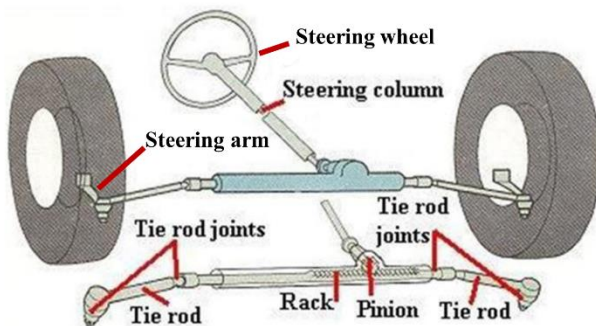
Figure 53 Rack and Pinion Steering System
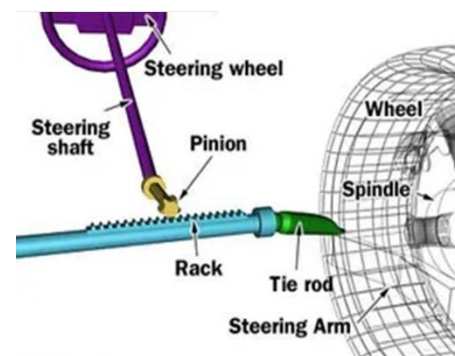
Figure 54 Rack and Pinion

49

The mechanical linkage between the steering system usually conforms to the Ackermann steering geometry.

Ackerman steering geometry is the term used to describe the behaviour of the front wheel when the vehicle is driven around a corner. In the corner when the front tires turn, the radius of the inner wheel is smaller than the outer wheels and that means the steering wheel is needed to generate the wheel angle for the inner wheels which are larger than the outer wheels, otherwise the inner wheel tends to slide over the road [6]. The Ackerman geometry neglects the effect of road on tires, so it is not completely suitable for modern cars. The wheel's behaviour interface corner turning can be seen in the following figure.
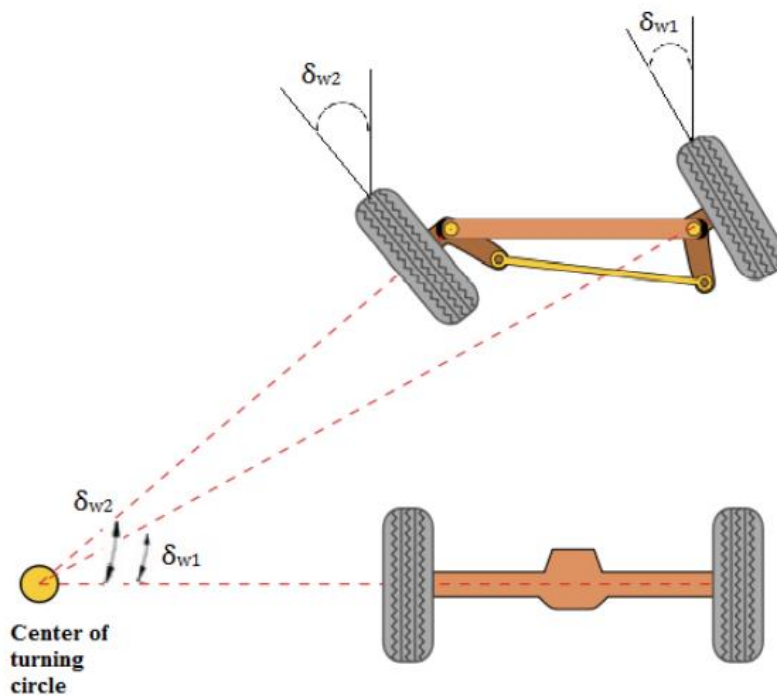
Figure 55 Ackerman steering geometry

As can be seen in the Figure, the inner wheel angle is larger than the outer wheel, when the vehicle turns around a circle.

$$\delta_{w_2} > \delta_{w_1}$$

It is important to notice that the wheels behaviour analysis is a very important point to accurately simulate tire forces. For this reason, all the parameters which can affect the tires must take into account in tire modelling. The toe angles for tires are other main characteristics of tires that should be considered in the modelling of the tire. Toe angle is the initial symmetric steering angle that each tire makes with the longitudinal axis of the vehicle, even when the steering wheel is not turned. The steerable wheels are set to have the toe angles as a function of the static

steering geometry and kinematic effects of the steering system and tires. Regarding the application of the steering system, the toe angle can be positive or negative. It can be measured as an angular deflection of the tire at the front of the tire.

Toe-in (positive) can be useful in order to improve the vehicle stability of the road car for straight driving and vehicle response in a turn.

Toe-out (negative) is used for racing cars only because it can increase the stability of the vehicle in turning position, but it is unstable for straight driving.
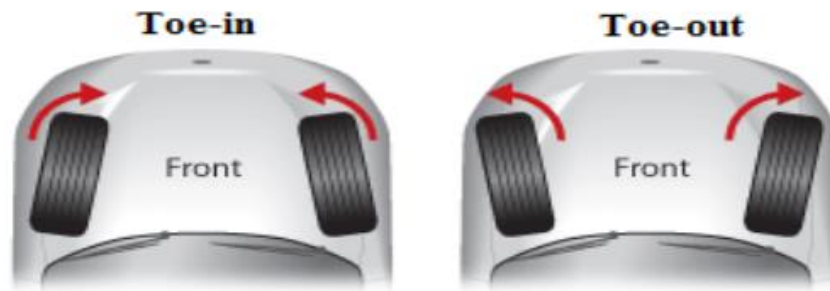
Figure 56 Toe-in and Toe-out

Other properties that should be considered when modelling a steering system are the effect of caster angle, camber angle and kingpin inclination.

Caster angle is the angular displacement of the steering axis from the vertical axis in the longitudinal plane (on the side view of the tire).
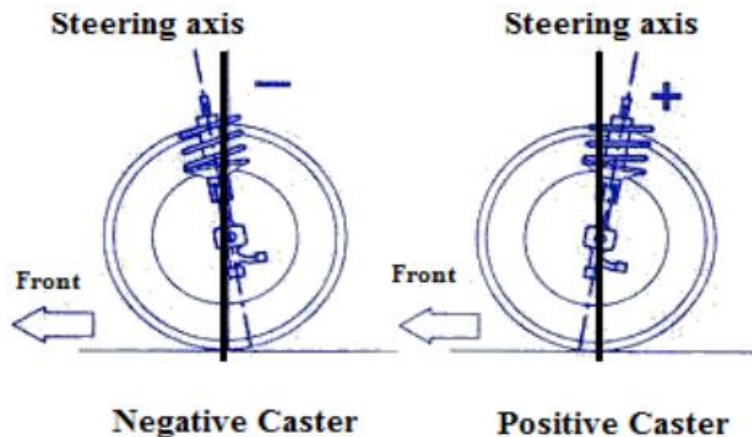
Figure 57 Caster Angles

Caster angle affects the steering feel by creating a self-centring torque to reduce the toughness of steering. For example, when the caster angle is positive and the wheel is steered, the lateral forces will create a torque around the steering axis and will increase the self-aligning torque of

51

the tire. Increasing self-aligning torque causes the steering wheel to align quickly. When the caster angle is negative the lateral forces will produce a torque that helps to steer. [7].

The camber angle is the angle made by the wheel between the vertical axis of the wheel and the vertical axis of the steering axis at the top of the front or rearview.
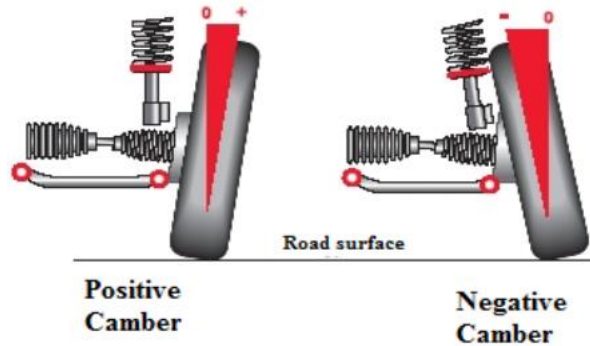
Figure 58 Chamber Angle

It is important to notice that the cornering force of the tires is mostly dependent on their angle relative to the road surface condition so that the generated maximum cornering force is achieved at a small negative camber angle.

Kingpin angle (inclination) is the angle between the kingpin axis and the vertical axis of the tire. The kingpin axis is the line between the lower and upper ball joints of the wheel's hub. The kingpin angle affects the scrub radius at the contact patch of the wheel. The scrub radius is the distance, in the range of some millimetres, between the kingpin axis and the tire's contact point with the road, where the kingpin axis and contact patch theoretically touch the road surface.
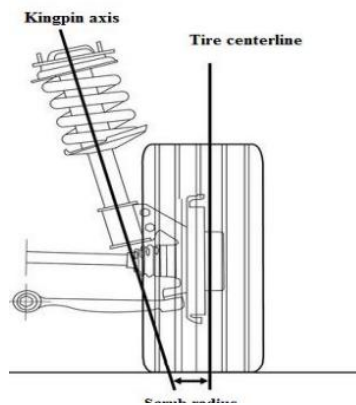
Figure 59 King Pin and Scrub Radius

The effect of the kingpin angle is usually discussed in terms of the scrub radius offset which determines the value of the self-aligning torque when the wheels are turned. For the zero-scrub radius, no reaction will transmit to the steering wheel and the driver is not able to perceive the change in the vehicle's lateral offset. In the case of the positive scrub radius (many conventional cars have a positive scrub radius offset), the wheels are returned to the straight position quickly. In the case of the negative scrub radius (some modern cars have a negative scrub radius offset), the longitudinal forces will generate a torque that increases the steering of the wheels in a longitudinal direction. [8]

4.2 Steering system forces and torques

In the modelling of the steering wheel feedback torque, six sources of forces and torques were taken into consideration, they are described as follows:

Longitudinal forces ($\vec{F}_x$) (or Tractive Force): The longitudinal forces are generated between tire and road, due to dynamic and adhesion friction forces.

$$F_x = -\mu * N$$

where $on\mu = \mu_{friction} + \mu_{adhesion}$ is the friction coefficient and N being the normal reaction force.

The friction coefficient μ, consequently F_x, varies as a function of slip rate s.

$$s = \begin{cases} \dfrac{v - R.\omega}{v} & \text{,for braking} \quad (R.\omega < v) \\[2mm] \dfrac{R.\omega - v}{R.\omega} & \text{,for acceleration} \quad (R.\omega > v) \end{cases}$$

where ω is the rotational velocity and R is the radius of the tire, v is the longitudinal velocity of the vehicle. F_x trend concerning s is represented below:
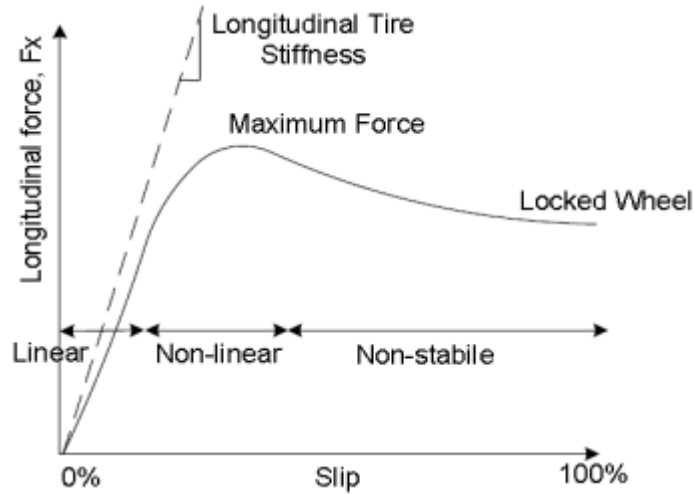
Figure 60 Longitudinal force - slip angle graph

The corresponding torque in the tire due to a longitudinal force is the product of the longitudinal forces and the moment arm (scrub radius), as follows:

$$T_{Long} = F_x * (scrub\ radius)$$

Lateral forces ($\vec{F}_y$): The lateral force on a tire is proportional to the slip angle of the tire since its generation depends on the magnitude of lateral deformation of the treads in the contact patch.
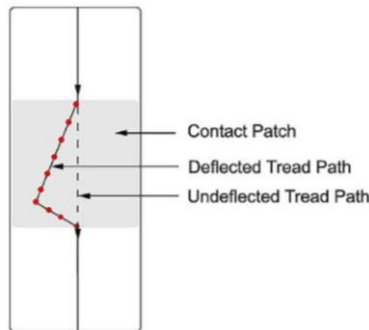
Figure 61 Contact Patch deformation during a curve

Slip angle is the angle formed by the direction of wheel travel and the direction of wheel heading, or better the angle between the forward velocity vector $\vec{v}_x$ and the vector sum $\vec{v}$ of wheel forward velocity $\vec{v}_x$ and lateral velocity $\vec{v}_y$, as defined in the image below [9]:
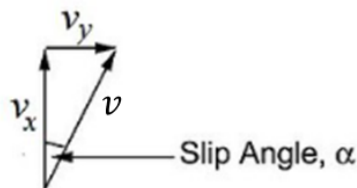
Figure 62 Slip Angle

54

These forces create a torque at the contact patch of the tire with the ground. The lateral forces act on a lever arm $\vec{L} = \vec{L}_{dist} + \vec{L}_{trail}$ which is the sum of the static offset (L_{dist}) and pneumatic trail (L_{trail}).

The corresponding torque can be written as:

$$T_{Lat} = F_y * L$$
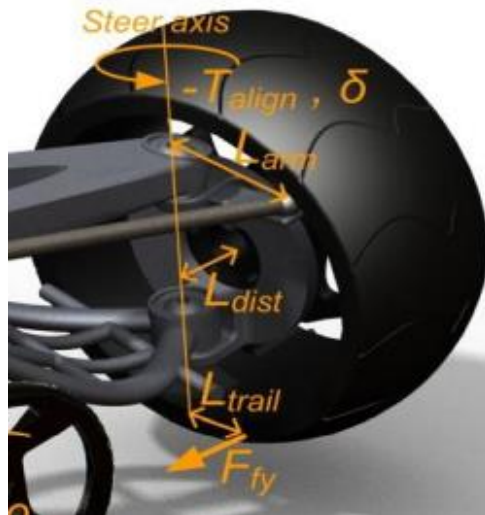
Figure 63 Wheel Hub

Linear damping (D): linear damping of the steering column damper (D_s) and the rack (D_r) generates an opposing torque for the steering wheel rotation direction. The torque due to the linear damping is a product of the total damping coefficient and the rotational speed of the steering wheel.

$$T_{Damp} = D * \dot{\theta}$$

Inertial effects (J): inertial effects of the steering system component such as the steering column, the rack-pinion mass, the wheel carriers and the hubs increase the resisting torque in accelerating and braking.

$$T_{Inertia} = J * \dot{\theta}$$

Front lift: suspension compliance of the car generates the additional steering angle in the wheels. In order to achieve the high-reliability model of the vehicle steering system for the Chalmers driving simulator, this part of the model was developed. In this model, the suspension linkage is used to connect the wheels to the body of the car. As mentioned previously, the front wheels of the cars are lifted or lowered due to the caster and kingpin (KPI) angles. The rack and pinion mechanism are used to calculate the proper suspension compliance effect.

Friction: friction is one of the important components of the steering system modelling which should be considered in the modelling process. In the model used by Benito& Nilsson, constant friction is applied as dry friction between the road surface and the steerable wheels. In addition to the force coming from the road-tire interaction, there is the friction that comes from the rack-pinion contact and bearings of the steering systems. Dahl friction model is used to model the rack-pinion component friction because it is simple and most useful. The Dahl friction model proposed that the relationship between frictional force and position would be analogous to a stress-strain curve and hysteresis. Modelling of the stress-strain curve can be extracted as:

$$
\dot{F}_f(t) = \sigma \cdot \left[1 - \frac{F_f(t)}{F_c} \cdot sign(\dot{x}(t)) \right]^\lambda \cdot sign\left(1 - \frac{\dot{F}_f(t)}{F_c} \cdot sign(\dot{x}(t)) \right) \cdot \dot{x}(t)
$$

where σ is the stiffness coefficient, $F_f(t)$ is the Dahl friction force, F_c is the Coulomb friction force, $\dot{x}(t)$ is the velocity between two surfaces and λ is the shape parameter.

4.3 Steering System Modelling

The steering system will be modelled based on the following hypotheses:

- The variation of the angular ratio of all universal joints has been neglected.
- The torsion bar is modelled as a massless spring.
- Both rack (D_{rack}) and torsion bar (D_{TB}) damping are considered
- The length of the steering arm lever is considered constant SAL
- The damping and the inertia of the steering wheel and of the steering column are included in the terms and of the steering column are included in the terms J_{sw} and D_{sw} .
- Power assist force is considered applied on the rack (F_{servo})

The steering system model considered is based on the torques and forces and is presented in the following figure:
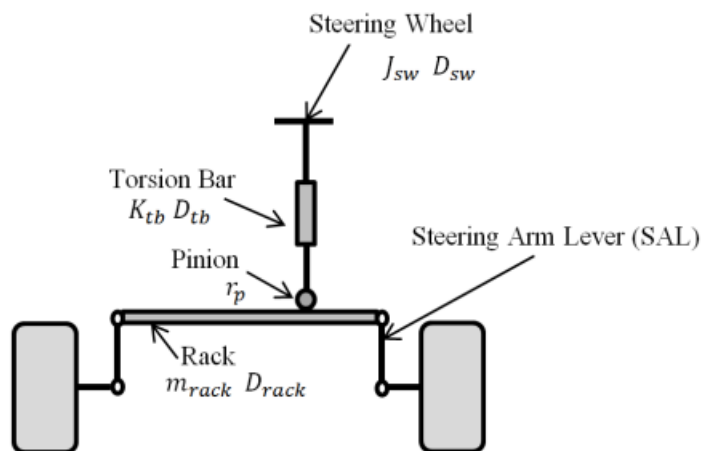
Figure 64 Steering System

For calculating these forces and torques consider the TMEasy tire's model, the starting point is to compute the resistant torque produced by the tire forces around the steering axis, taking into account both caster and kingpin angles. This has been done by following ISO 8855 regulation.

The longitudinal and lateral forces of the front tires (i=1,2) can be calculated by using:
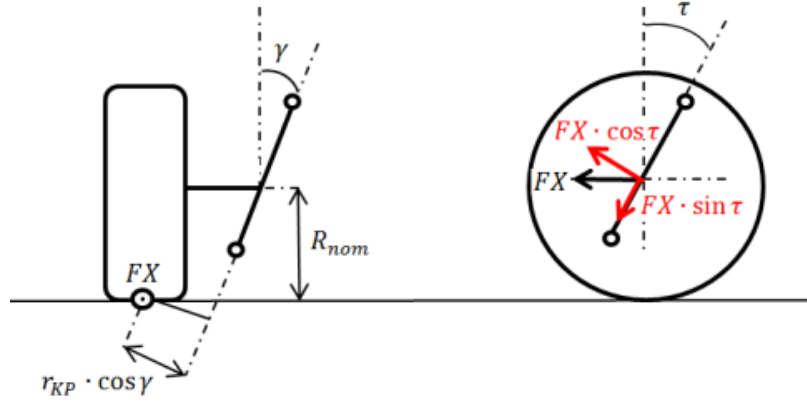
Figure 65 Longitudinal Forces System of forces

$$\sum F_x = m \cdot a_x \;\; \rightarrow \;\; F_{x_{tot}} = \left(F_{x_i} - F_{rolling_i}\right) \cdot \cos \delta_{w_i} - F_{y_i} \cdot \sin \delta_{w_i} \quad , with \; i = 1,2$$

$$F_{rolling_i} = -f_r \cdot g \cdot \min\left(1, v_{x_i}\right) \cdot sign\left(v_{x_i}\right)$$

Where $F_{rolling}$ is the force generated by tire rolling resistance e f_r is the rolling resistance coefficient, the m is the vehicle curb mass adding the driver mass (75Kg), g is gravity acceleration and v_x is the longitudinal axis of car's velocity.

The total resistant torque $T_{x_{st-axis}}$ generated around the steering axis due to $F_{x_{tot}}$ can be computed as:

$$T_{x_{st-axis_i}} = F_{x_{tot_i}} \cdot \cos \tau_i \cdot \left[r_{KP} \cdot \cos \gamma_i + R_{nom} \cdot \sin \gamma_i\right]$$
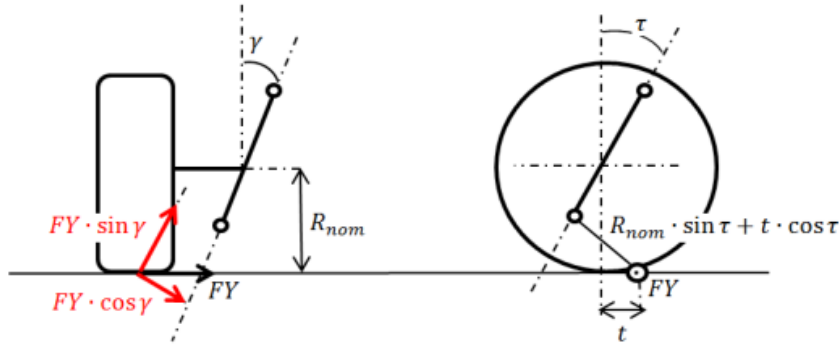
Figure 66 Lateral System of Forces

$$\sum F_y = m \cdot a_y \;\; \rightarrow \;\; F_{y_{tot}} = F_{y_i} \cdot \cos \delta_{w_i} + \left(F_{x_i} - F_{rolling}\right) \cdot \sin \delta_{w_i} \quad , with \; i = 1,2$$

The total resistant torque $T_{y_{st-axis}}$ generated around the steering axis due to $F_{y_{tot}}$ can be computed as:

$$T_{y_{st-axis_i}} = F_{y_{tot_i}} \cdot \cos\gamma_i \cdot [t \cdot \cos\tau_i + R_{nom} \cdot \sin\tau_i]$$

$$t = t_p + t_m$$

The vertical force and torque generated due to FZ are calculated starting from the following figure:
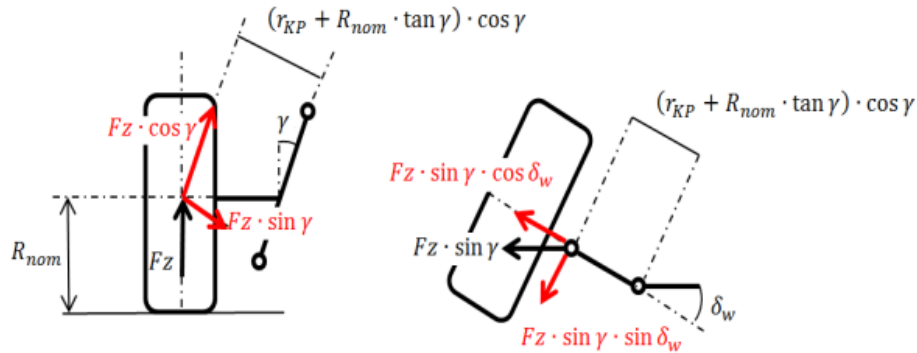
Figure 67 Vertical System of forces

The torque produced around the steering axis $T_{z_{st-axis}}$ due to $F_{z_{tot}}$ can be computed from:

$$T_{z_{st-axis_i}} = F_{z_{tot_i}} \cdot \sin\gamma_i \cdot \cos\tau_i \cdot \sin\delta_{w_i} \cdot \{\cos\tau_i \cdot [r_{KP} + R_{nom} \cdot \sin\tau_i]$$

So, the total resistant torque generated around the first ($T_{st-axis_1}$) and second ($T_{st-axis_2}$) steering axis can be computed as:

$$T_{st-axis_1} = -T_{x_{st-axis_1}} + T_{y_{st-axis_1}} + T_{z_{st-axis_1}}$$

$$T_{st-axis_1} = -F_{x_{tot_1}} \cdot \cos\tau_1 \cdot [r_{KP} \cdot \cos\gamma_1 + R_{nom} \cdot \sin\gamma_1] + F_{y_{tot_1}}$$
$$\cdot \cos\gamma_1 \cdot [t \cdot \cos\tau_1 + R_{nom} \cdot \sin\tau_1] + F_{z_{tot_1}} \cdot \sin\gamma_1 \cdot \cos\tau_1 \cdot \sin\delta_{w_1} \cdot \{\cos\tau_1$$
$$\cdot [r_{KP} + R_{nom} \cdot \sin\tau_1]$$

$$T_{st-axis_2} = -T_{x_{st-axis_2}} + T_{y_{st-axis_2}} + T_{z_{st-axis_2}}$$

$$T_{st-axis_2} = -F_{x_{tot_2}} \cdot \cos\tau_2 \cdot [r_{KP} \cdot \cos\gamma_2 + R_{nom} \cdot \sin\gamma_2] + F_{y_{tot_2}}$$
$$\cdot \cos\gamma_2 \cdot [t \cdot \cos\tau_2 + R_{nom} \cdot \sin\tau_2] + F_{z_{tot_2}} \cdot \sin\gamma_2 \cdot \cos\tau_2 \cdot \sin\delta_{w_2} \cdot \{\cos\tau_2$$
$$\cdot [r_{KP} + R_{nom} \cdot \sin\tau_2]$$

The resistant forces acting on the rack transmitted through the lever arm are then:

$$F_{r_i} = \frac{T_{st-axis_i}}{SAL}, for\ i = 1,2$$

The rack-pinion free body diagram is shown below:
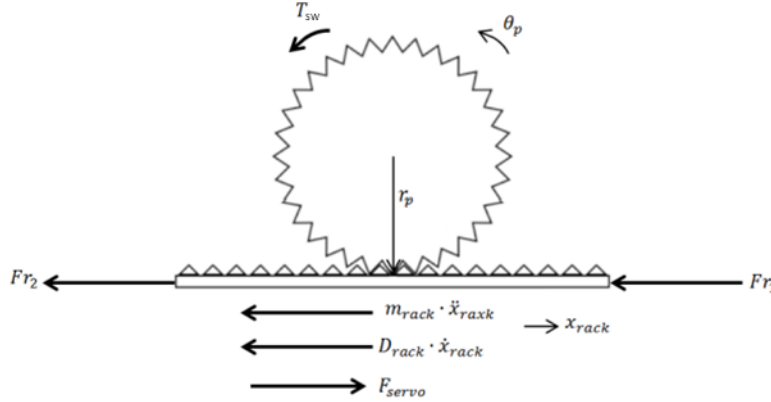
Figure 68 Rack and Pinion Force Balance

The total force transmitted by the pinion to the rack is equal to:

$$F_p = m_{rack} \cdot \ddot{x}_{sw} + D_{rack} \cdot \dot{x}_{sw} + \left(F_{r_1} + F_{r_2}\right) - F_{servo}$$

Now that the forces acting on the rack are known, it is possible to compute the torque acting on the steering wheel, which depends on the torque generated by F_p, the damping and inertia properties of the steering wheel and steering column and the servo assistance.

$$T_{sw} = J_{sw} \cdot \ddot{\theta}_{sw} + D_{sw} \cdot \dot{\theta}_{sw} + F_p \cdot r_p + T_f$$

where T_f is the torque produced due to friction.

4.3.1 Friction Modelling

Friction has an important influence on steering feel, especially in the so-called centre driving. This driving condition is the one in which the vehicle is driven with a small steering angle, for instance when it is driven in a straight line and a small movement of steering is needed to change trajectory. Friction mainly comes from the rack-pinion contact and through the bearings of the different components and can be modelled in different ways. An overall view on this topic can be found in [10]. For this thesis, a Dahl friction model has been adopted, mainly because it is simple, computationally fast and offers a good description of the phenomenon. The Dahl model was developed for the purpose of simulating control systems with friction. The starting point for

60

Dahl's model is the stress-strain curve in classical solid mechanics. When subject to stress, the friction force increases gradually until rupture occurs. Dahl modelled the stress-strain curve by the following differential equation:

$$\dot{F}_f(\text{t})=\sigma \cdot \left[1 - \frac{F_f(t)}{F_c} \cdot sign(\dot{x}(t))\right]^{\lambda} \cdot sign\left(1 - \frac{F_f(t)}{F_c} \cdot sign(\dot{x}(t))\right) \cdot \dot{x}(t)$$

Where:

$F_f(t)$ is the Dahl friction force

F_c is the Coulomb friction force

σ is the stiffness coefficient

λ is the shape parameter

$\dot{x}(t)$ is the relative velocity between the two surfaces

The Dahl friction model is a generalization of ordinary Coulomb friction and so it does not capture the Stribeck effect. Anyway, the Stribeck effect in a steering wheel is usually too low that the driver does not perceive it, so there is no need to model it. What is important is to model the hysteresis in the system. This model expresses the friction force only in function of the displacement: this means that the force is position-dependent. In the steering system, instead of having $F_f(t)$, F_c and $\dot{x}(t)$, the correspondent variables are the steering wheel friction torque $T_f(t)$, the steering wheel angular velocity $\dot{\theta}_{sw}$ and the Coulomb friction torque level T_c . In particular, the Dahl model used in this thesis has, for sake of simplicity and for computational reasons, a shape parameter $\lambda = 0$.

$$\dot{T}_f(\text{t})=\sigma \cdot sign\left(1 - \frac{T_f(t)}{T_c} \cdot sign(\dot{\theta}_{sw}(t))\right) \cdot \dot{\theta}_{sw}(t)$$

The stiffness coefficient for the steering wheel can be computed from the equation:

$$\sigma = \frac{2 \cdot D_{sw} \cdot K_{sw}}{\sqrt{\frac{K_{sw}}{J_{sw}}}}$$

4.3.2 Power Assisted Steering modelling (PAS)

The reason for which power steering is needed is mainly to take out the effort during parking and slow-speed manoeuvring and to reduce efforts when completing a severe cornering or correction of a car's attitude at medium speeds. Power steering has now become a positive necessity on

many large modern cars which have high front axle weights, large section tires, and now more frequently, front-wheel drive. It also improves safety by enabling the car to be rapidly manoeuvred out of difficulties and helps the car to be controlled in unexpected situations. Good PAS reduces driver fatigue and contributes to safety in this sense also. Power steering plays a key role in steering feel by limiting the maximum amount of torque exerted by the driver. There are several ways in which this additional power can be supplied, such as with a hydraulic system or an electric one. In this thesis, hydraulic power steering has been modelled.

An engine-driven hydraulic pump delivers fluid to a servo valve operated through a direct mechanical linkage to the steering wheel (torsion bar). The valve is used to control the fluid and head it to a piston on the rack, which supplies the required steering assistance. A typical rotary valve is shown below:
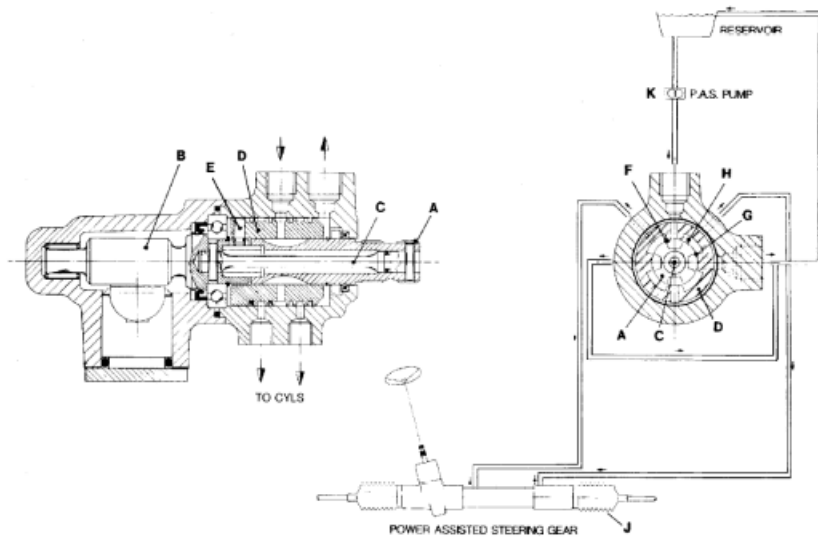
Figure 69 Power Assisted Steering System

The inner member (A) is controlled directly by the steering column, and it therefore faithfully follows steering wheel movements. This input valve member is connected to the pinion (B) by the torsion bar (C) which transmits torque between the two members. Fluid taken from a power steering pump (K) is supplied to this. A typical characteristic of the rotary valve is shown in the next figure, where the pressure is expressed as a function of the input torque (coming from the driver).
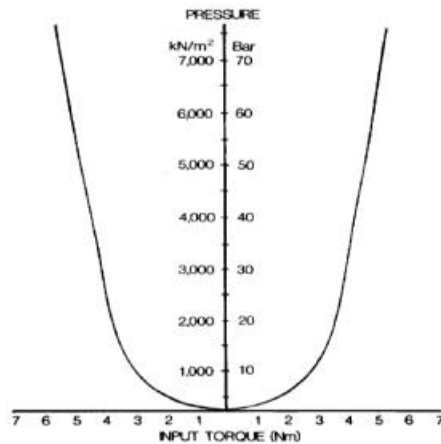
Figure 70 Input Steering Torque- Power Assisted System Pressure graph

Different vehicle types, different driving environments and different driving styles, etc. all tend to suggest that different 'feels' are required. For instance, a large vehicle that spends much of its "life" in town, at moderate speeds on straight roads can be satisfactorily steered with a system that uses large quantities of power and that only requires small forces from the driver to operate the valve. However, high-speed straight-line driving on highways or driving on twisting roads requires the accurate placing of the car and demands a system that 'tells' the driver much more about the car's response, enabling him to exercise the precise steering control that is necessary. At high speeds, the steering forces for corrections or lane changing manoeuvres are quite low and power assistance is not necessary. So, the characteristic curve is tuned in trying to find a compromise between these exigencies and for these reasons a typical characteristic between boost pressure and steering wheel torque has the trend shown in Figure 4.20:
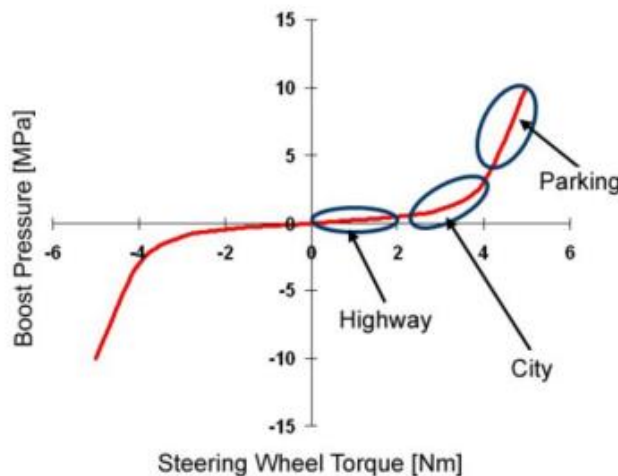
Figure 71 Boost Pressure - Steering Wheel Torque graph

In the "highway" interval the boost pressure is low and low power assist will be provided, making the steer more "direct". Vice versa in the "parking" interval, the boost pressure rises, and the assistance torque is provided since the main aim is to make the steering wheel as "soft" as possible, to reduce driver efforts. The following characteristic has been implemented in Dymola, starting from the data available in [11]. The relationship between boost pressure (or servo assistance pressure) and the steering wheel torque is given by a quadratic function, so:

$$P_{servo} = A \cdot T_{sw}^2 \cdot sign(T_{sw})$$

The servo assistance force is computed as:

$$F_{servo} = P_{servo} \cdot A_{servo}$$

A_{servo} is the area of the piston inside the double-acting hydraulic cylinder.

4.4 Tests

This section is meant to describe extreme drive conditions in which the steering wheel is hardly stressed so that we can understand which are the maximum forces and torques applied to it.

4.4.1 Overtaking Test (double lane change ISO 3888-2)

The report "An Assessment of Human Driver Steering Capability" by the National Highway Traffic Safety Administration of the US Department of Transportation [37], used double lane change data collected during NHTSA's Light Vehicle Handling and Electronic Stability Control (ESC) [38] Effectiveness Research Program to document the steering capability of human drivers in a highly transient situation.

A diverse range of test vehicles was used in this study, ranging from a high-performance sports car to a 15-passenger van. Each vehicle was equipped with an ESC.

Test Vehicle Descriptions.

Vehicle	Classification and Misc. Features	Wheelbase (inches)	Mean Track Width (in)	Test Weight (lbs)	Steering Ratio (deg/deg)	Left Steer Lock (deg)	Right Steer Lock (deg)
2003 Toyota Camry	High-volume passenger car, ESC, FWD, V6, 5-spd auto, 4-dr	107.0	60.8	3790	17.3	531	582
2002 Chevrolet Corvette	Sports car, ESC, RWD, V8, 5-spd manual, hatchback	104.3	61.6	3489*	16.0	487	489
2004 Volvo XC90 4x4	SUV, ESC, RSC, AWD, T5, 5-spd auto, 4-dr, 7-passenger capacity	112.3	64.2	5209	16.0	485	475
2003 Toyota 4Runner 4x4	SUV, ESC, AWD, V6, 5-spd auto, 4-dr, 5-passenger capacity	109.9	62.2	4668	17.3	564	549
2004 GMC Savana 3500	15-passenger van, ESC, RWD, V8, 5-spd auto	155.5	68.2	7075	17.1	599	574

To achieve the best compromise between high manoeuvre severity and reasonably low path variability, modified ISO 3888 Part 2 lane change geometry was used.
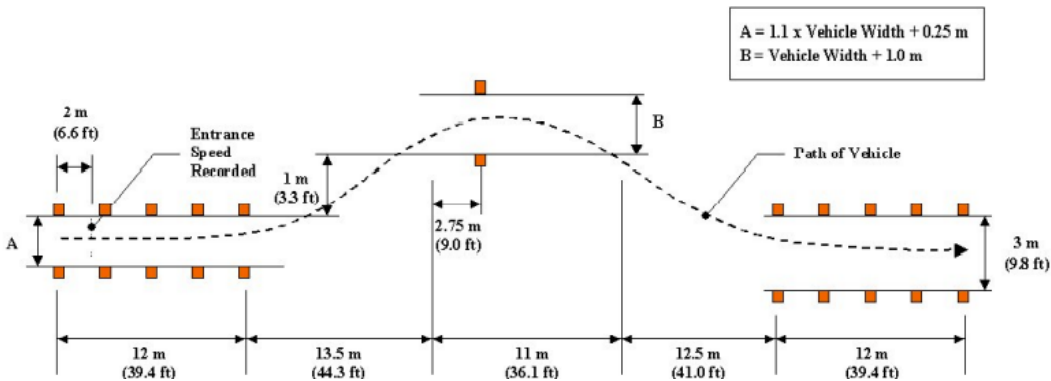

Figure 72 Modified ISO 3888-2 Course Layout

Three independent variables were considered: steering wheel angle (SWA), steering wheel rate (SWR), and steering wheel torque (SWT). The effect of three factors (driver, vehicle, and whether ESC was enabled or disabled), and one interaction term (vehicle and ESC) on these variables were investigated.

A summary of the overall maximum peak values recorded during tests is presented in the table below.

The data presented indicate drivers are capable of achieving very large steering inputs, even for relatively long periods of time. A maximum SWA of 578 degrees, and a maximum peak-to-peak SWA of 1118 degrees, were observed during an ESC enabled test performed with the Toyota 4Runner. A maximum, instantaneous peak SWR of 1819 deg/sec was recorded during an ESC disabled test performed with the Toyota Camry. Even when filtered with the most aggressive filter used in this study, the data indicate it is possible for the human driver to sustain an SWR of 963 deg/sec for one second, witnessed during an ESC disabled test performed with the Chevrolet Corvette. A maximum, instantaneous peak SWT of 33.9 lbf-ft (46.0 Nm) was observed during an enabled ESC test performed with the Volvo XC90. The ability of the driver to achieve high SWT was reduced greatly over time. In the extreme case where the driver is attempting to maintain the application of SWT for approximately one second, the largest peak SWT observed was 14.1 lbf-ft (19.1 Nm), 58.4 percent less than the maximum instantaneous peak value produced during the same test.

SWA (degrees)	Peak-to-Peak SWA (degrees)	SWR (degrees/s)	SWT (Nm)
578	1118	1819	46

Further details about the test are available in [37]

4.4.2 Kick-Plate Test

The "An instrumented steering wheel for driver model development" [39] reports the development and first employment of an Instrumented Steering Wheel (ISW) capable of sensing, at each hand, three forces and three torques, besides the grip force of both hands. The mass, moments of inertia and structural stiffness of the ISW are the ones of a common steering wheel.

Figure 73 Instrumented Steering Wheel (ISW)

Technical Specifications of the ISW. Parameters of a reference car steering wheel and parameters of the ISW.

Parameters	VALUE	Note
Mass	2.7 kg	Common car SW
Diameter	375 mm	Common car SW
Moment of inertia around rotation axis	<0.030 kg m^2	Common car SW
First natural frequency	50 Hz	Common car SW
Rated Force Capacity	±250 N	ISW
Rated Moment Capacity	± 25 Nm	ISW
Maximum force (applied without moment)	5×Maximum Rated Force Capacity	ISW
Maximum moment (applied without force)	5×Maximum Rated Moment Capacity	ISW

e first employment)]. The standard production spring clock cable provided power to the ISW and signal connection. The ISW data were acquired via a Kvaser USBcan Light system [41] and logged into a laptop with the steering angle data provided by the vehicle embedded sensor via CAN and the data provided by an OXTS RT3000 inertial and GPS system [42]. The tests were performed at the track "Pista e Centro Guida Sicura ACI-Sara Lainate "[43]. The track is equipped with a kick- plate. The kick-plate is a plank that is suddenly displaced in the lateral direction when the rear axle of a vehicle passes on it. This lateral excitation causes a yaw motion of the vehicle. Since the road surface that the vehicle traverses after the kick-plate is wet, the yawing motion amplitudes are relevant. To keep a straight path, the driver is required to counteract the yaw produced by the kick-plate. If the action of the driver is not quick, a spin may occur. The strong driver's action that is required implies quite different forces and moments exerted by the two hands on the ISW. Ten different drivers performed the kick-plate test nine times each, with two different speeds and two different kick gains (three times the low speed –low gain, three times the high speed –low gain, three times the low speed –high gain). The kick direction was random during all the tests. Two time-histories describing forces and moments are shown, one for the left hand and one for the right hand.
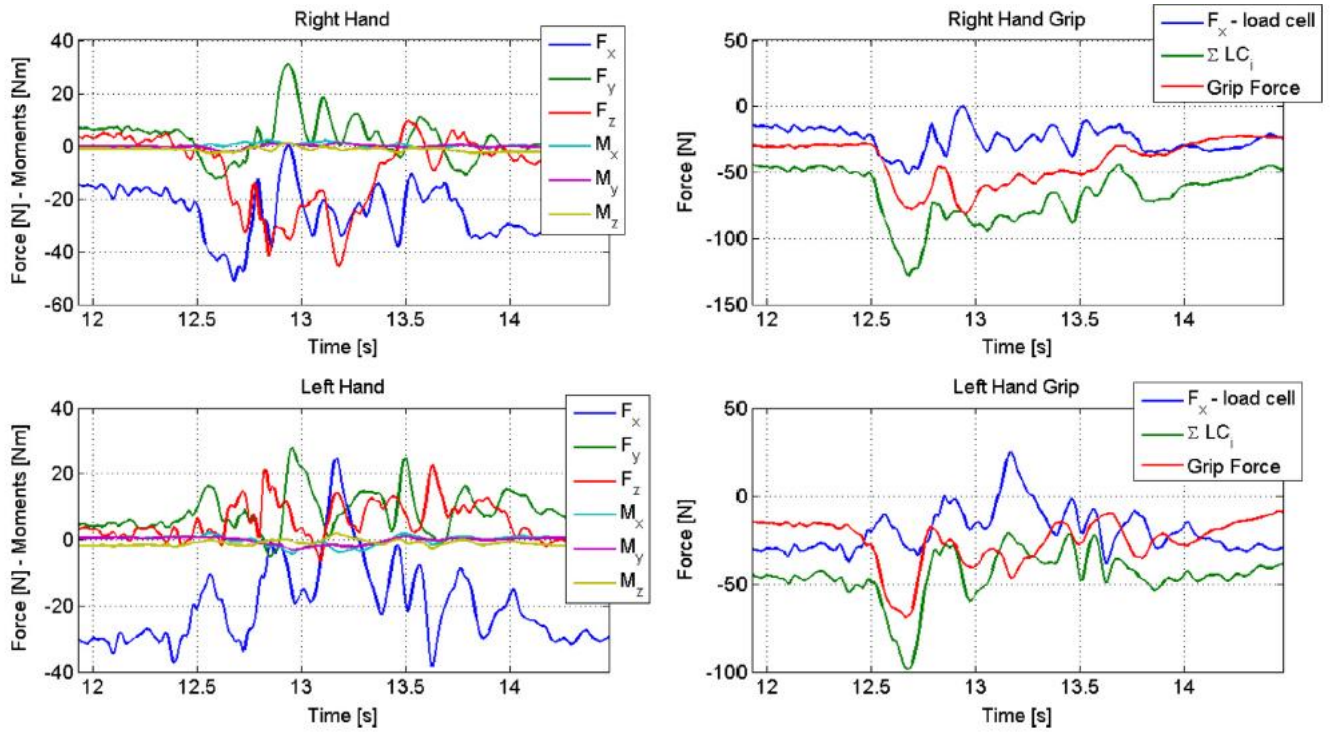
Figure 74 Kick-plate maneuver (input to the left). Forces and moments measured by the ISW at the two hand. LCi refers to i-th single axis load cell for grip detection

The reference systems are represented in the following figure.

Figure 75 ISW reference system

It is possible to note that the driver applies forces of less than 50 N during the emergency manoeuvre. The moments applied by the two hands are quite different from each other and are

lower than 5 nm. The grip forces at each handle are approximately in phase with the applied F_x and F_y.

A kick-plate manoeuvre towards the left is considered.
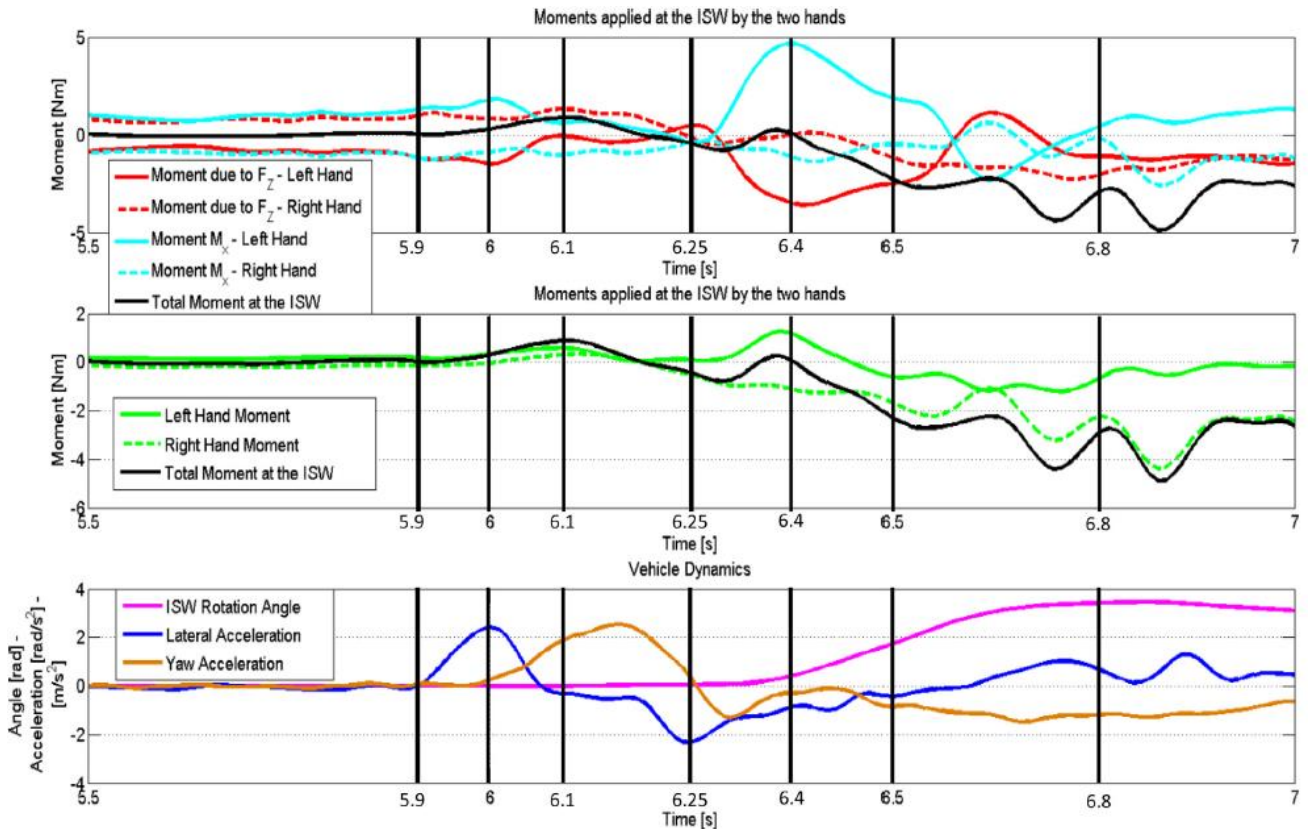
Figure 76 Kick-plate (input to left). Moments due to tangential forces and bare moments applied by hand during the initial phase of steering

moments on the ISW. This means that several NMS are activated in a coordinated manner. At t = 5.9 s the kick-plate starts its action. At t = 6 s the maximum lateral acceleration of the vehicle is reached. The ISW rotation angle is still zero. At t = 6.1 s a non-negligible moment is applied to the ISW, but the ISW rotation angle is still zero. Such a non-negligible moment seems counteracted by friction in the steering system, deliberately introduced to filter disturbances. The NMS is activated in reflex mode, due to the lateral kick that the driver's body and arms have received. The total non-negligible reflex moment is actually given by the two arms, wrists and hands, separately. At 6.25 s the voluntary steering action seems to initiate, but the ISW rotation angle is still zero. At 6.4 s the maximum bare moment by the left hand is applied, partially counteracted by the moment due to the tangential force F_z at the same left hand. The ISW starts rotating. At 6.8 s the rotation angle is fully developed. About 1 s has elapsed since the kick-plate has applied the lateral acceleration.

4.5 Passive Steering and Slalom/Active Steering Test

Method

Nineteen male subjects were divided into three groups of drivers with different driving levels, including skilled drivers, normal drivers and inexperienced drivers. Six subjects in the skilled driver group had held driving licenses for 8–25 years and they were professional vehicle testers. Their mean height was 172.2 cm (ranging from 165 to 177 cm), body weight 67.3 kg (61–90 kg) and age 34.3 (27–43). Seven subjects in the normal driver group had held driving licenses for 3–22 years and the average weekly driving distance amounted to 100–500 km. Their mean height was 167.3 cm (ranging from 160–180 cm), body weight 65 kg (55–84 kg) and age 32.3 (26–42). Six subjects in the inexperienced driver group had held driving licenses for 1–27 years. They were paper drivers or the average weekly driving distance was less than 100 km. Their mean height was 167.7 cm (ranging from 161 to 175 cm), body weight 66.3 kg (58–83 cm) and age 33 (25–49).

Procedure

Two experiments were performed for each subject. In each experiment, the subject was seated in the driver seat, and held the steering wheel with the right hand at the 3 o'clock position as the neutral or basic posture in a driving simulator (Figure 1), the same as the driving posture but without fastening the seat belt.

Figure 77 Subject in the basic posture sitting in the driving simulator and grasping the steering wheel with right hand at 3 o'clock position

The left hand was released from the steering wheel in the experiments. The seat and steering wheel were adjusted so that the arm was slightly bent at the elbow (approximately 110 deg between the forearm and upper arm) and the line along the steering axis (steering column) was approximately parallel to the line through the shoulder and wrist joints in the basic posture. The basic posture came from lots of investigations in which most of the subjects in the present investigation would feel comfortable in this posture. The basic posture approximately conformed to their driving customs.

4.5.1 Passive Steering Task

The subject was instructed to stabilize the steering wheel in its neutral position under the disturbed torque produced by a motor. The magnitude and frequency of the disturbed torque were defined as 5 Nm and 0.025 Hz (Figure 2), respectively. The magnitude was determined by referring to the value of torque in the actual driving condition with a conventional power-assisted steering system. The frequency was determined in a quasi-stable range in order to detect distinct and useful results. The subject continuously stabilized the steering wheel (keeping it in its neutral position) for at least one circle, including 3 varying torque periods.
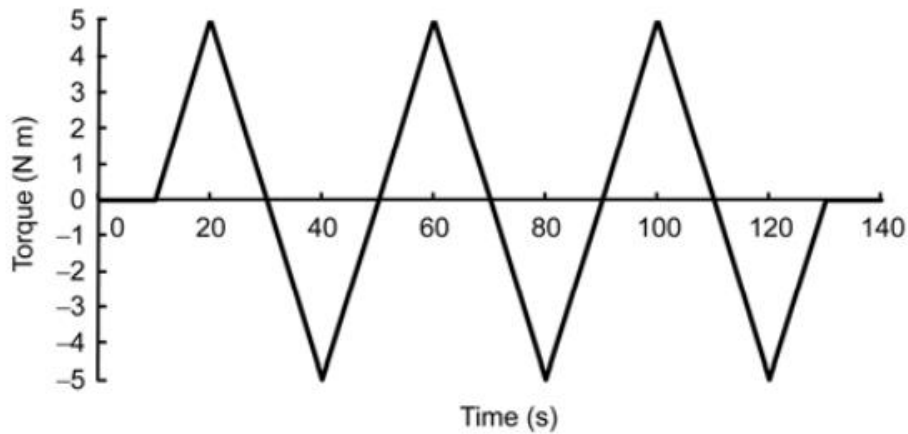
Figure 78 The disturbed torque produced by a motor in the driving simulator. One cycle consists of 3 periods of varying torque

4.5.2 Active Steering Task

The subject was instructed to perform a sine steering like the slalom steering test (Figure 3). The magnitude and frequency of this sine steering were approximately 60 deg (while steering torque was about 5 Nm) and 0.25 Hz respectively, which were similar to the slalom steering test of the vehicle under the velocity of 60 km/h.

Figure 79 The active steering task. One circle consists of 3 periods of sine steering at least

5 Steering Wheel Development

Next, will be illustrated two solutions for the connection of the steering wheel to the motor, an own adapter design, using mainly commercial mechanical components.

5.1 Proposed Design
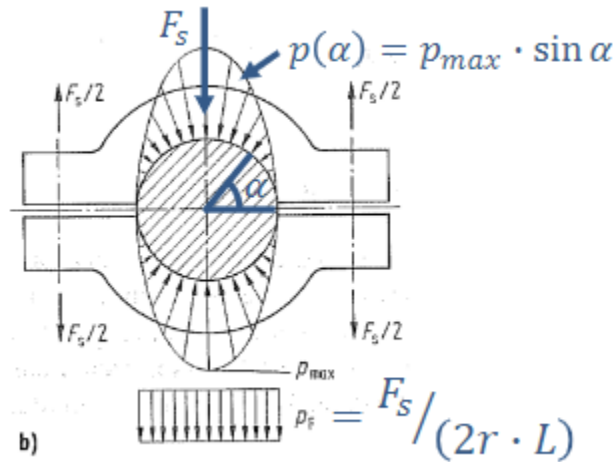
Figure 80 Adapter Proposed Design

From a forces balance along the vertical direction for a single side, we obtain:
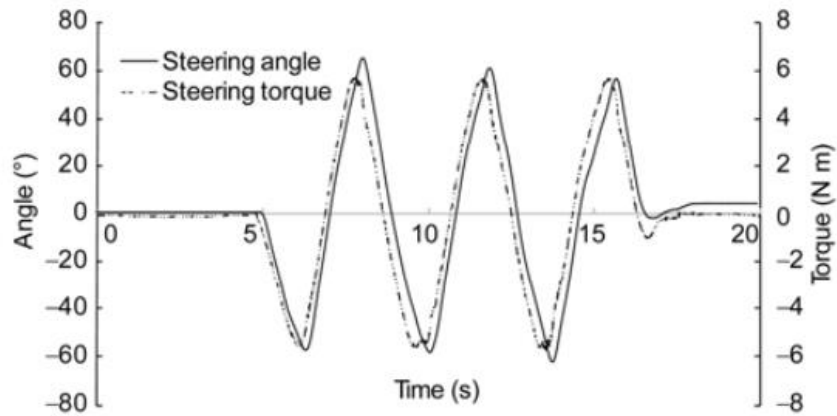
$$F_S = \int_0^\pi p(\alpha) \cdot L \cdot r \cdot d\alpha \cdot \sin \alpha \ = p_{MAX} \cdot L \cdot r \int_0^\pi \sin^2 \alpha \ d\alpha = \frac{\pi}{2} \cdot p_{MAX} \cdot L \cdot r$$

$$p_{MAX} = \frac{2F_s}{\pi L r}$$

The **infinitesimal** contribution of transmissible torque from half fit is:

$$dT_t = r \cdot dF_{friction} = \tau_{friction} \cdot L \cdot r^2 \cdot d\alpha = \mu \cdot p_{MAX} \cdot \sin \alpha \ \cdot L \cdot r^2 \cdot d\alpha$$

Integrating for both sides we obtain the expression of the total transmissible torque:

$$T_t = 2 \cdot \int_0^\pi dT_t = 4r^2 \cdot \mu \cdot L \cdot p_{MAX} = \frac{8}{\pi} \mu r F_s \quad \xrightarrow{\ p_F = \frac{F_s}{2r \cdot L}\ } \quad = \frac{16}{\pi} r^2 L \mu p_F$$

Since the transmissible torque must be equal to or greater than the maximum steering torque

$$T_t \geq T_{x_{max}} = \ 46 \ Nm = 46000 \ Nmm$$

Elaborating the total transmissible torque expression we find that the screw axial must be greater than $F_{S_{min}}$.

$$F_S \geq F_{S_{min}} = \frac{\pi \cdot T_{x_{max}}}{8\mu r}$$

Considering both hub and shaft are made of steel with rectified surfaces and not lubricated, the friction coefficient μ will approximately be equal to 0.2. In addition, the internal diameter is known as it's equal to the motor shaft diameter (24 mm).

$$F_{S_{min}} = \frac{\pi \cdot T_{x_{max}}}{8\mu r} = \frac{\pi \cdot 46000}{8 \cdot 0.2 \cdot \frac{24}{2}} = 2468 \ N$$

Thus:

$$p_{MAX_{min}} = \frac{2F_{S_{min}}}{\pi L r} = 6,55 MPa$$

For the chosen parameters, the parameters are:

$$F_{S_{chosen}} = 2500 N$$

$$p_{MAX_{chosen}} = \frac{2F_{S_{min}}}{\pi L r} = 6,63 \ MPa$$

5.2 Material

The component will be considered made of Aluminum EN 573-AW AlCu6BiPb (or 2011, UNI 9002/5), physical state T8.[46]

Process Characteristics:

Anodizing   DISCREET

Machinability   EXCELLENT

Corrosion resistance DISCREET

Mechanical Characteristics:

$R_s = 315 \ MPa = $ Yield Strength

$R_m = 395 MPa = Ultimate \ Tensile \ Strength$

Physic Characteristics:

$E = Young's\ Modulus = 70\ 000\ MPa$

$Poisson's\ Coefficient = 0.33$

Density = 2.82 g/cm^3

5.3 Forces and Torques Balance

x) $\vec{T}_x = \frac{d_{wheel}}{2}\vec{F}_{z_l} + \frac{d_{wheel}}{2}\vec{F}_{z_r}$ y) $\vec{T}_y = 0$ z) $\vec{T}_z = \frac{d_{wheel}}{2}\vec{F}_{x_l} - \frac{d_{wheel}}{2}\vec{F}_{x_r}$

$\vec{F}_x = \vec{F}_{x_l} + \vec{F}_{x_r}$ $\vec{F}_y = \vec{F}_{y_l} - \vec{F}_{y_r}$ $\vec{F}_z = \vec{F}_{z_l} - \vec{F}_{z_r} - m_{wheel}g\sin\alpha$
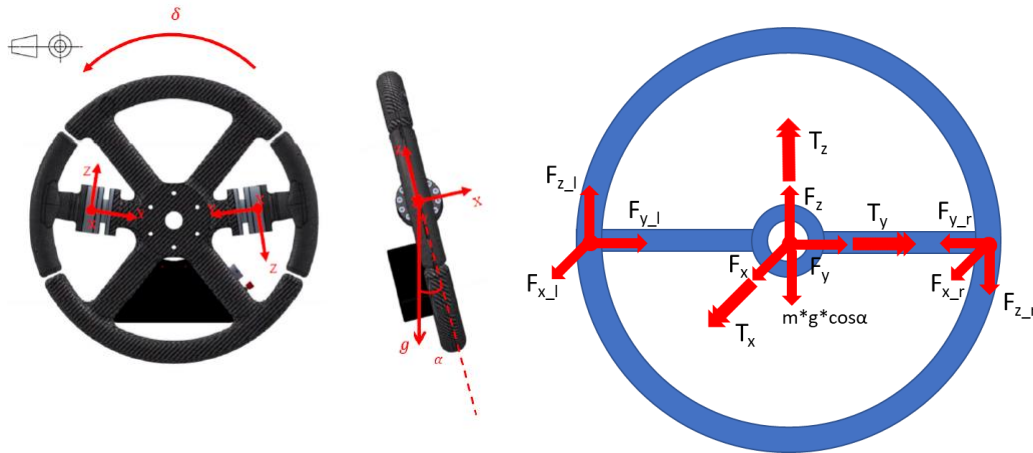
On Wheel

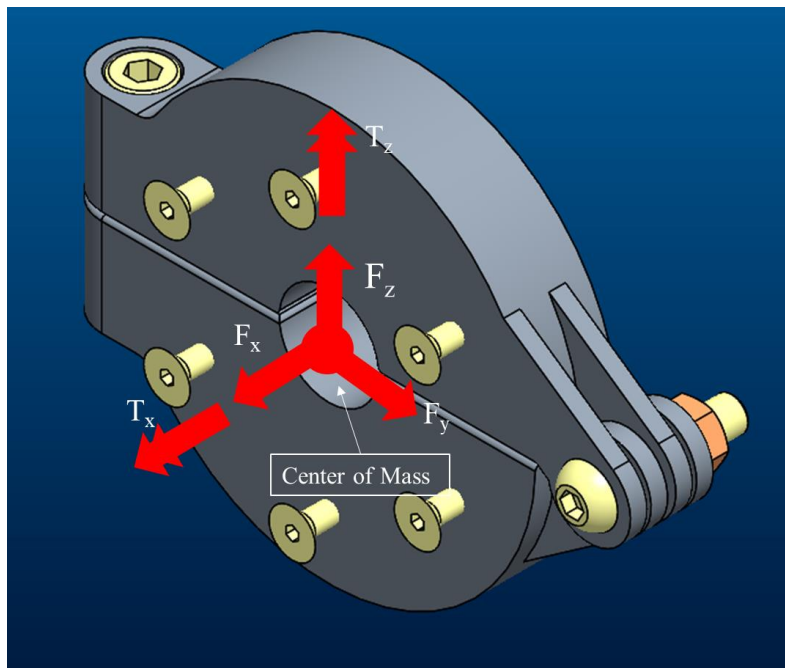Figure 81 Forces and Torques applied on Steering Wheel

On Adapter

Figure 82 Forces and Torques applied on Adapter

Note: The torque increase owing to the multiplication of the Fx, Fy,Fz by the handwheel depth and adapter depth (lengths along the z-axis) are negligible.

5.4 Cylindrical Body Design and Analysis

As a first approximation, we can consider the coupling as two coaxial cylindrical bodies applying a pressure load to each other and transmitting a given system of forces and torques.

5.4.1 Stress State

The total stress distribution on the hub and shaft derives from the overlapping of a pressure load and forces/torques transmitted through the coupling.

5.4.1.1 Pressure Load

The equations that provide the information about stress distribution due to a pressure load on a cylindrical body are known as Lamé's formulas. These expressions refer to a short, but radially thick cylinder. In its simplified form, the expressions consider only the pressure.

$$\sigma_c = A + \frac{B}{r^2} = circunferential\ stress$$

$$\sigma_r = A - \frac{B}{r^2} = radial\ stress$$

The axial stress σ_a is negligible.

Figure 83 Mathematical model for internal pressure applied on a hollow cylindrical body
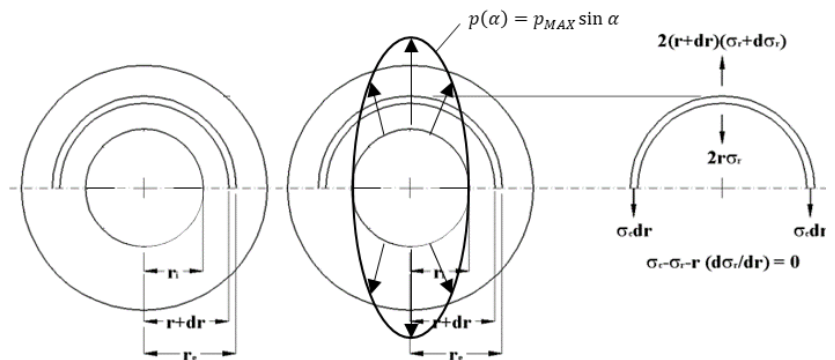
Initial conditions on the **Hub** are:

$$\sigma_r\left(r = r_{hub_i} = d/2\right) = -p(\alpha)$$

$$\sigma_r\left(r = r_{hub_e}\right) = 0$$

Solving the equations for the **Hub**, we obtain:

$$\sigma_c(r, \alpha) = \frac{p(\alpha)}{a^2 - 1}\left(1 + \frac{r_{hub_e}^{\ 2}}{r^2}\right)$$

$$\sigma_r(r, \alpha) = \frac{p(\alpha)}{a^2 - 1}\left(1 - \frac{r_{hub_e}^{\ 2}}{r^2}\right)$$

Where $a = {}^{r_{hub_e}}/_{r_{hub_i}} = {}^{d_{hub_e}}/_d$

For $\sin \alpha = 1$ and $r = r_{hub_i} = \frac{d}{2}$ we obtain the maximum values of σ_c and σ_r for the **Hub**.

$$\sigma_{c_{max}} = p_{MAX} \frac{a^2 + 1}{a^2 - 1}$$

$$\sigma_{r_{max}} = -p_{MAX}$$
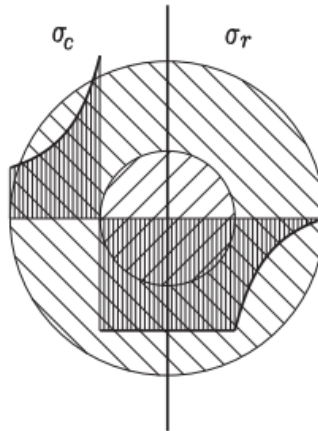
Figure 84 Stress distribution for uniform internal pressure

5.4.1.2 Concentrate Forces

F_{radial} arises when summing F_y and F_z . F_{radial} generates shear stress on the hub and shaft.

Shear stress is distributed along a hollow circular surface (**Hub surface**) in the following way:
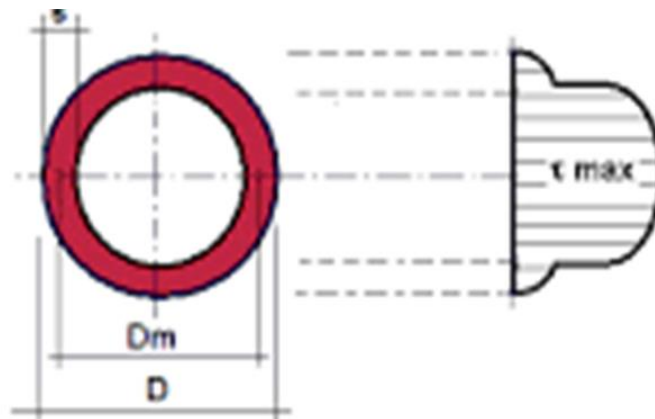

Figure 85 Shear stress distribution on a hollow cylindrical section due to F_radial

Its maximum value can be calculated as:

$$\tau_{radial} = \frac{2F}{A} = \frac{8F_{radial}}{\pi(d_{external}^2 - d_{internal}^2)}$$

$$F_{radial} = \sqrt{F_y^2 + F_z^2}$$

On the other hand, F_x generates axial stress with a constant profile.

Its maximum value on a hollow circular section is (**Hub section**):

$$\sigma_{F_x} = \frac{F_x}{A} = \frac{4F_x}{\pi(d_{hub_e}^2 - d^2)}$$

5.4.1.3 Concentrate Torques

The stress distribution due to T_z is $\sigma_{T_z} = \frac{T_z\, y}{J}$

For hollow circular section $J = \frac{\pi}{64}(d_{external}^4 - d_{internal}^4)$

So, in the study case:

For the Hub: $\sigma_{T_z} = \frac{32 T_z d_{hub_e}}{\pi(d_{hub_e}^4 - d^4)}$

Figure 86 Hollow Section

The maximum stress value due to the torque T_x applied to a cylindrical beam section is:

$$\tau_{T_x} = \frac{T_x \cdot R}{J_p}$$

J_p is the polar moment of the section and R is its radius.

For hollow circular section, $J_p = \frac{\pi}{32}(d_{external}^4 - d_{internal}^4)$

So, in the study case :

For the Hub: $\tau_{T_x} = \frac{16 T_x d_{hub_e}}{\pi(d_{hub_e}^4 - d^4)}$
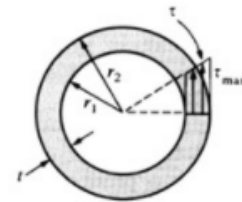
5.4.2 Statical Analysis

Applied Forces

According to The Measure of Man and Woman [1], on handwheels for vehicles, valves or tools, the optimum ergonomic rim force required is 13 to 22N. The maximum rim force is 89N with

one hand and 133 N with two hands. The wheel's diameter should be between 178mm and 533mm.

These values are compatible with the maximum steering torque equal to 46 Nm found during the "Overtaking Test", carried out with a Volvo XC90 (steering wheel diameter $=d_{wheel}=$ 350 mm).

$$T_{x_{max}} = 46\ Nm$$

Indeed, given d_wheel=300mm=0,30m and considering $F_{zr\_max} = F_{zl\_max}$:

$$F_{zr\_max} = F_{zl\_max} = F_{z_{max}} = \frac{T_{x_{max}}}{d_{wheel}} \approx 153N$$

On the other hand, the Kick-plate Test provides us with peak values of forces applied on the wheel handle along axis x,y during an emergency situation.

$$F_{x_l}, F_{x_r}, F_{y_l}, F_{y_r} \leq 50\ N$$

Let's consider the most critical (and not repetitively) situation could occur when driving, that is, when two forces in the same direction reach the peak at the same time (two peaks overlapped) generating traction and/or shear stresses on the part.

Then, $F_{y_{max}} = F_{y_l} - F_{y_r} = 50 - (-50) = 100N$ and $F_{x_{max}} = F_{x_l} + F_{x_r} = 50 + 50 = 100N$.

Remind:

$$F_{S_{chosen}} = 2500N$$

$$p_{MAX_{chosen}} = \frac{2F_{S_{min}}}{\pi L r} = 6,63\ MPa$$

Verification

The analysis of the overall stress distribution makes it possible to identify as critical points, the points located at the hub internal diameter (d) at $\alpha = 90°, 270°$. These points are the points where pressure load reaches its peak. As we are approximating the hub to a cylinder with a solid homogenous hollow section and negligible depth, the critical section can be anyone.

|				Forces		Hub Stresses			% with respect to sigma_c	
		Geometry								
	d	24	mm	Fymax=Fxmax	100 N	sigma_c	7,65	Mpa	100%	
hypotesis	d_hub_e	90	mm	Fzmax	153 N	sigma_r	-6,63	Mpa	87%	
	L	20	mm	F_radial	179 N	tau_Fradia	6,06E-02	Mpa	1%	neligible
results	m_hub	0,5	kg	Tx	46000 Nmm	sigma_Fx	1,69E-02	Mpa	0%	neligible
	μ	0,61		Tz	15000 Nmm	tau_Tx	0,09	Mpa	1%	neligible
greatest stress	a	3,75		Fs_min	2468 N	sigma_Tz	0,21	Mpa	3%	neligible
	d_wheel	300	mm	pmax_min	6,55 MPa	sigma_vm	12	Mpa		
				Fs_chosen	2500 N					
				pmax_chosen	6,63 MPa					
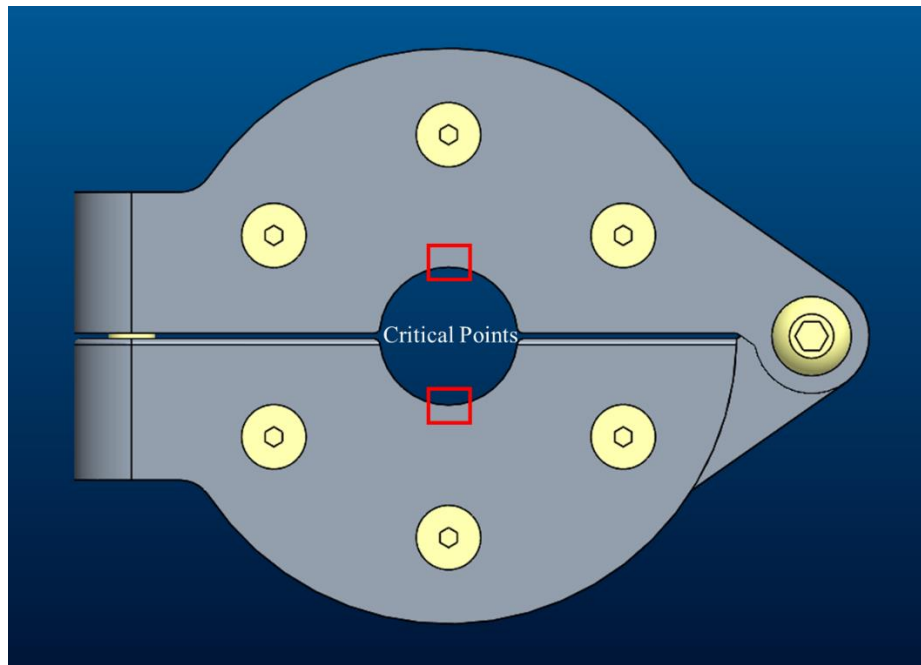
Figure 87 Critical Points

On these points, the stress state's main components are radial and circumferential stresses caused by the contact pressure. Every other stress is negligible.
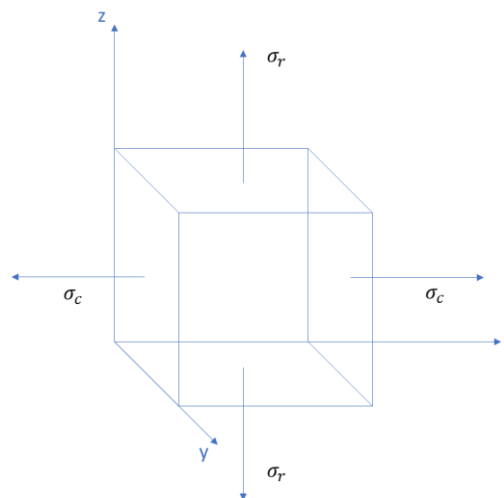

Figure 88 Stress State on the critical points

Considering

$$\sigma_c = \sigma_{c_{max}} = p_{MAX} \frac{a^2 + 1}{a^2 - 1}$$

$$\sigma_r = \sigma_{r_{max}} = -p_{MAX}$$

By applying Von Mises' yield criterion, we obtain:

$$\sigma_{VM} = \sqrt{\sigma_c^2 + \sigma_r^2 - \sigma_c \sigma_r} = 12 MPa \ll R_s$$

Therefore, the component is statically verified ($\sigma_{VM} \ll R_s$).

5.4.3 Dynamic Analysis

In this section we will study the components from the dynamic point of view. The steering wheel inputs illustrated in "Kick-Plate Test" (forces) and "Passive Steering and Slalom/Active Steering Test" (steering torque) will be considered.

Applied Forces

By analyzing the graphs in the Section "Kick-Plate Test" we can define the following:

$$F_{x_{max}} = 0 \, N, F_{x_{min}} = -100 \, N$$

$$F_{y_{max}} = 20 \, N, F_{y_{min}} = 0 \, N$$

$$F_{z_{max}} = 25 \, N, F_{z_{min}} = -50 \, N$$

And "Passive Steering and Slalom/Active Steering Test"

$$T_{x_{max}} = 6 \, Nm, T_{x_{min}} = 6 \, Nm$$

In this analysis, just torsional and bending effects of forces will be taken into account. In addition, F_s and p_{MAX} are constant and have the same value considered on the static analysis.

To dynamically verify a mechanical component, we should first identify stress state alternate and average components.

$$\sigma_a = \frac{\sigma_{max} - \sigma_{min}}{2} \quad and \quad \sigma_m = \frac{\sigma_{max} + \sigma_{min}}{2}$$

$$\tau_a = \frac{\tau_{max} - \tau_{min}}{2} \quad and \quad \sigma_m = \frac{\tau_{max} + \tau_{min}}{2}$$

Then compute from Haigh diagram bending fatigue limit $\sigma_{a_{lim}}$:
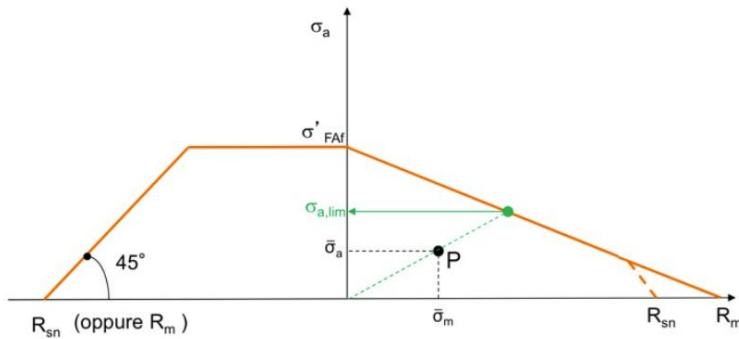
$$\sigma'_{FA} = \sigma_{FA} \cdot \frac{b_2 \cdot b_3}{K_{f,f}}$$

Figure 89 Haigh Diagram

And the torsional fatigue limit $\tau_{a_{lim}}$:
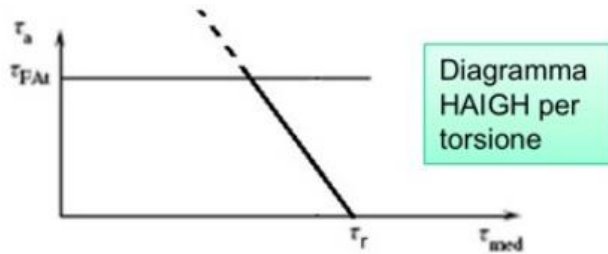
$$\tau'_{FA} = \tau_{FA} \cdot \frac{b_2 \cdot b_3}{K_{f,t}}$$

Figure 90 Haigh Diagram for torsion

Where:

$b_2 = dimensional\ factor$

$$b_2 = \frac{\sigma'_{FA}}{\sigma_{FA}}$$
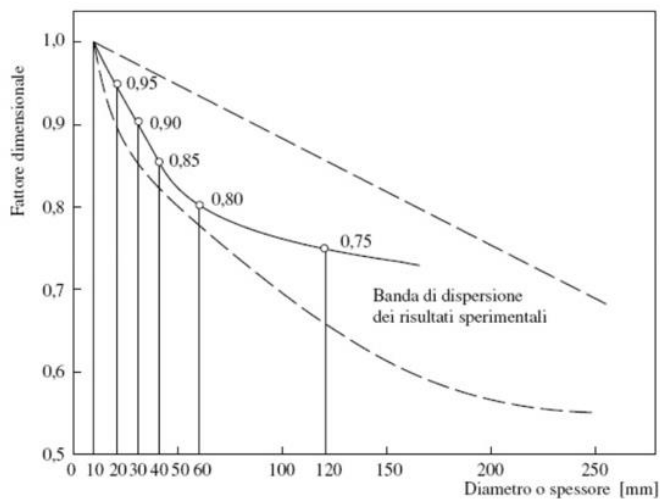
Figure 91 Dimensional Factor

$b_3 = superficial\ factor$

82

$$b_3 = \frac{\sigma'_{FA}(R_t)}{\sigma_{FA}}$$

Figure 92 Superficial Factor

$K_f = fatigue\ notch\ factor$

$$K_f = 1 + q(K_t - 1)$$

$q = fatigue\ sensitivity$

Figure 93 Fatigue sensitivity

Then we have to compute Gough-Pollard equivalent stress σ_{GP}

$$\sigma^*_{GP} = \sqrt{\sigma_a^2 + \left(\frac{\sigma_{lim}}{\tau_{lim}}\right)^2 \cdot \tau_a^2} \leq \sigma_{lim}$$

Verification

As mentioned, only torsional and bending stresses are considered according to the Gough-Pollard method.

$$\sigma_{T_z} = \frac{32 T_z d_{hub_e}}{\pi \left(d_{hub_e}^4 - d^4\right)}$$

$$\tau_{T_x} = \frac{16 T_x d_{hub_e}}{\pi \left(d_{hub_e}^4 - d^4\right)}$$

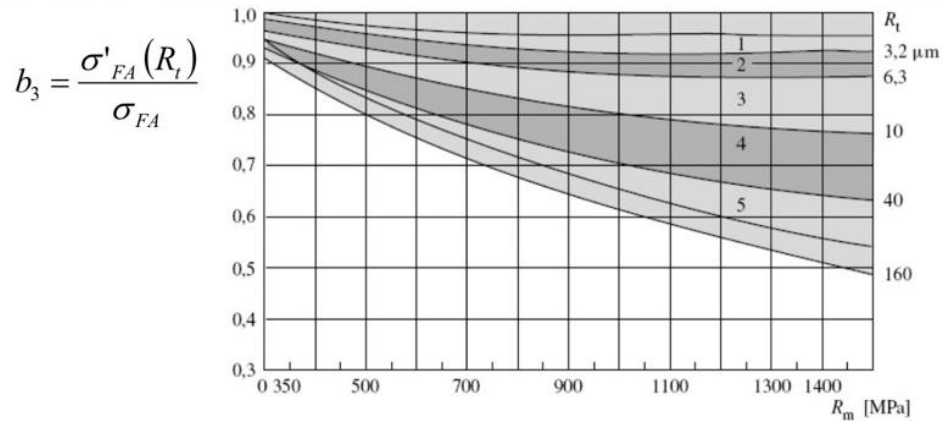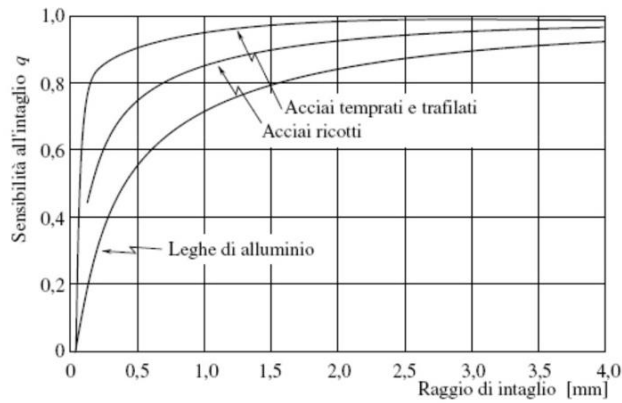From Haigh Diagram we find fatigue limits $\sigma_{a_{lim}}$ and $\tau_{a_{lim}}$:

$$\begin{cases} \sigma_a = -\dfrac{\sigma'_{FAf}}{R_m} \sigma_m + \sigma'_{FAf} \\ \sigma_a = \dfrac{\sigma_{T_{z\_a}}}{\sigma_{T_{z\_m}}} \sigma_m \end{cases} \rightarrow \sigma_{a_{lim}}$$

$$\tau_{a_{lim}} = \tau'_{FAf}$$

Follow the entire computation:

				HUB								
		Geometry			Forces Min and Max value					Hub Stresses		
		d	24 mm		Fxmax	0 N	Fxmin	-100 N	tau_Tx_max	0,01 MPa	tau_Tx_min	-0,01 MPa
	hypotesis	d_hub_e	90 mm		Fymax	20 N	Fymin	0 N	sigma_Tz_max	0,00 MPa	sigma_Tz_min	-0,21 MPa
		m_hub	0,5 kg		Fzmax	25 N	Fzmin	-50 N				
	results	L	20 mm		Tz_max	0 Nmm	Tz_min	-15000 Nmm	tau_Tx_a	0,01 MPa	tau_Tx_m	0,00 MPa
		μ	0,61		Tx_max	3750 Nmm	Tx_min	-7500 Nmm	sigma_Tz_a	0,11 MPa	sigma_Tz_m	-0,11 MPa
	greatest stress	d_wheel	300 mm									
		Rm	395 Mpa									
		tau_m	228 Mpa									
		Fatigue Factors			Pure Alternate Fatigue Limits			Equivalent Fatigue Limits				
		b2	0,85		sigma'FA	111 MPa		sigma_lim	155 MPa			
		b3	0,9		tau'FA	67 MPa		tau_lim	67 MPa			
		q	0,9									
		Kt	1,4					Gough-Pollard Equivalent Stress				
		Kf	1,36					sigma_GP	0,11 MPa			

The Hub is dynamically verified since $\sigma_{GP} \ll \sigma_{a_{lim}}$

5.5 Adapter Lateral Flange

The adapter lateral flanges can be approximated to a plate with a vertical force applied on an end and the opposite end is fixed. It works only statically.
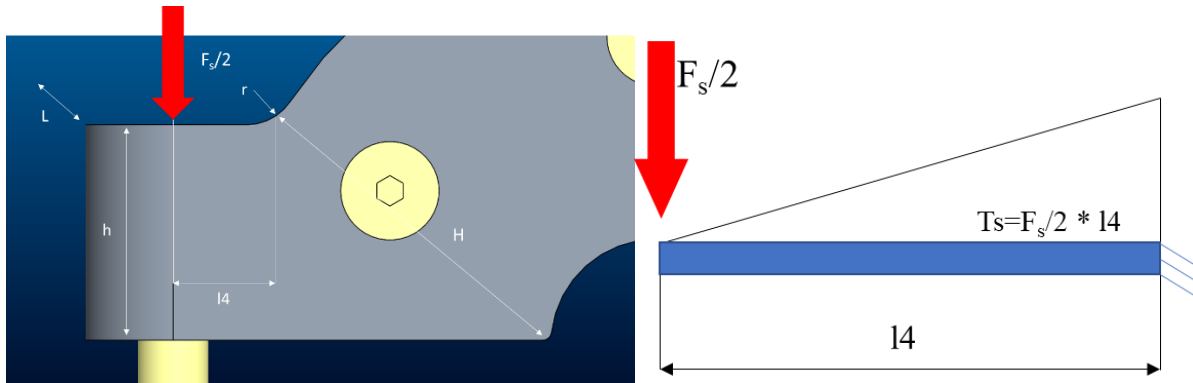
Figure 94 Lateral flanges applied forces

Stress State and Static Analysis

The stress state is only composed of the maximum axial stress value given by $Ts = \frac{F_s}{2} l_4$ (bending torque) since the shear stress generated by Fs/2 is negligible.

$$\sigma_{T_s\_Nom} = \frac{6T_s}{Lh^2}$$

Given the geometrical dimensions we can find Kt on the graph:
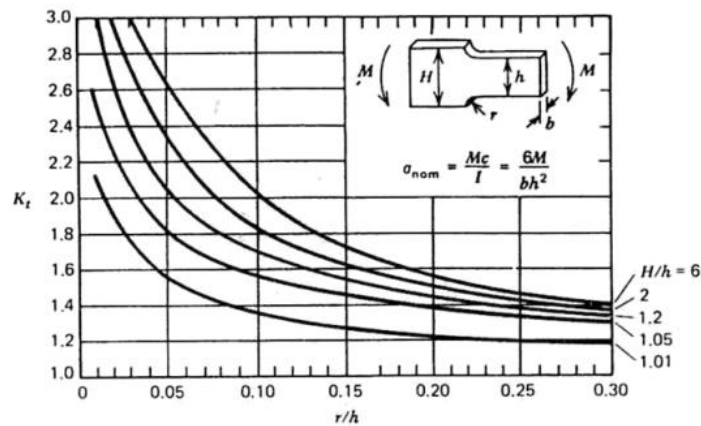
Figure 95 Kt grapgh

And finally, compute the maximum stress value:

FLANGE							
At the round	I4	24 mm		tau_Fs	3 MPa	negligible
	L	20 mm		sigma_nom	16 MPa	
	h	24 mm		H/h	1,667	
	H	40 mm		r/h	0,250	
	r	6 mm		Kt	1,4	
	Fs_chosen/2	1250 N		sigma_max	22 MPa	
	Ts	30000 Nmm				
At the bore	L	20 mm		tau_Fs	4 Mpa	negligible
	h	24 mm				
	d	6 mm				
	Fs_chosen/2	1250 N				

So $\sigma_{T_s\_Max} = 100 \; MPa \leq R_s$.

5.6 Screws

The force applied to the screws is the following:

$F_s = 2500 \; N$ and $V = \dfrac{T_{xmax}}{r_{screw\_axis}} = \dfrac{46000 \; Nmm}{35mm} = 219 \; N$ plus the Total Tightening Torque

$T_a = T_k + T_{ga} = F_s[\mu \dfrac{1.5D}{2} + tg(\varphi + \rho') \dfrac{d_2}{2}].$

Figure 96 Forces applied on the screws

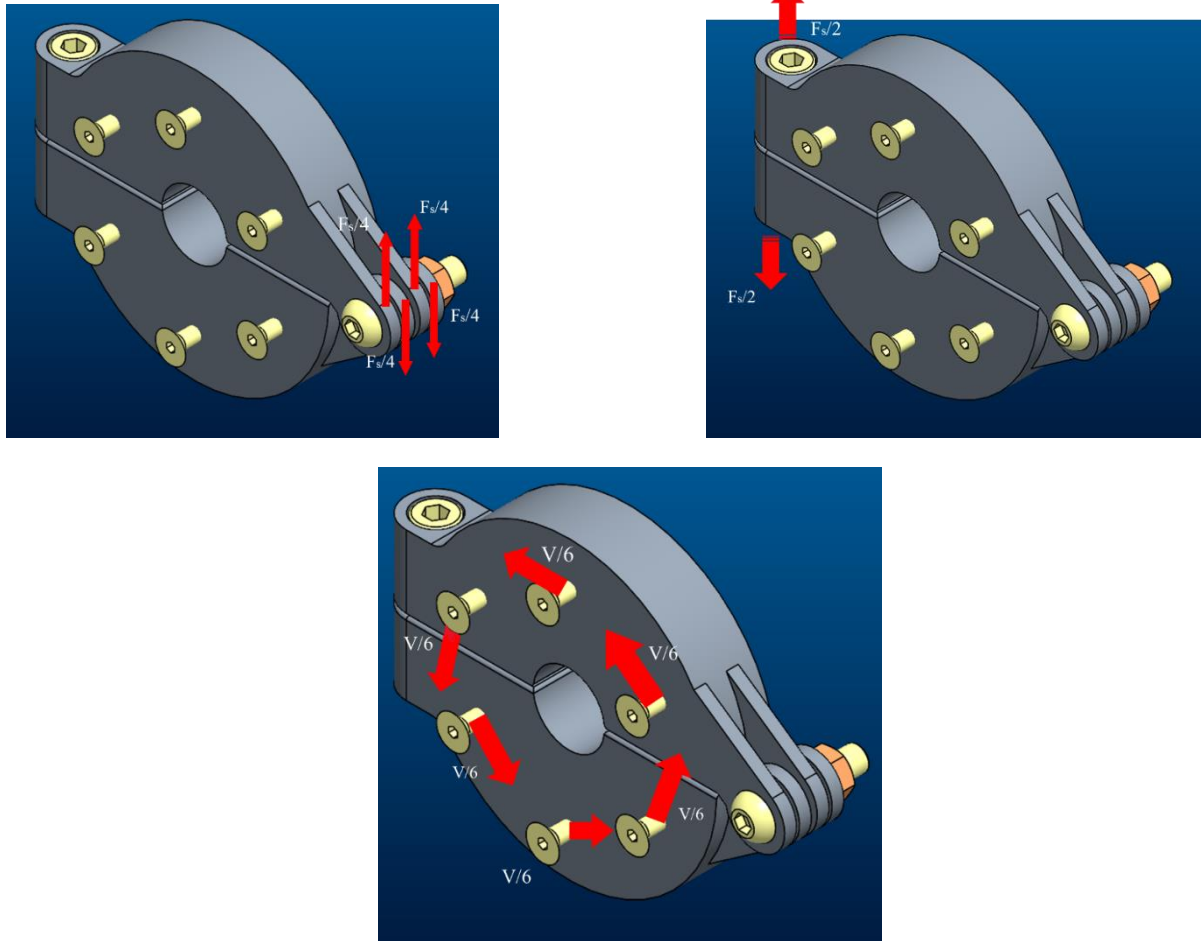On the following computation d3 (screw minor diameter) is considered to compute the resistant area of the screw:

		Adapter-Adapter Screws								Adapter-Handwheel Screws				
	Fs	2500	N		class	10,9			Tx	46000	Nmm		class	8,8
	M8				Rs	900	Mpa		r	35	mm		Rs	640	Mpa
major diam.	D	8	mm		Rm	1000	Mpa		n	6	screws		Rm	800	Mpa
pitch diam.	d2	7,188	mm						V_required	219	N			
minor diam.	d3	6,466	mm						Fs	100	N			
	A3	8,20921	mm2						M5					
pitch	p	1,25	mm					major diam.	D	5	mm			
helix angle	φ	0,04969	rad					pitch diam.	d2	4,48	mm			
thread angle	α	1,0472	rad					minor diam.	d3	4,019	mm			
friction coeff.	μ	0,47							A3	3,17151	mm2			
friction angle	ρ	0,49723						pitch	p	0,8	mm			
effective tightening	Tga	5471	Nmm					helix angle	φ	0,05089	rad			
total tightening	Ta	12521	Nmm					thread angle	α	1,0472	rad			
								friction coeff.	μ	0,47				
Applied forces are:								friction angle	ρ	0,49723				
	Fs	2500	N					effective tightening	Tga	137	Nmm			
	Tga	5471	Nmm					total tightening	Ta	313	Nmm			
Stresses:								Applied forces are:						
	σ_Fs	304,5	Mpa						Fs	100	N			
	τ_Tga	103,1	Mpa						Tga	137	Nmm			
	σ_vm	353,001	Mpa	Chosen Screws:					V_required	219	N			
Safe factor	Sf	2,55		M8-class 10,9				Stresses:						
									σ_Fs	24,9	Mpa			
									τ_Tga	10,7	Mpa			
									τ_V	69,1	Mpa			
									σ_vm	140	Mpa	Chosen Screws:		
								Safe factor	Sf	4,56		M5-class 8,8		

Motor Flange - Support

Tx	46000	Nmm	class	5,6	
r	25	mm	Rs	300	Mpa
n	4	screws	Rm	500	Mpa
V_required	460	N			
Fs	50	N			
M8					
major diam.	D	8	mm		
pitch diam.	d2	7,188	mm		
minor diam.	d3	6,466	mm		
	A3	8,20921	mm2		
pitch	p	1,25	mm		
helix angle	ϕ	0,04969	rad		
thread angle	α	1,0472	rad		
friction coeff.	μ	0,47			
friction angle	ρ	0,49723			
effective tightening	Tga	109	Nmm		
total tightening	Ta	250	Nmm		
Applied forces are:					
	Fs	50	N		
	Tga	109	Nmm		
	V_required	460	N		
Stresses:					
	σ_{Fs}	7,7	Mpa		
	τ_{Tga}	2,1	Mpa		
	τ_{V}	56,0	Mpa		
	σ_{vm}	101	Mpa	Chosen Screws:	
Safe factor	Sf	4,95	M8x1,25-class 5,6		

Adapter Fixture Screws

	Fs	1250	N	class	12,9
	M8			Rs	1080 Mpa
major diam.	D	8	mm	Rm	1200 Mpa
pitch diam.	d2	7,188	mm	τsn	624 Mpa
minor diam.	d3	6,466	mm		
	A3	8,20921	mm2		
	τ_{Fs}	152			
				Chosen Screws:	
Safe factor	Sf	4,10	M8-class 12,9		

Adapter-Adapter Screw
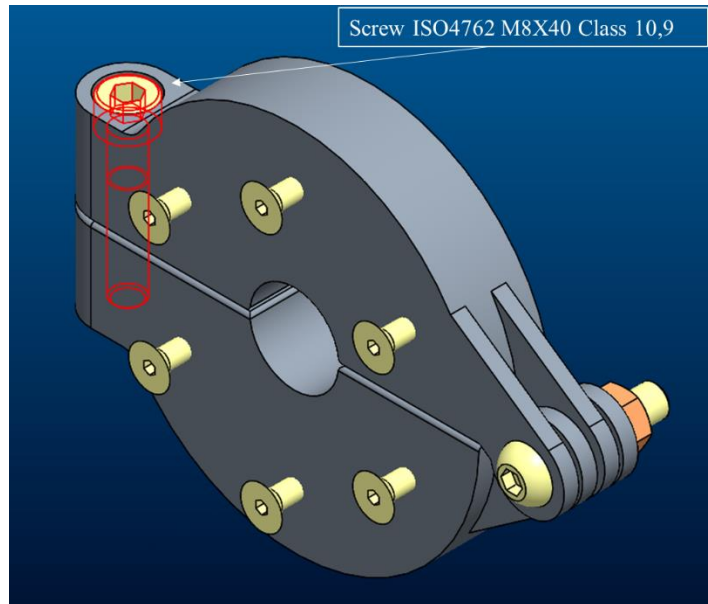

Screw ISO4762 M8X40 Class 10,9

Figure 97 Adapter-Adapter Screw

Adapter-Handwheel Screws

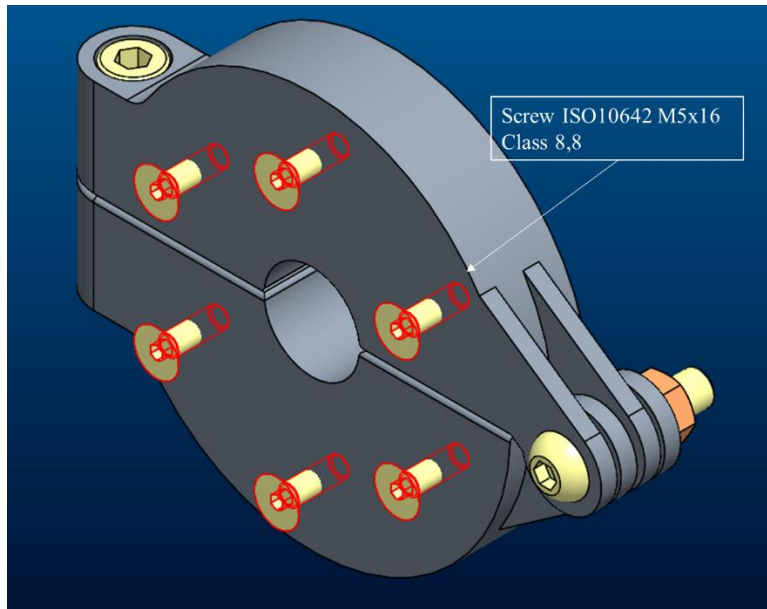**Figure 98 Adapter-Handwheel Screws**

Adapter Fixture Screw and Nut

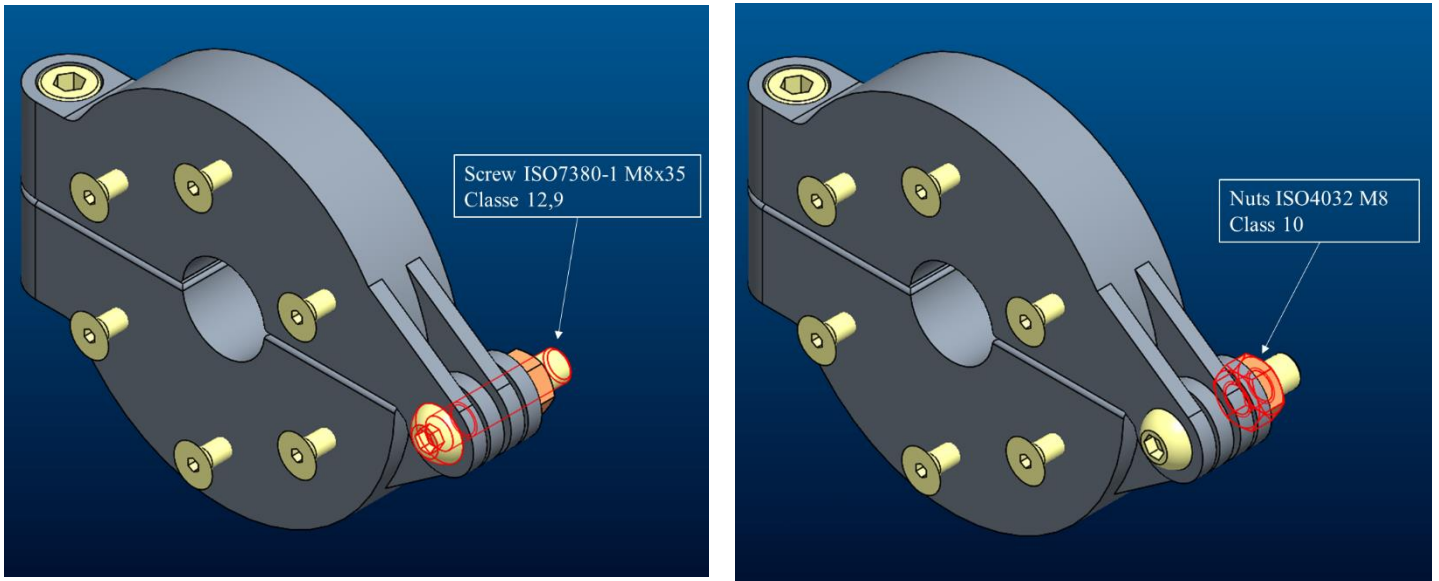

Figure 99 Adapter Fixture Screw and Nut

Motor Support Screws and Nuts

Screws ISO7380-1 M8x25
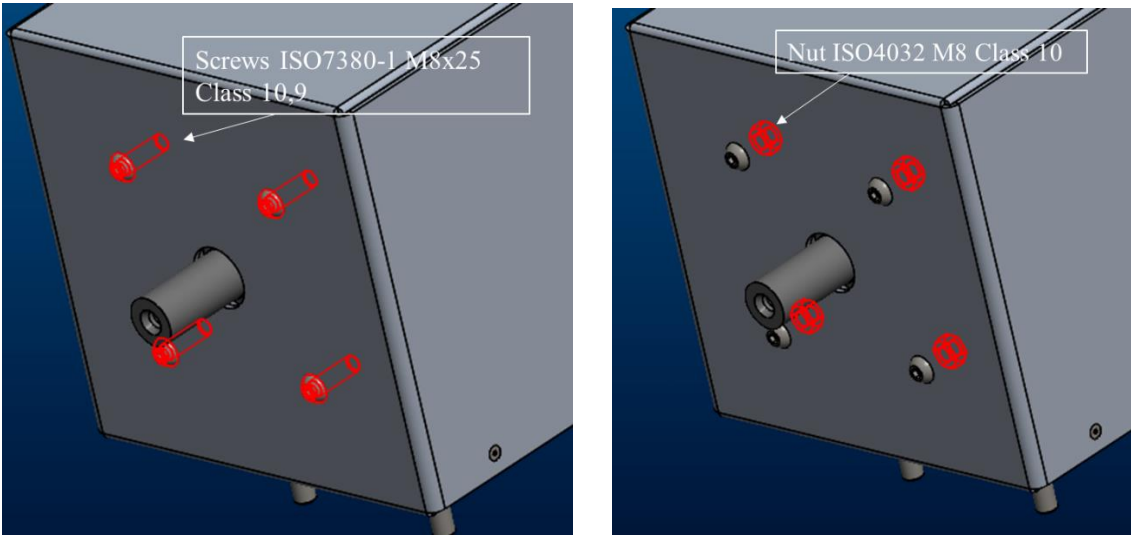Class 10,9

Nut ISO4032 M8 Class 10

Figure 100 Motor Support Screws and Nuts

5.7 FEM Analysis

Once the material (Aluminum EW-573 2011 T8) was declared into the ANSYS's engineer dataset, the geometry was imported into the "Design Modeler" module and simplified in order to obtain a greater result when meshing the component.

In the ANSYS's Mechanical Module the component was partitioned and mesh aiming to obtain structured and refined mesh on the critical points and a coarse mesh on the other points decreasing the computational cost of the analysis.
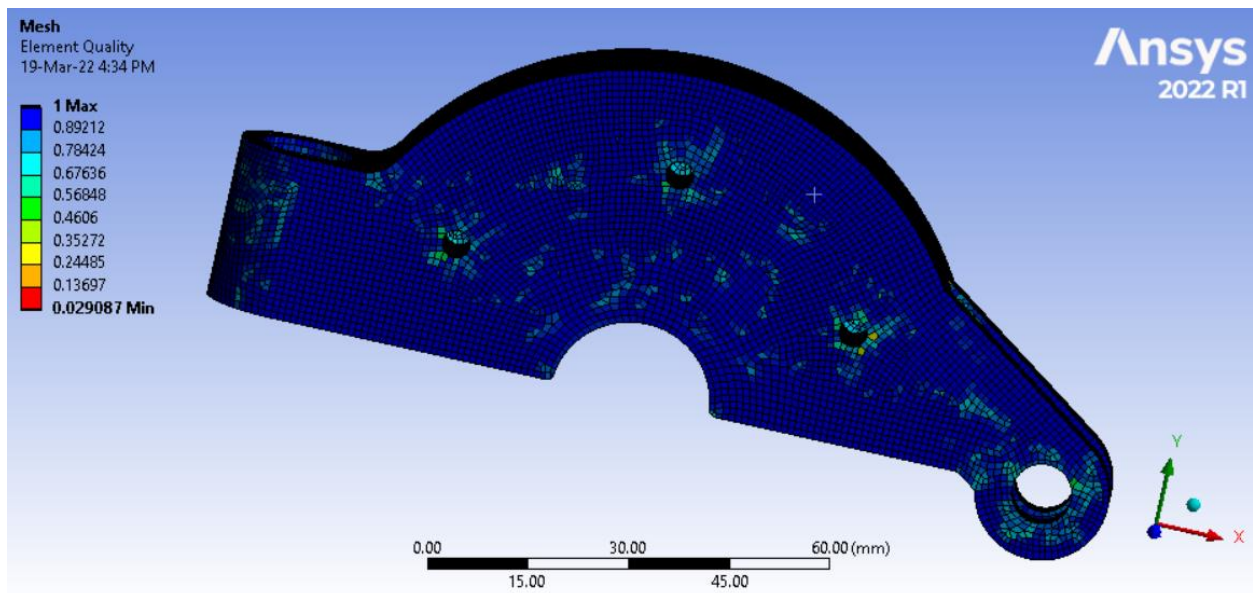

Figure 101 Element Quality

On the three central holes are applied the forces due to the steering torque, while on the lateral ones the load is due to screws used to clamp the adapter to the motor shaft. In addition, the contact surface between the adapter and motor shaft central is bounded through cylindrical support (no displacement in radial-axial and no rotations) and a bearing load is applied.
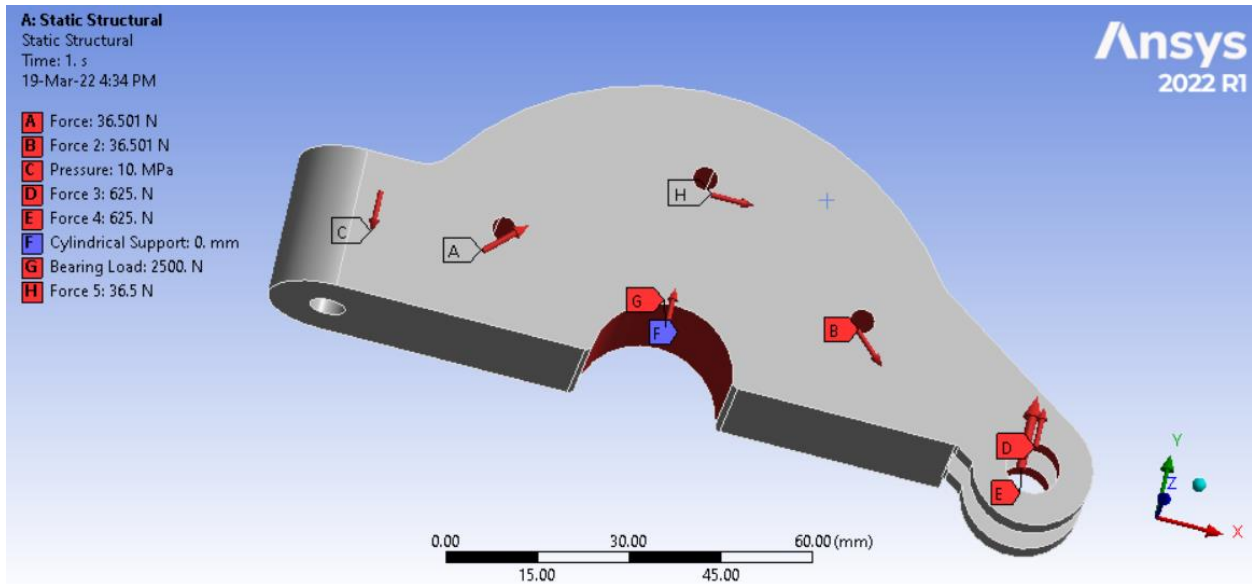
Figure 102 Forces and Boundaries

The Von-mises' equivalent stress analysis results show us that the biggest stress value is located on the inner diameter of the contact surface, and it is equal to 125.48 MPa, providing a safe factor equal to Sf= 2.51.
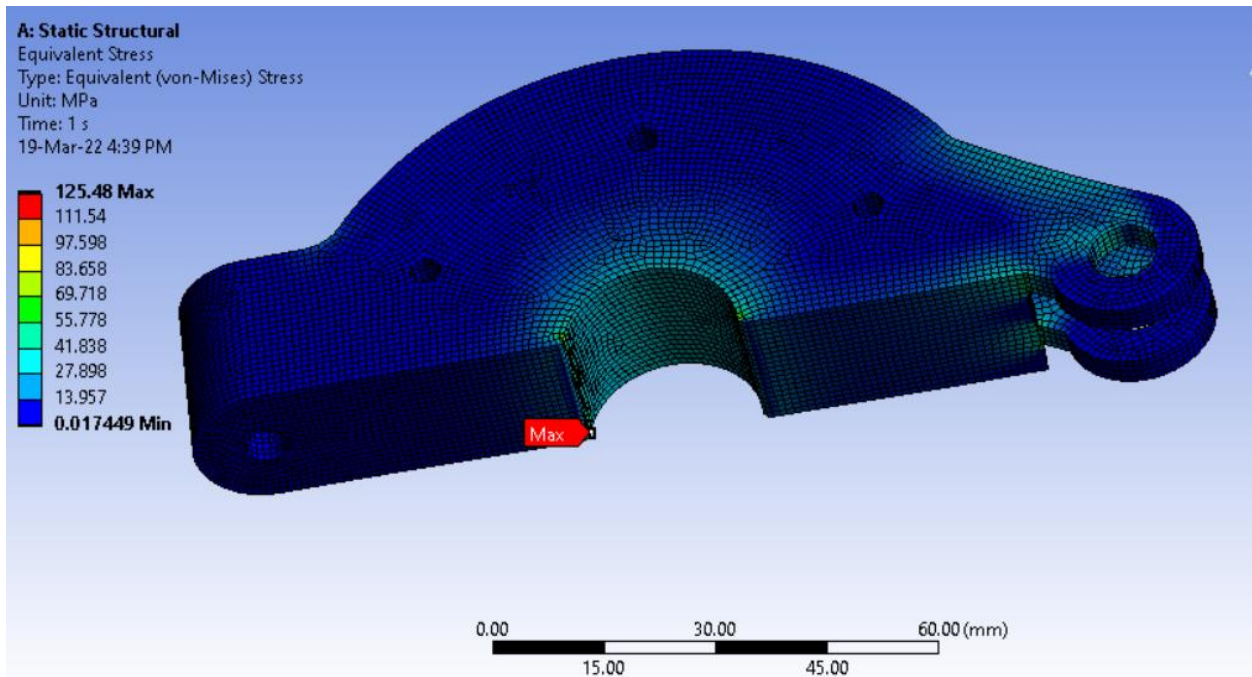

Figure 103 Von Mises' Equivalent Stress

Now look at the total deformation solution, we can observe the maximum deformation ii less than 0.1 mm and is located on the right end. Since there is a backslash equal to 1mm between screw external diameter and bore internal diameter, the deformation isn't a problem.
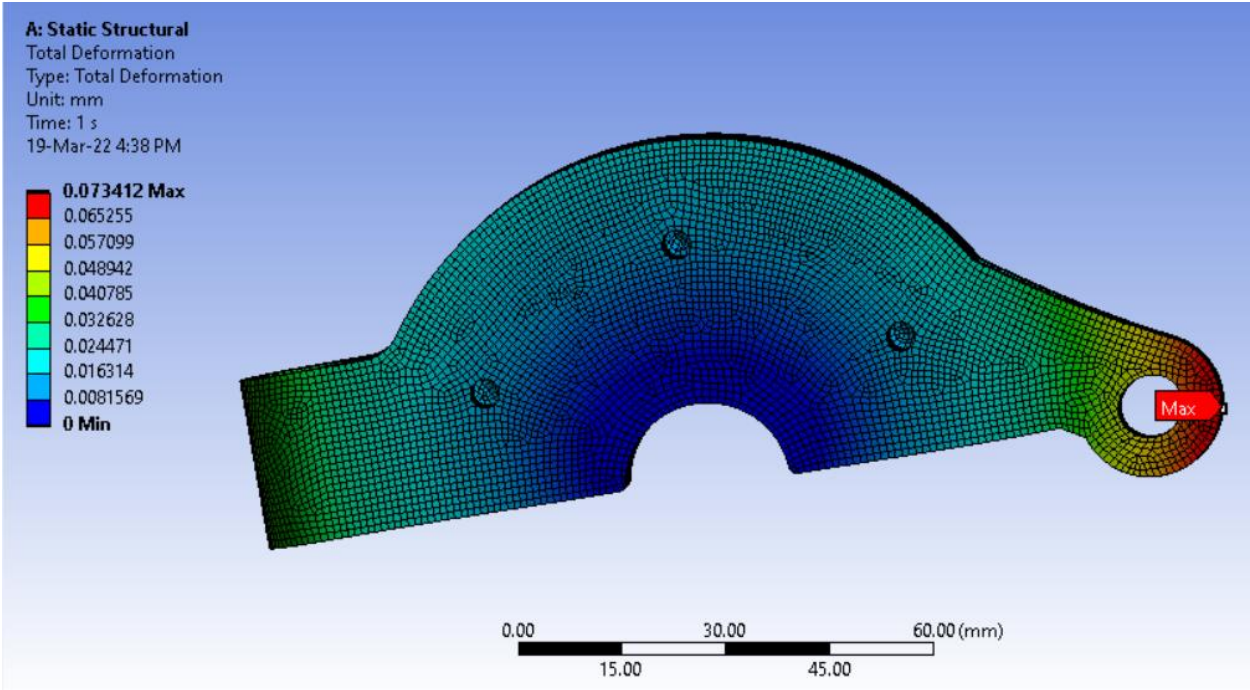

Figure 104 Total Deformation

5.8 Final Design

At the end of the analysis an adapter design, dynamically and statically verified was reached.

It is a clamping element with an embedded flange which is the interface for the handwheel to mount the wheel on the adapter and consequently to the motor shaft.

The final result is shown below:

Figure 105 Adapter Final Design
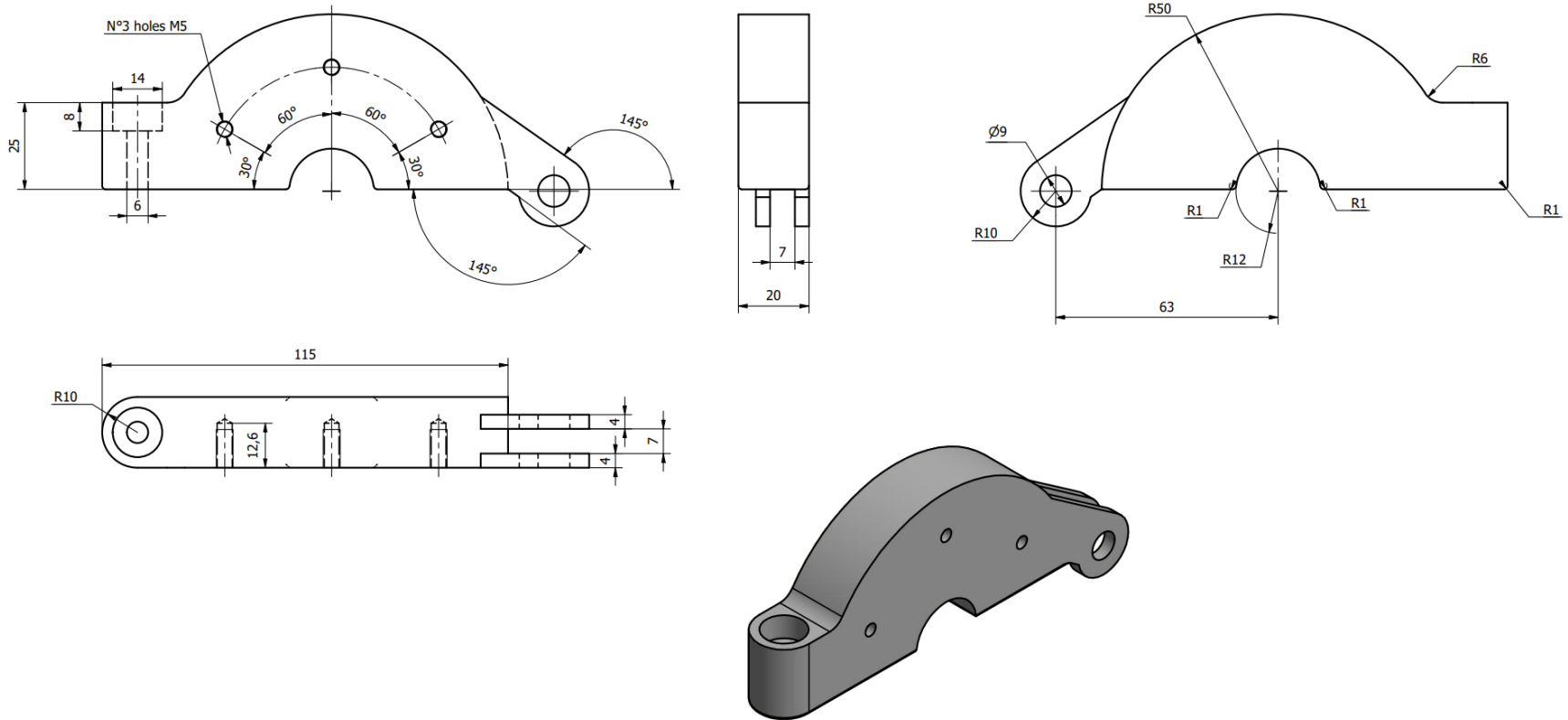
5.9 Drawings

Figure 106 Adapter drawing upper side

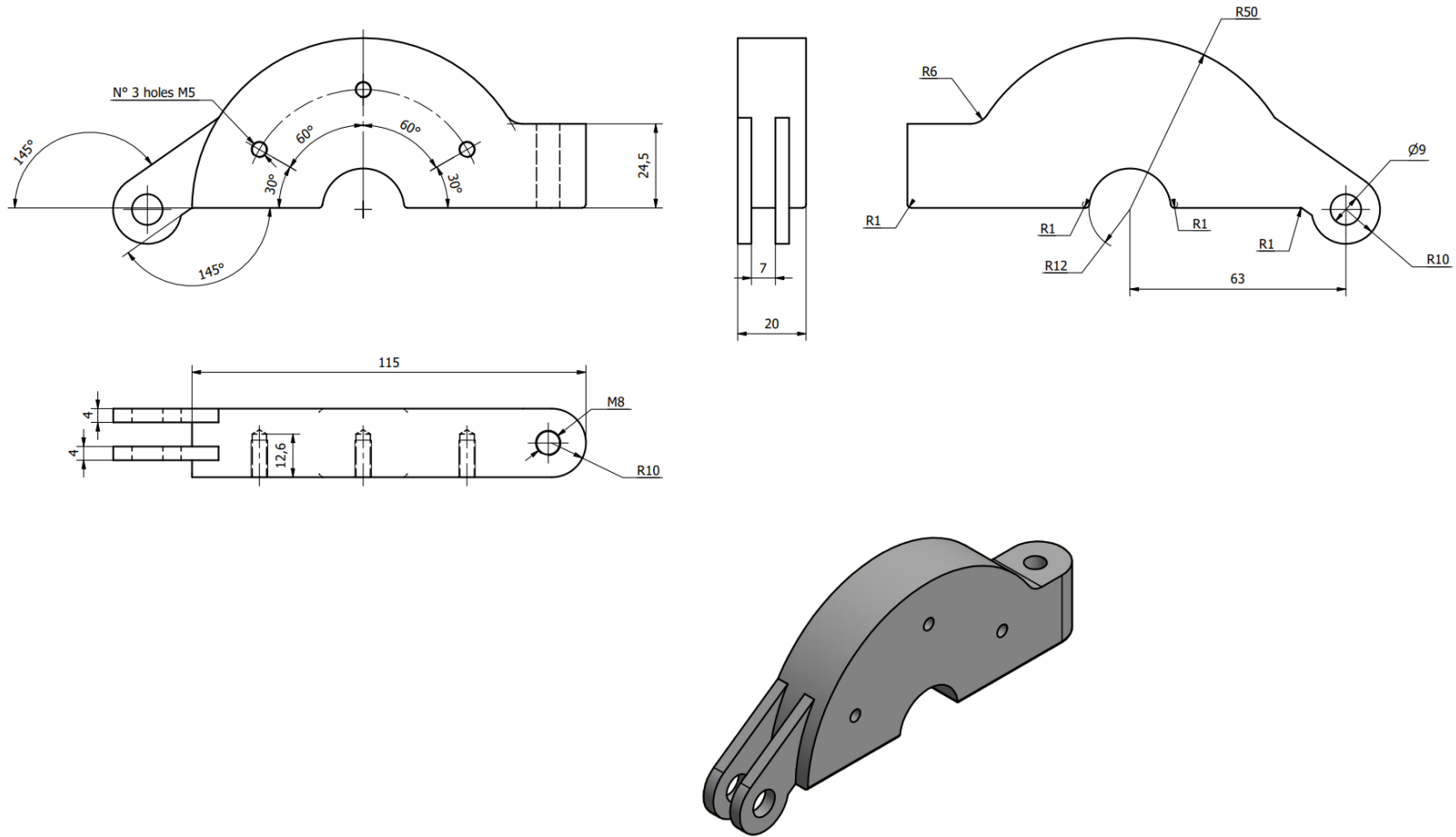Material: Aluminum EN 573-AW AlCu6BiPb (or 2011, UNI 9002/5), physical state T8

Figure 107 Adapter drawing downside

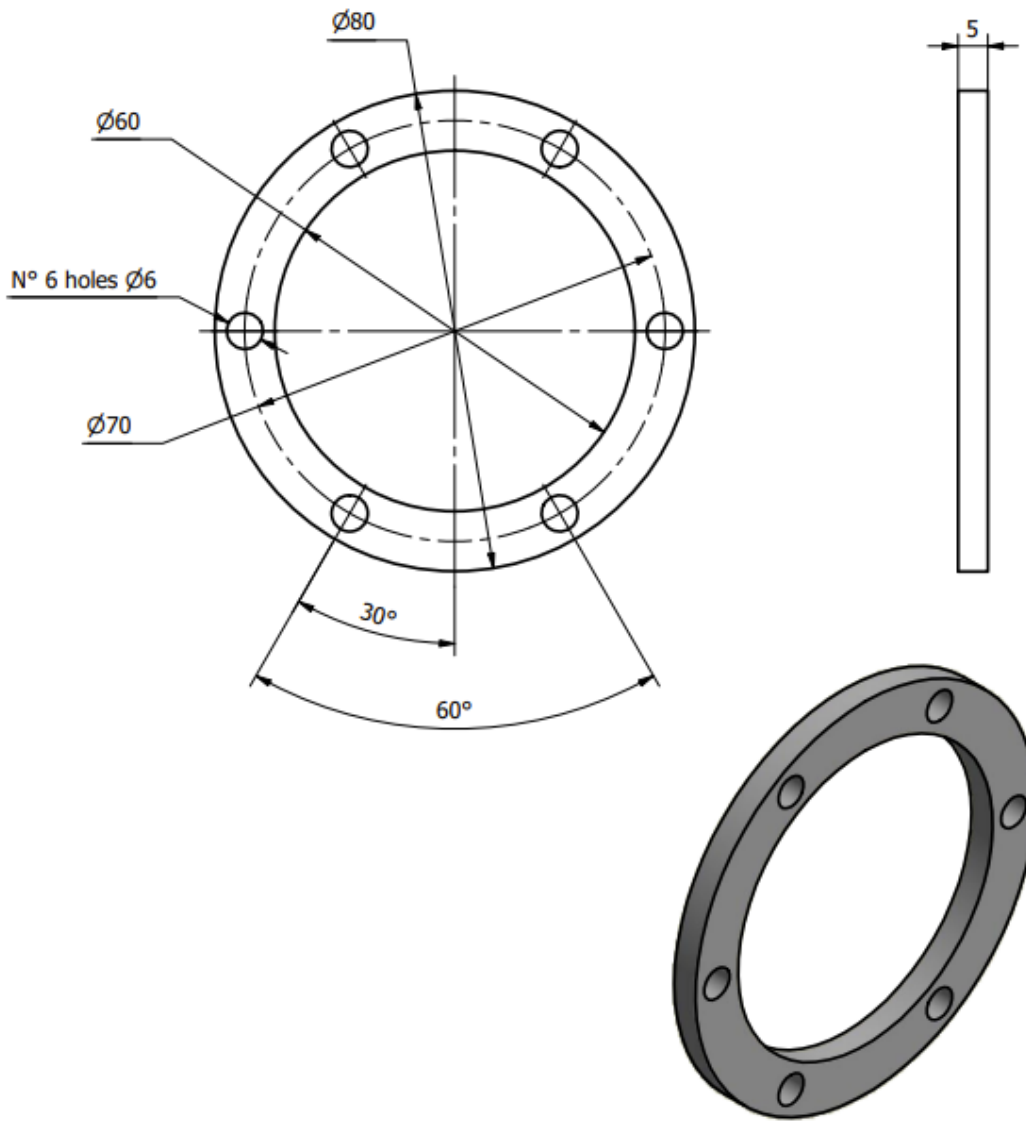Material: Aluminum EN 573-AW AlCu6BiPb (or 2011, UNI 9002/5), physical state T8

Figure 108 Spacer Drawing

Material: Aluminum EN 573-AW AlCu6BiPb (or 2011, UNI 9002/5), physical state T8

5.10 Commercial Coupling Solution

The cleanest way to fix the handwheel to a motor shaft is by using a clamping element.

Keeping in mind, the maximum transmitted torque is $T_{x_{max}} = 46\ Nm$, and the inner diameter of the handwheel interface is 55 mm, the chosen clamping element should have the external diameter smaller than 55mm and transmissible torque greater than 46Nm.

Given the requirements the chosen locking assembly was a Chiaravalli's self-centring RCK 61 with the following features:
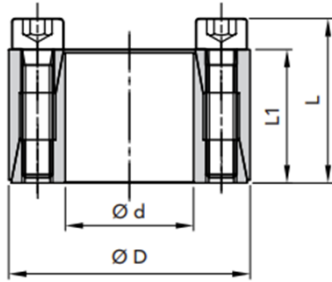
RCK 61 TYPE CLAMPING ELEMENTS
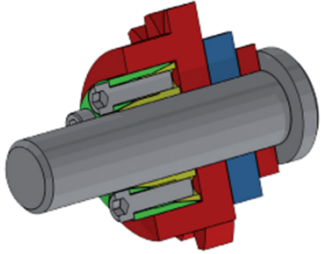
SELF CENTRING

THE RECOMMENDED MACHINING TOLERANCES FOR THE PRESSURE SURFACES ARE AS FOLLOWS:

Ø h 8 FOR SHAFT
Ø H 8 FOR HUB

PART NUMBER	DIMENSIONS				maximum torque Mt Nm	CLAMPING PRESSURE		CLAMPING SCREWS DIN 912 MAT. 12.9			EXTRACTION THREAD		WEIGHT Kg
	Ød	ØD	L1	L		Shaft N/mm²	Hub N/mm²	N.	Type	Torque Nm	Type	N.	
06610024	24	47	26	32	380	220	110	6	M6x25	16,2	M6	3	0,20

Figure 109 Clamping Elements

A flange is mounted on the clamping element to allow the handwheel to be coupled to the clamping element and consequently to the motor shaft.
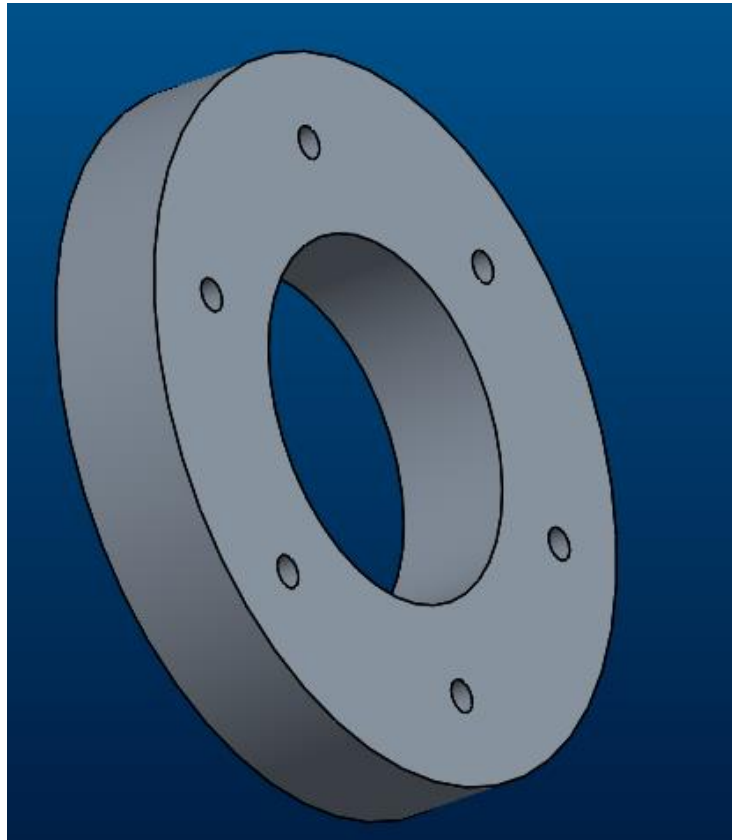
Figure 110 Flange

Material: Aluminum EN 573-AW AlCu6BiPb (or 2011, UNI 9002/5), physical state T8
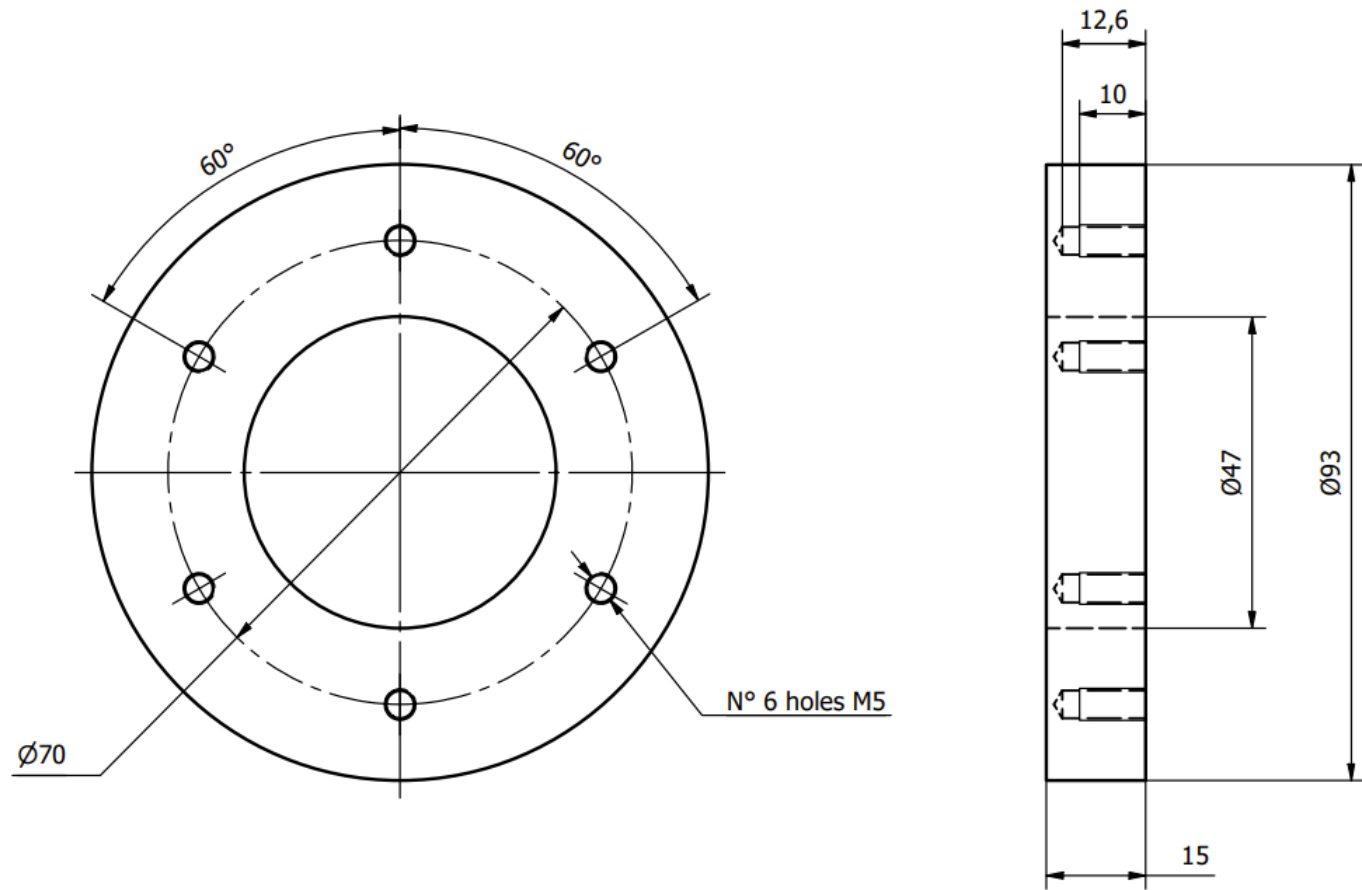
Figure 111 Flange Drawing

5.11 Motor Selection

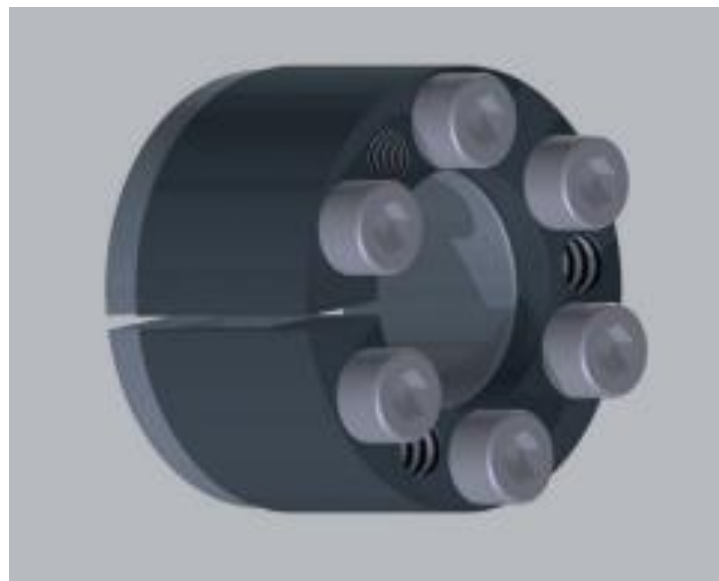The chosen motor must meet static, dynamic and performance requirements based on the application. Unlike common applications, the dynamic behaviour of the load is unknown, so this dissertation will consider only statical requirements, leaving the dynamic verification for future studies.

- Maximum radial force on the shaft at a distance d=26 mm from the mounting flange:

$$F_{radial,max} = \sqrt{F_{y,max}^2 + (F_{z,max} - m_{hub}g)^2} = 183N$$

- Maximum axial force on the shaft at a distance d=32 mm from the mounting flange:

$$F_{x,max} = 100N$$

- Peak Torque:

$$T_{peak} \geq 46Nm$$

The only dynamic verification that will be done is the motor bearing duration.

The motor that meets these requirements is the AKM2G-54 manufactured by KollMorgan, having the following features:

	Parameters	Tol	Symbol	Units	AKM2G-54 L	M	N
	Max Rated Equivalent Line Voltage	Max	Vbus	Vac	480	480	400
	Max Continuous Torque for ΔT winding = 100°C ①②③⑤	Nom	T_{cs}	Nm	20.1	20.0	20.0
				lb-in	178	177	177
	Continuous Current for ΔT winding = 100°C ①②③	Nom	I_{cs}	Arms	10.6	14.5	16.3
	Max Continuous Torque for ΔT winding = 60°C ②③⑤	Nom	T_{cs}	Nm	15.9	15.9	15.9
				lb-in	141	141	141
	Max Mechanical Speed ④	Nom	N_{max}	rpm	6000	6000	6000
	Peak Torque ①②③	Nom	T_p	Nm	54.8	54.7	54.7
				lb-in	485	484	484
	Peak Current	Nom	I_p	Arms	31.7	43.9	48.8
120 Vac	Rated Torque (speed) ①②③		T_{rtd}	Nm	-	19.3	19.1
				lb-in	-	171	169
	Rated Speed		N_{rtd}	rpm	-	1100	1200
	Rated Power (speed) ①②③		P_{rtd}	kW	-	2.22	2.40
				Hp	-	2.98	3.22
240 Vac	Rated Torque (speed) ①②③		T_{rtd}	Nm	18.4	17.2	16.5
				lb-in	163	152	146
	Rated Speed		N_{rtd}	rpm	1600	2300	2600
	Rated Power (speed) ①②③		P_{rtd}	kW	3.09	4.13	4.49
				Hp	4.14	5.54	6.02
400 Vac	Rated Torque (speed) ①②③		T_{rtd}	Nm	15.9	12.9	11.0
				lb-in	141	114	97.6
	Rated Speed		N_{rtd}	rpm	2800	3900	4500
	Rated Power (speed) ①②③		P_{rtd}	kW	4.66	5.28	5.20
				Hp	6.25	7.08	6.97
480 Vac	Rated Torque (speed) ①②③		T_{rtd}	Nm	14.3	9.80	-
				lb-in	126	86.7	-
	Rated Speed		N_{rtd}	rpm	3400	4800	-
	Rated Power (speed) ①②③		P_{rtd}	kW	5.08	4.92	-
				Hp	6.81	6.60	-

Where we can see that the Peak Torque is greater than what is needed.

5.11.1 Maximum Forces Verification

Shaft Loading

Motor	Max. Radial Force (N)	Max. Axial Force (N)
AKM2G-2	195	600
AKM2G-3	340	600
AKM2G-4	560	1400
AKM2G-5	890	1740
AKM2G-6	2000	2200
AKM2G-7	2670	3000

The maximum radial load ratings reflect the following assumptions:

1. Motors are operated with peak torque of the longest member of the frame size.

2. Fully reversed load applied to the end of the smallest diameter standard mounting shaft extension.

3. Infinite life with 99% reliability.
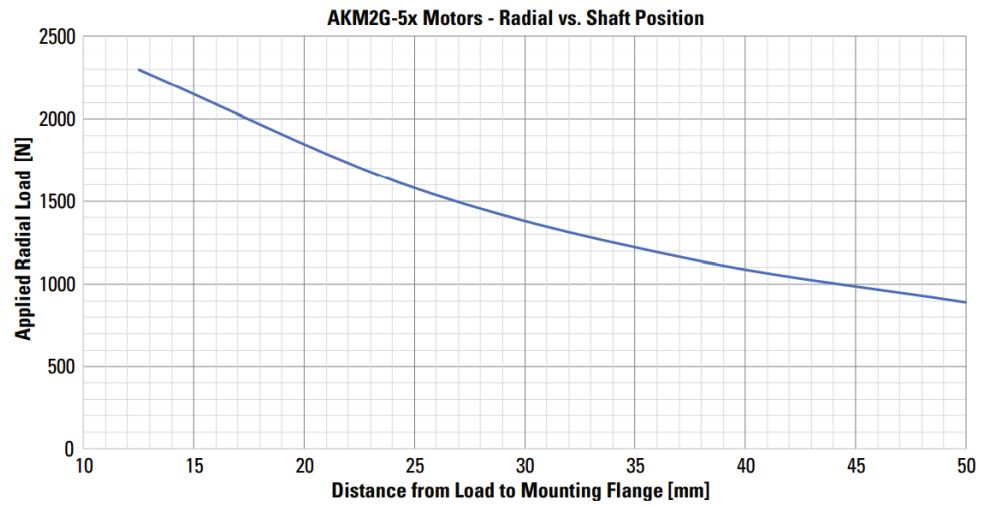
4. Safety factor = 2.

Figure 80 AKM2G-5X Motors Radial Load- Distance from mounting flange graph

At a distance of 32mm the allowed maximum radial force is around 1200N, which is much greater than the actual radial load of 183N, as well as the allowed maximum axial (1740N) load and the actual maximum axial load (100N) [44]

5.11.2 L10 Bearing Fatigue Verification

L10 is a parameter that measures (in cycles or hours) how long a bearing last given a load condition.

Below is shown the manufacturer's graph for L10= 20 000 h parametrized on rotational velocity :
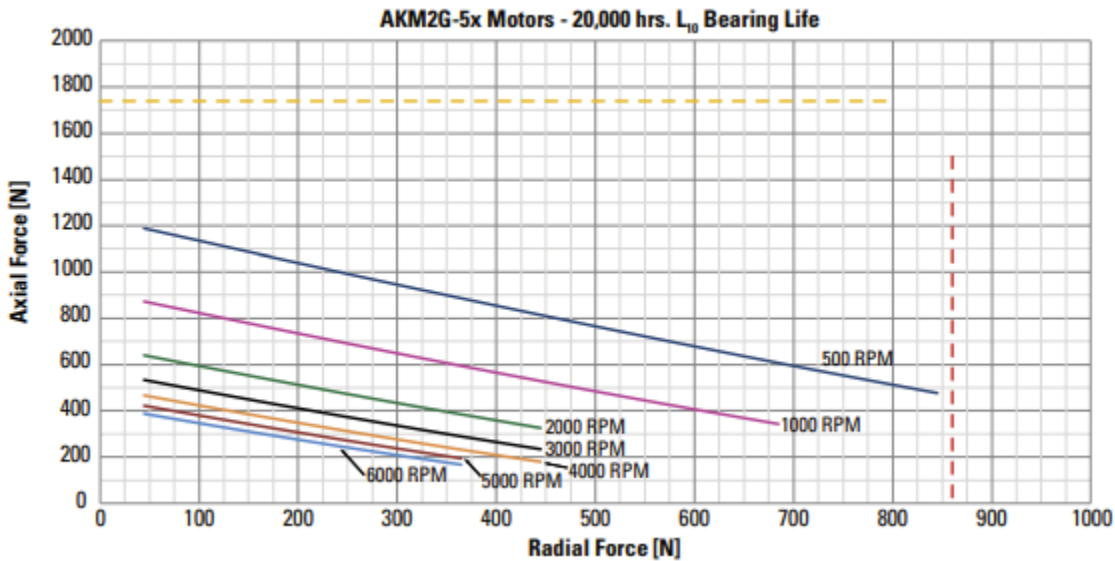

Figure 81 AKM2G-5X Motors L10 Bearing Life

The driving tests illustrated in the previous "Tests" Section lead us to consider the applied load on the steering wheel as a load condition with very low frequency. Indeed, the input load applied to the steering wheel had a frequency equal to 0.025Hz during the Passive Steering test and 0.25Hz during the Active Steering Test.

In order to identify the limit value for the axial and radial load from the L10 Bearing Fatigue Verification, the 500-rpm line is considered.

So reminding the load condition is:

$$F_{radial,max} = 183N \text{ and } F_{x,max} = 100N$$

The load is far below the limits.[44]

5.11.3 Finer Selection based on Load Dynamics

Aim a future study below will follow an explanation for the motor-transmission unit based on the alpha/beta method once the load dynamic characteristics are accurately defined.

The choice of the electric motor required to handle a dynamic load is closely related to the choice of transmission. This operation is bound by the limitations imposed by the motor's working range and is subjected to several constraints that depend indirectly on the motor (through its inertia J_m) and the reducer (through its transmission ratio τ).

A methodology for choosing the gear motor in order to ensure maximum acceleration of the system and reduce execution time for a particular law of motion is presented in Pasch and Seering (1984).

A simple but general model of a servo system can be characterized by three key elements: servo-motor, transmission, and load (Fig. 1). The load characteristics usually are completely known as they depend on the task, while the motor and the transmission are unknown until they are selected.
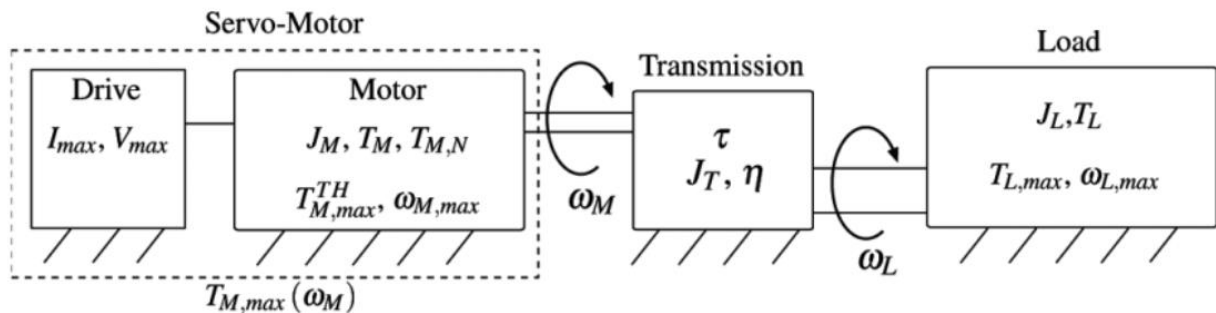

Figure 112 MTU model

Figure 1- Model of a generic machine

The power supplied by the motor depends on the external load applied (T_L) and on the inertia torque acting on the system ($T_L \dot{\omega}_L$). Since different patterns of speed (ω_L) and acceleration ($\dot{\omega}_L$) generate different loads, the choice of a proper law of motion is the first project parameter that should be taken into account when sizing the motor-reducer unit.

Frequently, in industrial applications, the machine's task is cyclical with a period ta which is normally much smaller than the motor thermal time constant:

in this case the motor, because of its capacity and thermal resistance, is unable to follow the fast heat oscillations of the power dissipated, which are then filtered: the temperature of the motor evolves as if it were subject to constant dissipated power, equal to the mean power dissipated in the cycle. Assuming that the heat dissipation is due to the Joule effect and the torque is proportional to the current, the motor behaviour can be analyzed through the root mean square (RMS) value of T_M defined as

$$T_{M,rms} = \sqrt{\frac{1}{t_a} \int_0^{t_a} T_M^2 \, dt},$$

(1)

namely the torque, acting steadily over the cycle, is attributable to the total energy dissipation that occurred in the cycle.

The selection of the actuator means checking the following conditions:

• rated motor torque:

$T_{M,rms} \leq T_{M,nom}$ (2)

• maximum motor speed:

$\omega_M \leq \omega_{M,max}$ (3)

• maximum servo-motor torque:

$T_m(\omega_m) \leq T_{M,max}(\omega_M)$ (4)

The terms on the right side of inequalities (2), (3), (4) are characteristic of each motor. On the other hand, the quantities $T_{M,rms}$, ω_M and T_M depend on the load and, therefore, on the reducer transmission ratio τ. The gear ratio adapts the torque and speed values required by the load to that available from the motor. Because of the mutual dependence between the motor and the transmission the selection of the two components should be performed in parallel. Moreover, the choice of transmission also depends on other factors, such as the torque applied on the transmission shaft, the maximum achievable speed, potential clearances, and the system's mechanical efficiency η. The transmission is approximated to a system with no moment of inertia and no loss of power (η= 1).

Since each motor has a maximum achievable speed ($\omega_{M,max}$), we have:

$\omega_{L,max} \leq \tau\omega_{M,max}$ (5)

where $\omega_{L,max}$ is the maximum speed achieved by the load. Considering a specific motor, the condition on the maximum achievable speed (3) can be written in terms of τ:

$$\tau \geq \tau_{M,lim} = \frac{\omega_{L,max}}{\omega_{M,max}} \qquad (6)$$

where $\tau_{M,lim}$ is defined, for each motor, as the ratio between the maximum speed achieved by the load and the one achievable by the motor. For a specific motor, $\tau_{M,lim}$ is the minimum transmission ratio value that can be employed to drive the given load.107

The motor torque T_M can be written as:

$$T_M = \tau T_L^* + J_M \dot{\omega}_M = \tau T_L^* + J_M \frac{\dot{\omega}_L}{\tau}, \qquad (7)$$

Where

$$T_L^* = T_L + J_L \dot{\omega}_L \qquad (8)$$

is the generalized resistant torque at the load shaft. Equation (7) highlights the dependence of the applied torque on the gear ratio and the inertia of the motor, while from (8) we can see that all the terms related to the load are known.

The root means square torque is obtained from (1):

$$T_{M,rms}^2 = \int_0^{t_a} \frac{T_M^2}{t_a} dt = \int_0^{t_a} \frac{1}{t_a} \left(\tau T_L^* + J_M \frac{\dot{\omega}_L}{\tau} \right)^2 dt. \qquad (9)$$

and then

$$T_{M,rms}^2 = \tau^2 T_{L,rms}^{*2} + J_M^2 \frac{\dot{\omega}_{L,rms}^2}{\tau^2} + 2 J_M (T_L^* \dot{\omega}_L)_{mean}. \qquad (10)$$

Inequality (2) can be written as

$$\frac{T_{M,N}^2}{J_M} \geq \tau^2 \frac{T_{L,rms}^{*2}}{J_M} + J_M \frac{\dot{\omega}_{L,rms}^2}{\tau^2} + 2 (T_L^* \dot{\omega}_L)_{mean}. \qquad (11)$$

Let's introduce two parameters, the accelerating factor of the motor:

$$\alpha = \frac{T^2_{M,N}}{J_M},$$

(12)

which describes the performances of each motor, and the load factor:

$$\beta = 2\left[\dot{\omega}_{L,rms}T^*_{L,rms} + (\dot{\omega}_L T^*_L)_{mean}\right],$$

(13)

That defines the performance required by the task.

Using α and β, Eq. (11) becomes

$$\alpha \geq \beta + \left[T^*_{L,rms}\left(\frac{\tau}{\sqrt{J_M}}\right) - \dot{\omega}_{L,rms}\left(\frac{\sqrt{J_M}}{\tau}\right)\right]^2.$$

(14)

Since the term in brackets is always positive, or null, the load factor β represents the minimum value of the right-hand side of Eq. (14). This means that the motor accelerating factor α must be sufficiently greater than the load factor β, for the inequality (11) to be verified. The preliminary choice of motor is made by comparing only the values α and β; these values are easily calculated if we know the mechanical properties of the motor and the load features. A motor must be rejected if α<β, while if α≥β the motor can have enough rated torque if τ is chosen properly.[45]

5.12 Carter Design

The motor carter is an aluminium metal sheet bent in a proper to provide mechanical support to the motor and enclose every electronic equipment. The carter was designed to provide the framework for the installation of a cooling system for keeping low the temperature of the electronic components.
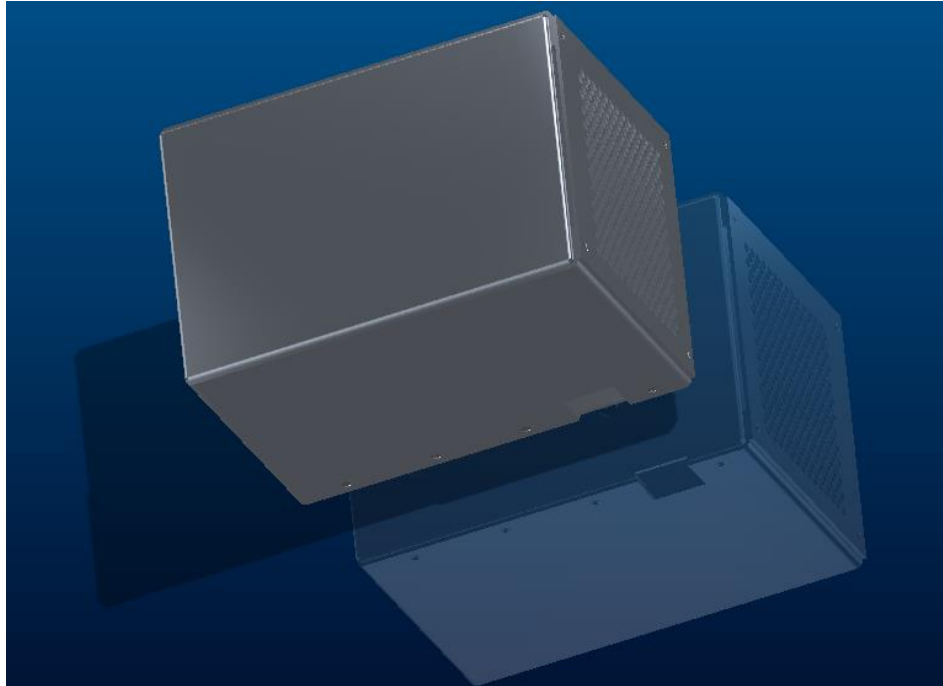
Figure 113 Carter Front

Figure 114 Carter Rear

5.12.1 Material

The component will be considered made of Aluminum EN 573-AW Al-Cu4MgSi (or 2017A, UNI 9002/2), physical state T451.

Process Characteristics:

Anodizing   DISCREET

Machinability   GOOD

Corrosion resistance   DISCREET

Mechanical Characteristics:

$R_s = 285\ MPa = \text{Yield Strength}$

$R_m = 430 MPa = Ultimate\ Tensile\ Strength$

Physic Characteristics:

$E = Young's\ Modulus = 72\ 000\ MPa$
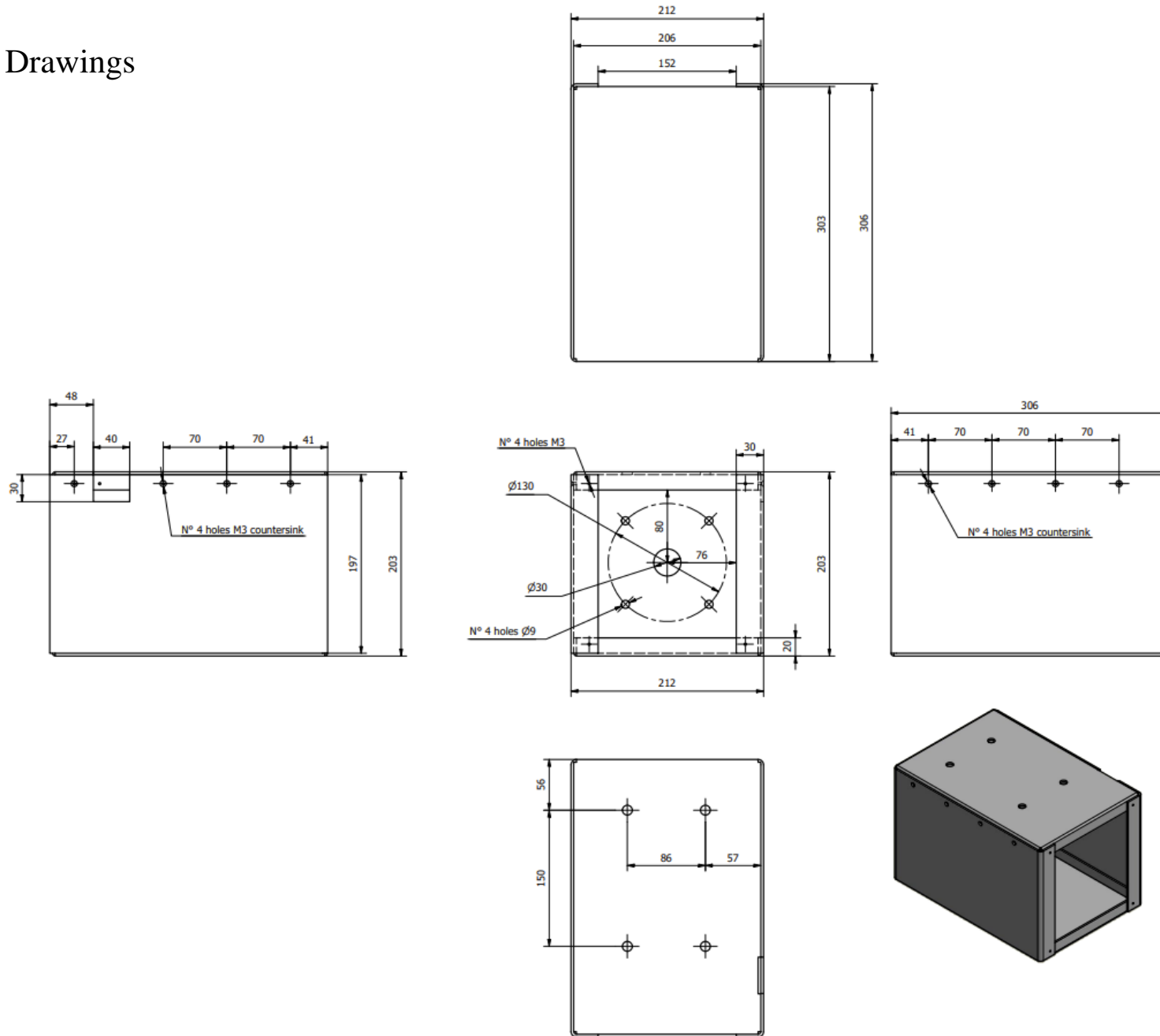
$Poisson's\ Coefficient = 0.33$

Density = 2.78 g/cm^3

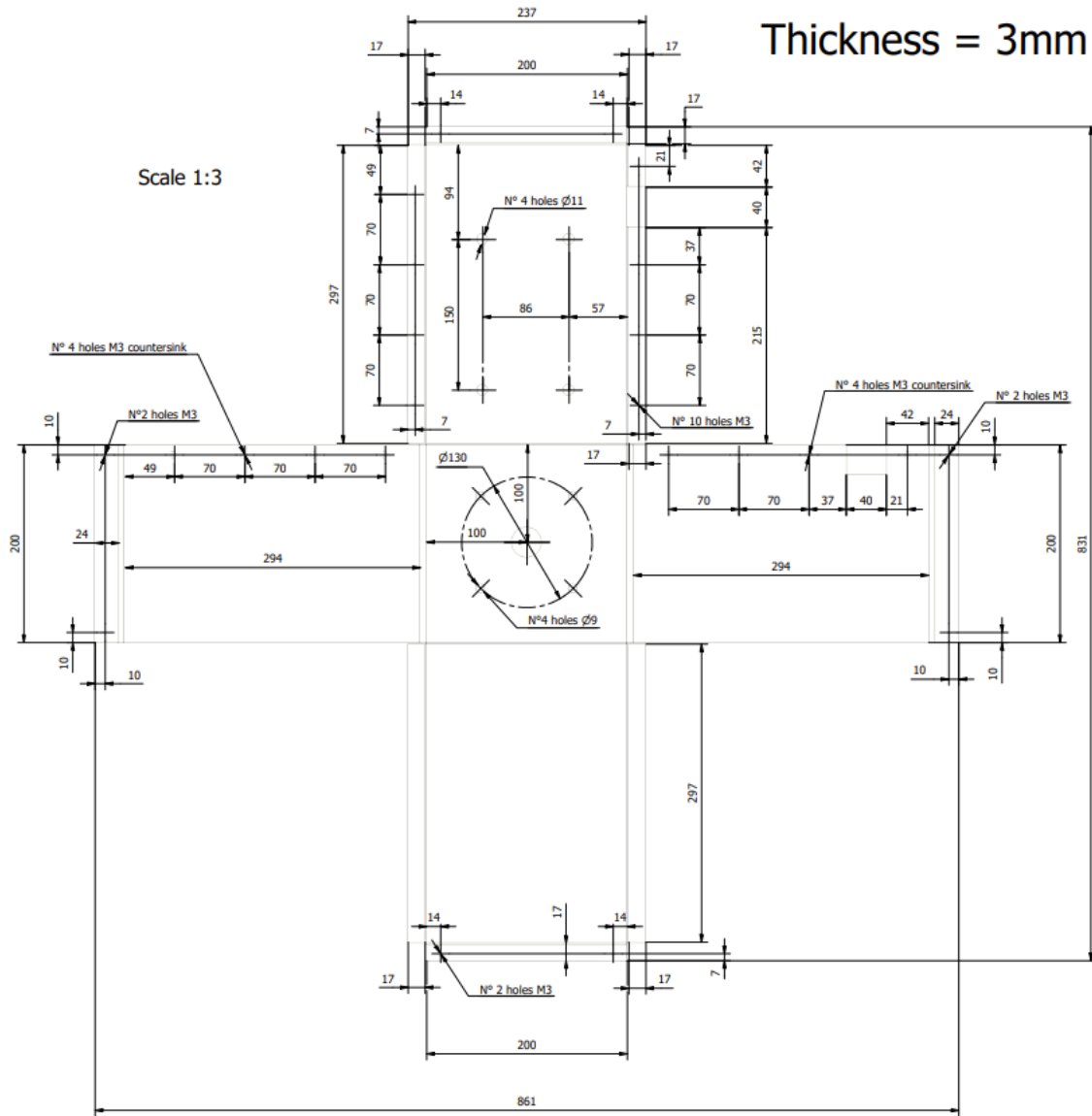## 5.12.2 Drawings

Figure 115 Carter
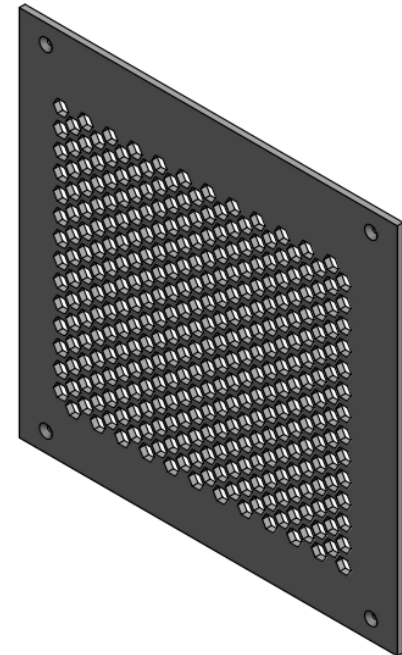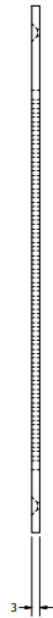
Figure 116 Carter Unbend

Figure 117 Carter Back Cover
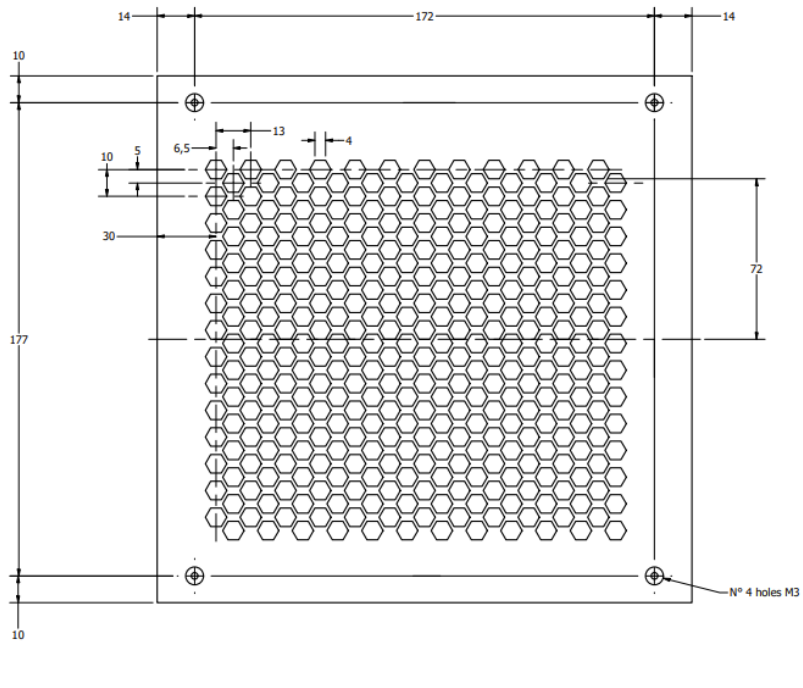
5.13 Final Assemblies

In this capture, the two final assemblies were shown. For the first assembly isometric, lateral, back and front views will be reported, while the second assembly only isometric and lateral as the other view is like the first assembly.

5.13.1 Adapter Assembly

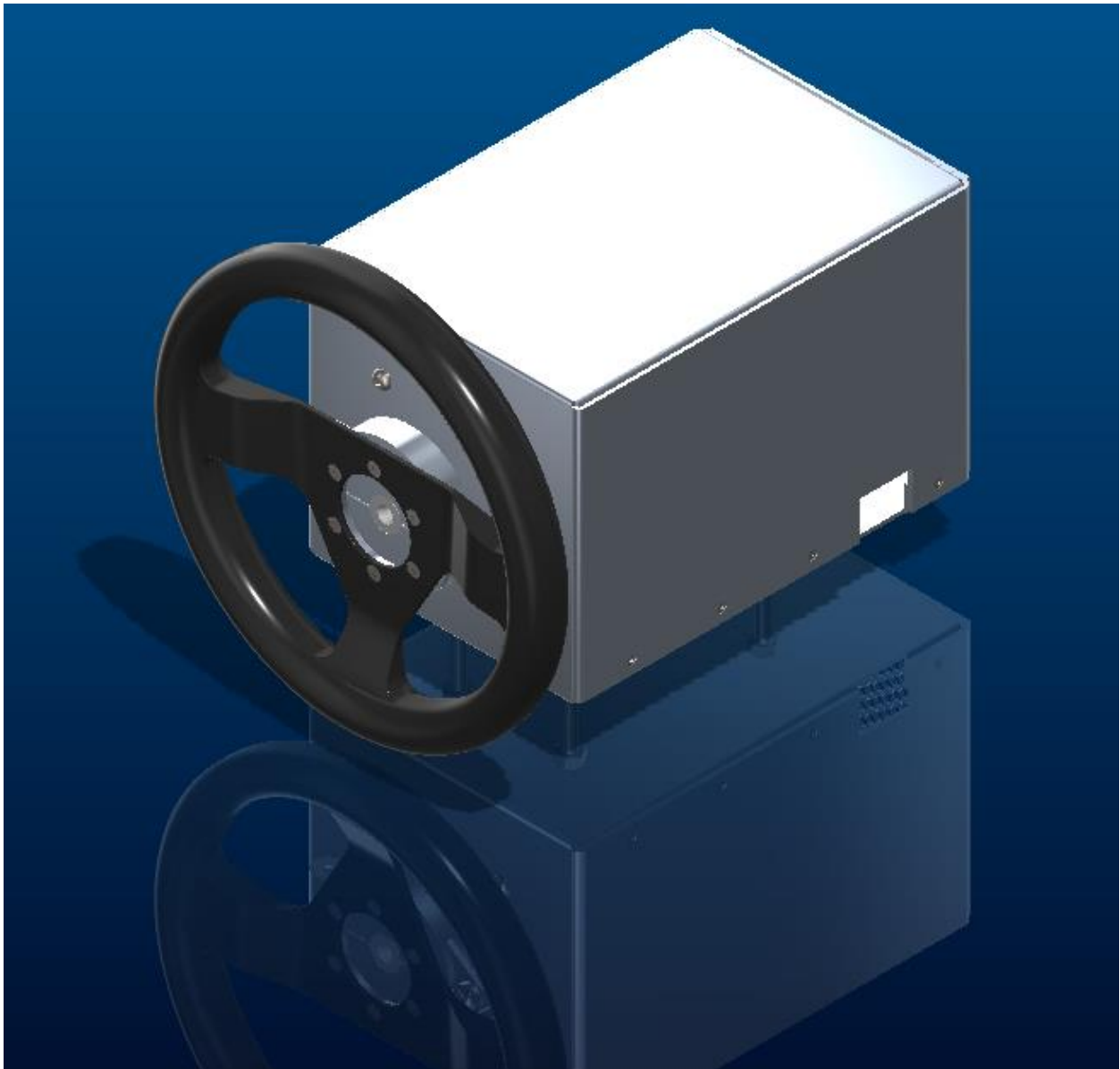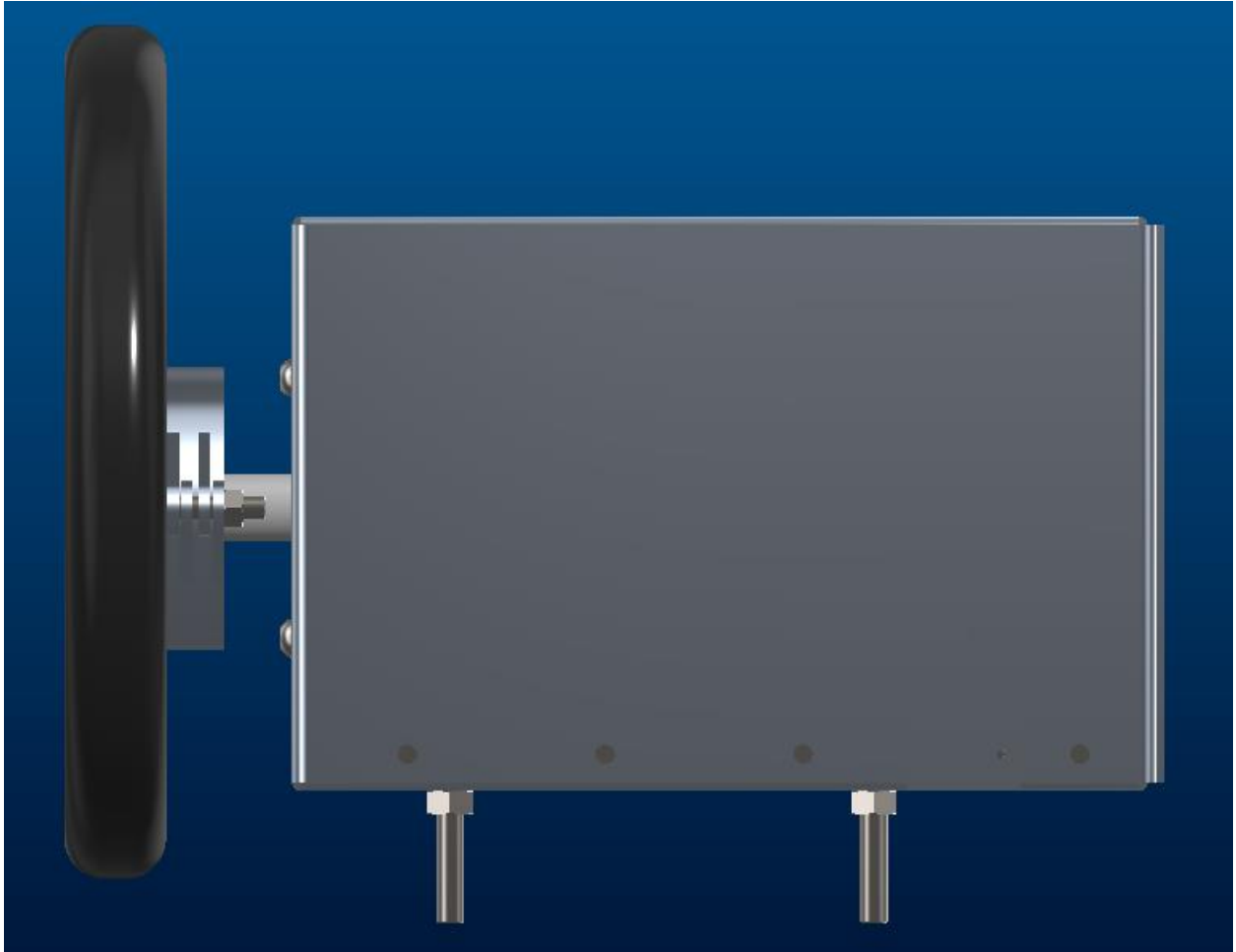**Figure 118 Adapter Assembly**

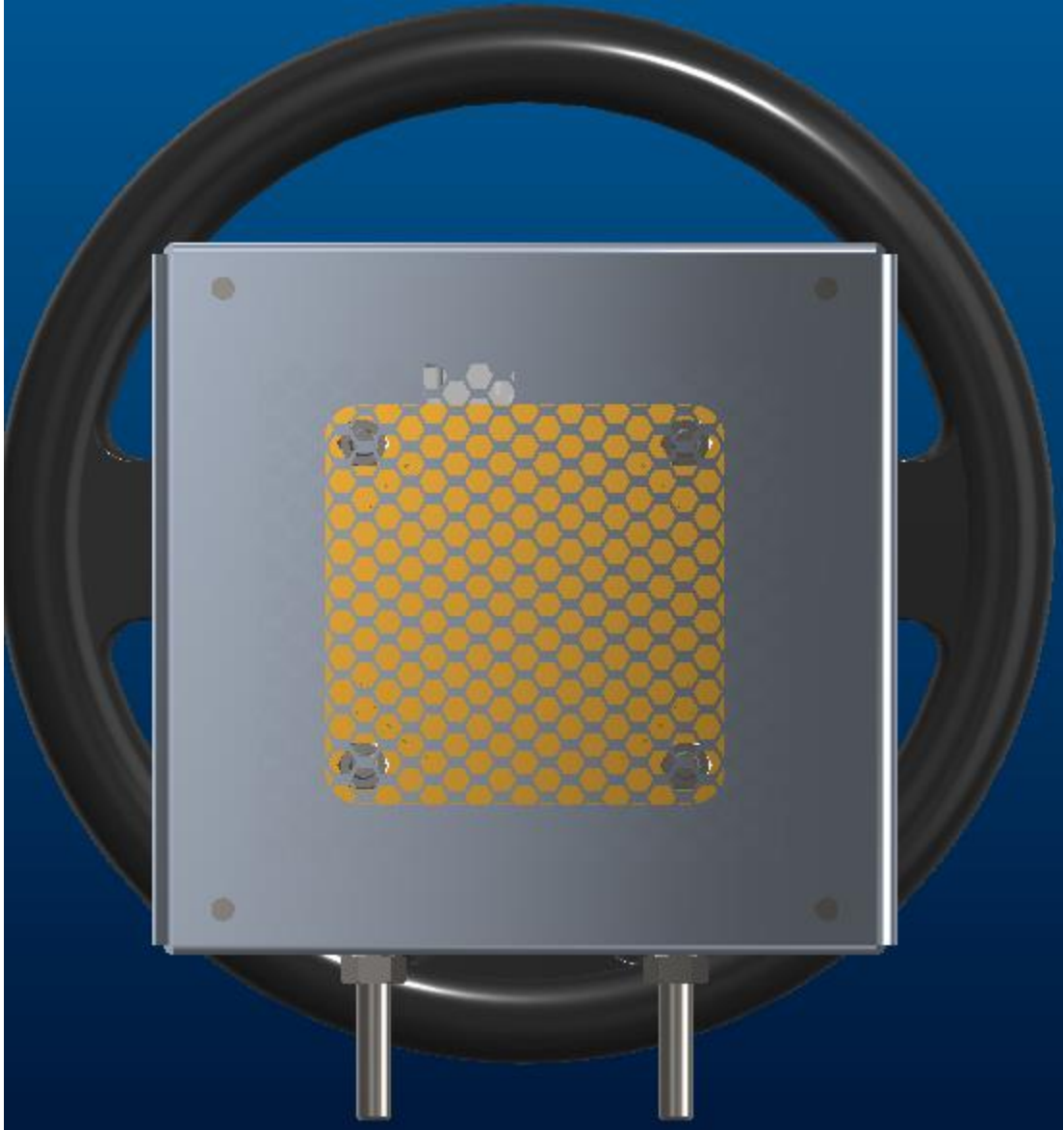**Figure 119 Adapter Assembly**

Figure 120 Adapter Assembly

Figure 121 Adapter Assembly

5.13.2 Clamping Element Assembly

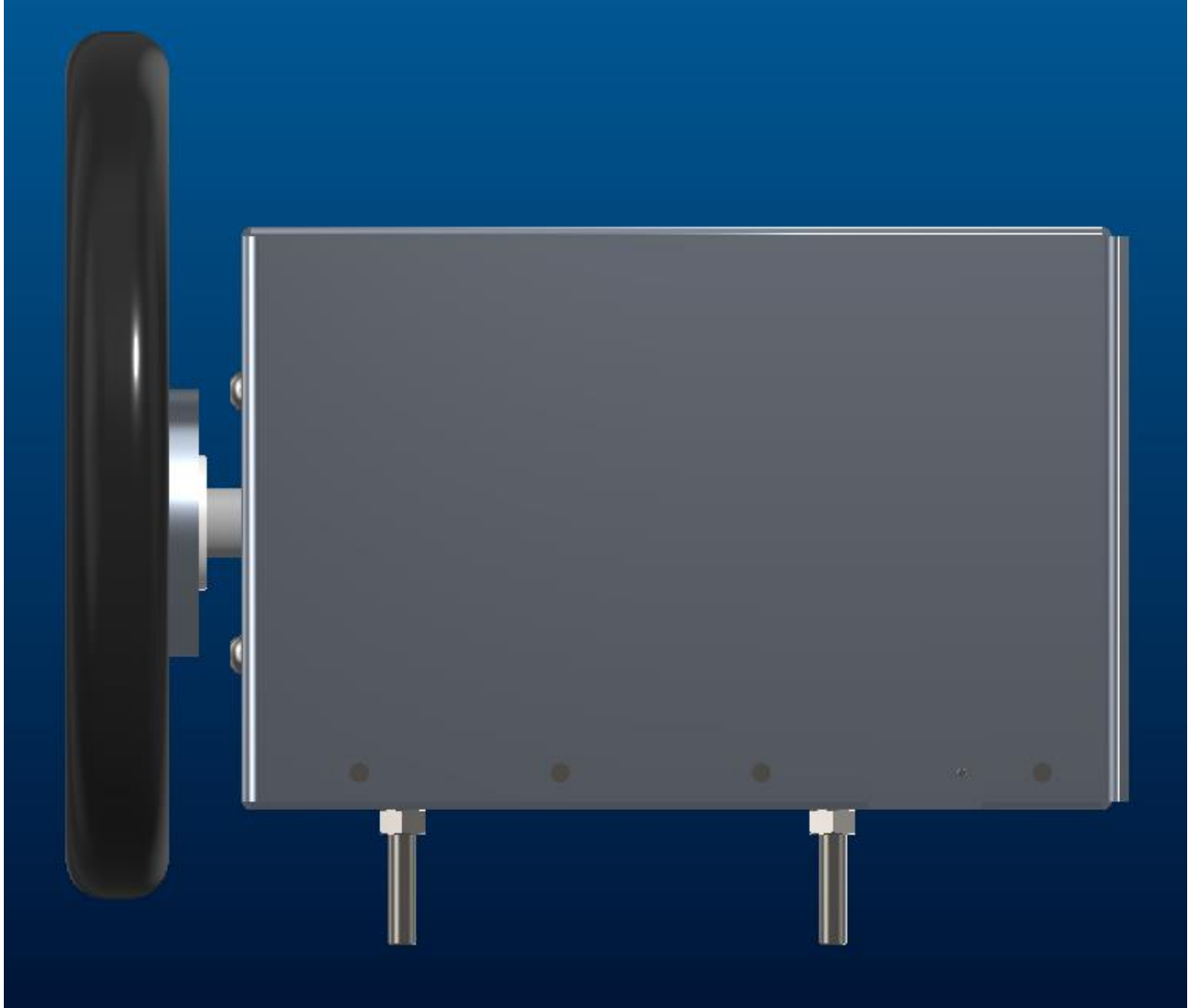**Figure 122 Clamping Element Assembly**

Figure 123 Clamping Element Assembly

6 Conclusion, Recommendation and Future Work

The main conclusions obtained in this master thesis were a benchmark identification through an analysis of current commercial and literal solutions, the outline of a new specification for creating an improved force-feedback steering wheel system, a suitable motor selection and the proposition of some mechanical design alternatives.

The benchmark performances compared to the driving tests results (which report critical driving situations) exposed the weak points of the currently available solutions. Given the necessary improvements, the project specifications were outlined.

Based on the new requirements and using an appropriate method, a suitable motor was chosen.

Then some mechanical design alternatives of a coupling system for fixing the handwheel to the motor shaft were proposed and verified theoretically and by FEM, besides the motor carter design.

Some recommendations for future work and further development, to obtain a completely functioning improved force-feedback steering wheel:

- Force-Feedback Steering Wheel Electric and Electronic Design, starting from the market and literature study realized for the identification of the benchmark, consequently, the specification for an improved electric and electronic design.

- Development and application of Control Algorithm

- Tests and Validation

References

[1] OC Racing – Youtube – What is Force Feedback – Available from: https://www.youtube.com/watch?v=1ri_OXzT9Mg [Accessed on 28th March 2022]

[2] ocsimracing.com – What is Force Feedback? – Available from: https://www.ocsimracing.com/general-ocsimracing/what-is-force-feedback [Accessed on 28th March 2022]

[3] Jesse Parker – ezsimracer.com - What is Force Feedback in Racing Wheels? Do you need it? – Available from: https://ezsimracer.com/force-feedback/ [Accessed on 28th March 2022]

[4] SimXperience – Direct Drive vs Belt Drive vs Gear Drive – Available from: https://www.simxperience.com/blog/simxperience-news-1/direct-drive-vs-belt-drive-vs-gear-drive-70 [Accessed on 28th March 2022]

[5] Amujo Olasoji – hotcars.com – Everything You Need To Know About The Direct Drive Wheel – Available from: https://www.hotcars.com/direct-drive-wheel-everything-need-know/ [Accessed on 28th March 2022]

[6] Gómez Fernández, J. (2012). A Vehicle Dynamic Model for Driving Simulators. Master's Thesis, Department of Applied Mechanics, Division of Vehicle Engineering and Autonomous Systems, Chalmers University of Technology, Göteborg, Sweden

[7] Obialero, E. (2013). A Refined Vehicle Dynamic Model for Driving Simulators. Master's Thesis, Department of Applied Mechanics, Division of Vehicle Engineering and Autonomous Systems, Chalmers University of Technology, Göteborg, Sweden.

[8] Suspension Designer – KPI Kingpin angle, scrub radius & wheel centre offset – Available from: https://www.suspensiondesigner.com/kpi-kingpin-angle-scrub-radius-wheel-centre-offset/ [Accessed on 28th March 2022]

[9] Jonathan Vogel – Race Car Engineer (racecar-engineering.com) – Tech Explained: Steering Forces – Available from: https://www.racecar-engineering.com/tech-explained/tech-explained-steering-forces/ [Accessed on 28th March 2022]

[10] Olsson H., Åström K.J., Canudas de Wit C., Gäfvert M., Lischinsky P. (1997): Friction Models and Friction Compensation.

[11] Adams F.J., (1981): Proceedings of the Institution of Mechanical Engineers, Automotive Power Steering "Feel". SAGE

[12] Honeycutt C., Sushko J. (2011): Haptic Feedback Steering Wheel, Department of Mechanical Engineering, University of South Florida, Tampa, FL, 33620, U.S.A.

[13] Mohellebi H., Kheddar A., Member, IEEE, and Espié S. (2009): Adaptive Haptic Feedback Steering Wheel for Driving Simulators, IEEE TRANSACTIONS ON VEHICULAR TECHNOLOGY, VOL. 58, NO. 4

[14] Hengdrive BLDC Motor-B4260M Datasheet – Available from: http://www.klsele.com/admin/product_upload/20150324094550KLS23-B4260M.pdf [Accessed on 28th March 2022]

[15] Reddit Forum – T300 / TX motor upgrade success – Available from: https://www.reddit.com/r/simracing/comments/ln2a87/t300_tx_motor_upgrade_success/ [Accessed on 28th March 2022]

[16] AliExpress – PowerGrip® GT3 324 3MGT 9 Datasheet – Available from: https://it.aliexpress.com/item/32670202229.html?spm=a2g0s.9042311.0.0.27424c4d32RUT0 [Accessed on 28th March 2022]

[17] Gamma di cinghie PowerGrip® GT3 – Available from: https://ww2.gates.com/Italy/brochure.cfm?brochure=10045&location_id=14620 [Accessed on 28th March 2022]

[18] Project cars game Forum – I think my T300 has died, Page 7 – Available from: https://forum.projectcarsgame.com/showthread.php?34895-I-think-my-T300-has-died/page7 [Accessed on 28th March 2022]

[19] Reddit Forum – Thrustmaster TX/T300 tune-up and replacement parts – Available from: https://www.reddit.com/r/simracing/comments/97pl86/thrustmaster_txt300_tune_up_and_replacement_parts/ [Accessed on 28th March 2022]

[20] THRUSTMASTER T300 RS Power Supply – Available from THRUSTMASTER T300 RS Alimentatore EUR 60,05 - PicClick IT [Accessed on 28th March 2022]

[21] city-driving.co.uk – T300 fan replacement – Available from: https://forum.city-driving.co.uk/showthread.php?tid=26208 [Accessed on 28th March 2022]

[22] chiefly-choice.com – DC BRUSHLESS FAN Datasheet – Available from: http://www.chiefly-choice.com/fans/uploads/122939245975j0n.pdf [Accessed on 28th March 2022]

[23] Reddit Forum - Logitech G920 Wheel falling out of calibration / becoming off-centre during gameplay – Available from:

https://www.reddit.com/r/simracing/comments/79e7zw/just_for_reference_logitech_g920_wheel_falling/ [Accessed on 28th March 2022]

[24] YouTube – G27 Racing Wheel: Tear Down and Inspection – Available from: https://www.youtube.com/watch?v=aepgg1Fecww&t=859s [Accessed on 28th March 2022]

[25] YouTube – Logitech g27 rattle/chatter fix – https://www.youtube.com/watch?v=SeOQfNlwGmM&t=202s [Accessed on 28th March 2022]

[26] Leilei Motors – rs555sh-15260 datasheet – Available from: https://www.leili-motor.net/uploads/RS-555SH.jpg) [Accessed on 28th March 2022]

[27] Gt Planet Forum – Increasing power to the Logitech G920 – Available from: https://www.gtplanet.net/forum/threads/increasing-power-to-the-logitech-g920.392673/ [Accessed on 28th March 2022]

[28] Tonyk182 – Il Logitech G27 smantellato nelle sue componenti – Available from: https://www.tonyk182.com/2016/02/05/il-logitech-g27-smantellato-nelle-sue-componenti/ [Accessed on 28th March 2022]

[29] Inside Sim Racing (isrtv.com) – Logitech G29 steering wheel review – Available from: https://www.isrtv.com/logitech-g29-review/#:~:text=They%20offer%20the%20same%20256,resolution%20that%20the%20G27%20offers. [Accessed on 28th March 2022]

[30] YouTube – FANATEC DD1/DD2 TEARDOWN, How a Fanatec Direct Drive Wheel Base Works – Available from: https://www.youtube.com/watch?v=MDiQ9zmqOss [Accessed on 28th March 2022]

[31] YouTube – Fanatec Podium DD1 Review – Available from: https://www.youtube.com/watch?v=2oKccb4-y4o [Accessed on 28th March 2022]

[32] Fanatec – Podium Wheel Base DD1 Available from: https://fanatec.com/eu-en/racing-wheels-wheel-bases/wheel-bases/podium-wheel-base-dd1 [Accessed on 28th March 2022]

[33] Simucube 2 Pro | Direct Drive Force Feedback wheelbase – Available from: https://simucube.com/simucube-2-pro/ [Accessed on 28th March 2022]

[34] YouTube – Simucube 2 Pro R2, Recensione vs Fanatec Podium – Available from: https://www.youtube.com/watch?v=AqCGvFM4ktg [Accessed on 28th March 2022]

[35] Wikipedia – Comparison of direct-drive sim racing wheels – Available from:

https://en.wikipedia.org/wiki/Comparison_of_direct-drive_sim_racing_wheels [Accessed on 28th March 2022]

[36] EdRacing.com – Steering Wheel Torque – Available from:
http://www.edracing.com/edr/Wheel-Torque.php [Accessed on 28th March 2022]

[37] An Assessment of Human Driver Steering Capability, National Highway Traffic Safety Administration of US Department of Transportation

[38] Docket Number NHTSA-2004-19951-2, January 6, 2005.

[39] Massimiliano Gobbi, Francesco Comolli, Masatoshi Hada, Gianpiero Mastinu, An instrumented steering wheel for driver model development.

[40] Toyota – Available from: https://www.toyota.com/ [Accessed on 28th March 2022]

[41] Kvaser – Available from: https://www.kvaser.com/ [Accessed on 28th March 2022]

[42] OxTS – Available from: http://www.oxts.com/ [Accessed on 28th March 2022]

[43] ACI-SARA LAINATE – Available from: http://www.vallelunga.it/it/aci-sara-lainate/ [Accessed on 28th March 2022]

[44] AKM2G Servo Motor Selection Guide – Available from:
https://www.kollmorgen.com/sites/default/files/AKM2G-KM_SG_000315_RevC_EN-mobile_ed.pdf [Accessed on 28th March 2022]

[45] Giberti H., Cinquemani S., Legnani G. (2011) – A PRACTICAL APPROACH TO THE SELECTION OF THE MOTOR-REDUCER UNIT IN ELECTRIC DRIVE SYSTEMS – Dipartimento di Meccanica, Politecnico di Milano, Milano, Italy, Università degli Studi di Brescia, Brescia, Italy

[46] Alubremen Srl – Barre 2011 T3/T6/T8 – Available from:
https://www.alubremen.com/it/prodotto/barre/2011-t3t6t8/ [Accessed on 28th March 2022]

[47] Alubremen Srl – Laminati 2017 T451 – Available from:
https://www.alubremen.com/it/prodotto/laminati/2017a-t451/ [Accessed on 28th March 2022]

[48] Rockwell, T.H. (1972) Skills, Judgment and Information Acquisition in Driving, In Human Factors in Hinhwav Traffic Safety Research, (T. W. Forbes, Editor), John Wiley & Sons, 133-164.

[49] Gordon, D. A. (1966) Experimental Isolation of Drivers' Visual Input. Public Roads, 33, 53-68.

[50] Ronald R. Mourant and Praveen Sadhu (2002), Evaluation of Force Feedback Steering in a Fixed Based Driving Simulator, Virtual Environments Laboratory 334 Snell Engineering Center Northeastem University Boston, MA 02115